

Search for Nuclear Magnetic Resonance Evidence of Spin Accumulation

THÈSE N° 4434 (2009)

PRÉSENTÉE LE 26 JUIN 2009

À LA FACULTÉ SCIENCES DE BASE

LABORATOIRE DE PHYSIQUE DES MATÉRIAUX NANOSTRUCTURÉS

PROGRAMME DOCTORAL EN PHYSIQUE

ÉCOLE POLYTECHNIQUE FÉDÉRALE DE LAUSANNE

POUR L'OBTENTION DU GRADE DE DOCTEUR ÈS SCIENCES

PAR

Aurore RUDOLF

acceptée sur proposition du jury:

Prof. G. Meylan, président du jury

Prof. J.-Ph. Ansermet, directeur de thèse

Prof. A. Domingues dos Santos, rapporteur

Prof. C. Hébert, rapporteur

Dr M. W. Pieper, rapporteur



ÉCOLE POLYTECHNIQUE
FÉDÉRALE DE LAUSANNE

Suisse
2009

“Above all, don’t fear difficult moments. The best comes from them.”

Rita Levi Montalcini

Acknowledgments

This thesis was made possible because of all the people who supported and helped me in one way or another during these last four years, both in my professional and personal life.

I am grateful to my advisor, Prof. Jean-Philippe Ansermet, for the trust he has placed in me from the onset of this Doctoral work. As much as his contagious passion for Physics and Science in general, I appreciate his being available at all times, his enthusiasm and his kindness. His can-do attitude has been a challenging and motivating driving force. I would also like to thank him for giving me the opportunity and encouraging me to escape the everyday routine by carrying out experiments in different institutes at the EPFL as well as in Sweden, and for all the opportunities that he offered to me to travel around the world and to broaden my vision of science.

I thank Dr. Jacques van der Klink for his priceless help and support with the NMR hardware during this thesis work as well as for his availability. He was also ready to engage me in helpful discussions at any time with great patience and kindness. I would like to express my total gratitude to Dr. Mohamed Abid, who was here when I just started and continued to give me substantial and unwavering support all throughout this work. I have no words to express just how much I appreciate his hard work and incisive suggestions, his day-to-day presence, helping and providing answers to the most challenging scientific and experimental questions I have had. Thanks also for his friendship and I hope to have gained some of his impressive experimental skills. Thank you to Dr. Maria-Eleni Belesi for the amazing work and help she provided me with ever since she arrived. Her kindness has made these last nine months of my work so much brighter.

I am indebted to Prof. Antonio Domingues dos Santos for providing me with precious samples and for his involvement in my thesis jury. I would also like here to acknowledge all the other members of the jury, the president Prof. Georges Meylan, Prof. Cécile Hébert and Dr. Martin Wilhelm Pieper for accepting to read the following pages and for their precious suggestions regarding future work.

I am grateful to all the members of the technical staff, and especially Gilles Grandjean, José Grandjean, Michel Fazan, André Schläfli and Claude Amendola and to the secretaries of the institute for their efficiency and kindness, Florence Choulat, Monique Bettinger and especially Chantal Roulin for her friendship. Thanks

a lot to Nicolas Leiser for his precious help regarding the cleanroom.

For the fruitful collaborations, I thank here Prof. László Forró, Prof. Hubert Girault, Dr. Jean Gamby, Dr. Sima Valizadeh, Dr. Hanna Yousef and Dr. Ana Akrap for her trust and friendship.

I thank Dr. Simon Granville who generously gave his time and attention not only to proofread this manuscript but also to advise me on magnetic experiments. Thank you to Dr. Mirko Milas for his help, notably in Solid Works drawings in the first two years of this work. Thank you to Dr. Bálint Náfrádi for his help, for our precious discussions and for his friendship.

My gratitude extends to my colleagues, both past and present members of the group who became valuable friends, for the collegial atmosphere, their assistance and our memorable times in day-to-day work as much as outside the EPFL. In order of appearance, thank you Dr. Andrea Fabian Montabert, Dr. Christophe Terrier, Dr. Santiago Serrano-Guisan, (very near future Dr.) Sami Jannin, Dr. Arnaud Comment, Dr. Fiodar Kurdzesau, Elena Murè, Dr. Nicolas Bizière.

Thank you to Dr. Neven Barišić for his unconditional support before, during and certainly after the thesis. Thanks a lot to Dr. Titusz Fehér, for his friendship and his kind invitations and opportunities to travel to Budapest. A special thank you to Ana, Pablo, Camilo, Johanna, Vincent and Silvia. Thanks a lot to my badminton and running mates and friends, Ana, Pablo, Haiming, Johanna, John, Markus, Maria-Eleni who made Friday and Wednesday evenings so much fun. Thank you so much to all my friends who accompanied me all or partway along this path, Martial, Daniel, Jacqueline, Agi, Anna, Claudia, Anikó, Arnaud, Tamas, Csilla, Guido, Yanki, Ízaro, Joy, Katarzyna, David, Luka, Sherine, Gustav, Gøran.

Tous mes remerciements vont maintenant à mes amis en France, Bénédicte, Célia, Isabelle, David, Marion pour avoir su rester si proches de moi malgré la distance. Merci aux deux bouts de chou, Corentin et Marion, pour leur affection dont ils font preuve à chacun de mes retours en Alsace.

Le plus grand merci va à mes parents pour leur amour, leurs encouragements et leur soutien inconditionnels. Je suis reconnaissante à mon frère Alexandre, qui a toujours soutenu ma décision de passer quatre années à proximité des montagnes

suisses. Et enfin, merci à tous les membres de ma famille pour leur soutien.

Version abrégée

Les développements vers la compréhension des propriétés de transport à l'interface entre deux métaux différents - ferromagnétique et non magnétique - ainsi que la découverte de la magnétorésistance géante ont suscité un fort intérêt à la fois de la communauté scientifique mais aussi de l'industrie électronique avec la perspective d'utiliser le spin des électrons dans des systèmes électroniques rapides, à l'échelle nanométrique. La polarisation de spin obtenue en injectant un courant à travers une nanostructure magnétique est appelée "accumulation de spin". Au cours de ce travail de thèse, nous avons utilisé la résonance magnétique nucléaire (RMN) du ^{59}Co à champ nul sous courant afin de sonder cet effet. Aucune mesure locale de l'accumulation de spin n'a été rapportée à notre connaissance. La RMN était une technique de choix pour cette étude, étant donné qu'elle permet de sonder de manière locale la structure électronique et sa dynamique.

Dans la première partie de cette thèse, nous présentons les spécificités de la RMN dans les ferromagnétiques. Nous examinons également l'effet attendu sur le signal RMN du fait de l'accumulation de spin. Dans une deuxième partie, nous décrivons et caractérisons les différents échantillons que nous avons étudiés au cours de ce travail de thèse : des granulaires, des nanofils multicouches et des piliers de taille micrométrique. La troisième partie est consacrée à la description des spectres RMN du ^{59}Co obtenus pour divers échantillons. Nous avons également mesuré les temps de relaxation spin-spin et spin-réseau dans les échantillons granulaires de Co/Cu. Cette étude est cruciale dans le choix des meilleurs candidats pour les expériences de RMN sous courant. Enfin, nous avons utilisé une technique de résonance nucléaire ferromagnétique excitée et détectée électriquement, développée dans le cadre de cette thèse. Cette technique présente plusieurs avantages par rapport à la RMN classique : aucune bobine ni aucun circuit résonnant ne sont nécessaires et surtout, cette technique ouvre de nouvelles perspectives sur la possibilité d'étudier de plus petits échantillons, qui n'auraient pas pu l'être par des méthodes de RMN classique. Une nette amélioration en découle, car le courant nécessaire pour obtenir les densités de courant voulues sont de fait plus faibles, et ainsi, le champ créé par ce courant est

diminué. La résonance nucléaire ferromagnétique excitée et détectée électriquement a été utilisée pour les mesures sous courant. Les densités de courant injectées étaient suffisamment élevées dans les échantillons pour induire des effets mesurables sur les spectres obtenus, qui sont décrits et interprétés dans la partie finale de ce manuscrit.

Mots-clés: RMN à champ nul, nanostructures, échantillons magnétoresistifs, accumulation de spin, résonance nucléaire ferromagnétique excitée et détectée électriquement.

Abstract

Developments towards an understanding of the nature of conductance at the interface between two different metallic layers - ferromagnetic and non magnetic - as well as the discovery of giant magnetoresistance have stirred attention from both the scientific community as well as the electronics industry, with the prospect of using the spin of electrons in fast, nano-sized electronic devices. The spin polarization obtained by driving a current through a magnetic nanostructure is referred to as “spin accumulation”. In this thesis work, we use ^{59}Co zero-field nuclear magnetic resonance (NMR) under an additional current in order to probe spin accumulation. To the best of our knowledge, no local measurement of spin accumulation has yet been reported. NMR was chosen as the most appropriate technique for this study, as it is a local probe of the electronic structure and its dynamics.

In the first part of this thesis, we present the main characteristics of NMR in ferromagnets. We also discuss the effect expected in the NMR due to spin accumulation. In the second part, we describe and characterize the different samples that we investigated during this study: granular samples, multilayered nanowires and micro-pillars. The third part is devoted to the description of ^{59}Co NMR lineshapes obtained for different samples. In addition, we measured the spin-spin and spin-lattice relaxation times in the Co/Cu granular samples. This study is of tremendous importance to choosing the best candidate sample for NMR experiments under additional current. Finally, we used a method of electrically excited and electrically detected ferromagnetic nuclear resonance (EDFNR) developed during the course of this work. This technique presents several advantages over standard FNR: neither coil nor resonant circuit is needed and, overall, EDFNR opens the possibility of studying samples with much fewer nuclei than is achievable with standard nuclear resonance methods. This could provide an important development to decrease the current needed for the same current density in the samples, which is of great interest due to the smaller magnetic field created by the reduced current. EDFNR was applied to measure the nuclear resonance in the samples under an additional applied current. The current densities achieved were high enough to induce mea-

surable effects in the EDFNR spectra, which are interpreted in the final part.

Keywords: Zero-field NMR, nanostructures, magnetoresistive samples, spin accumulation, electrically excited and detected FNR.

Contents

1	Introduction	1
2	Design of the NMR experiment	9
2.1	NMR in ferromagnets	9
2.1.1	NMR Hamiltonian	10
2.1.2	The hyperfine field	11
2.1.3	The enhancement factor	13
2.2	Effect of spin accumulation on the NMR	13
3	Samples and characterization	19
3.1	Sample design	20
3.1.1	Granular sample (CIP configuration)	20
3.1.2	Multilayered sample (CPP configuration)	21
3.2	Co/Ag and Co/Cu granular samples	24
3.2.1	Fabrication	24
3.2.2	Giant magnetoresistance and magnetic characterizations	26
3.3	Co/Ag, Co/Au and Co/Cu multilayered nanowires	32
3.3.1	Fabrication	32
3.3.2	Characterization by electron microscopy	33
3.3.3	Giant magnetoresistance and magnetic characterization	34
3.3.4	Longer nanowires interconnected in series	36
3.4	Co/Cu interconnected pillars in series	37
3.5	Conclusions	39
4	Microscopic properties of Co nanostructures by NMR	41
4.1	NMR spectrometer	42
4.2	Number of observed nuclei	43
4.3	Preliminary remarks on ^{59}Co NMR	43
4.4	^{59}Co NMR in multilayered samples	44

4.4.1	Co/Ag and Co/Au nanowires	45
4.4.2	Co/Cu nanowires	49
4.4.3	Co/Cu micro-pillars	50
4.5	^{59}Co NMR in Co/Cu granular samples	51
4.5.1	Co/Cu fabricated at RT	51
4.5.2	Co/Cu fabricated at 573K	56
4.6	Conclusions	60
5	Electrically excited and detected ferromagnetic nuclear resonance	61
5.1	Introduction	61
5.2	Comparison between NMR and electrically excited and detected FNR	62
5.3	Electrically excited and EDFNR under additional bias current	66
5.3.1	Continuous voltage	67
5.3.2	Pulsed voltage	68
5.4	Conclusions	79
6	General conclusions and perspectives	81
A	Samples investigated	85
B	^{55}Mn Zero field NMR in a (Ga,Mn)As thin film	87
C	Electrodeposition of Au nanowires	91
D	SQUID measurements on BaVS_3	95
	Curriculum Vitae	107

List of Figures

1.1	Model of the densities of states of two ferromagnetic films in interfacial contact with a paramagnetic film. In equilibrium, the Fermi levels align (top). When a current is driven through the sandwich the voltage drop across the trilayer depends on the orientations of the magnetizations of the ferromagnetic films (bottom). Inset: Configuration of the measurement and the sandwich structure under consideration. After [3].	3
1.2	Experimental illustration of GMR. After [4].	4
1.3	Schematic of spin accumulation at an interface between a ferromagnetic and a non-magnetic layer (a) spin up and down currents outside the spin accumulation zone; (b) Interfacial splitting of the chemical potentials $E_F \uparrow$ and $E_F \downarrow$. The arrows symbolize the spin flips that control the progressive depolarization of the electron current between the left and the right. After [1].	5
1.4	Result of the Valet-Fert model: position-dependence of the electrochemical potential on a bilayer system for the case of antiparallel arrangement of the magnetizations of two semi-infinite ferromagnetic metals. After [7].	6
1.5	Non-local measurement configuration (top). Electrochemical potential for up and down spins, distances in units of the spin diffusion length; Solid line : electrochemical potential in the absence of spin effects (bottom). After [12].	7

2.1	Density of states $g(E)$ of 4s bands: illustration of the imbalance in population due to spin accumulation (left); splitting of energy bands due to the effect of an applied field B for a spin parallel (+) or antiparallel (-) to B if we consider that the electrons interact with B only via their magnetic moment through the Zeeman interaction (right). E_F is the Fermi energy.	14
2.2	Form of the chemical potential in a multilayer: alternate ferromagnetic (FM) and non-magnetic (NM) layers. After [7].	16
3.1	Sketches of the wide structure of the granular sample studied (left) and of the mask used for the lithography (right).	20
3.2	SEM pictures of one via revealing the pores (left), and top view of a device showing vias interconnected in series with Cu contacts, after electroplating; the caps above the wires are clearly visible (right). Courtesy of Dr. Hanna Yousef, Uppsala University (Sweden).	22
3.3	Picture of the four samples showing the 600 (on the upper left and bottom right sides), 800 (top right) and 1000 (bottom left) square vias.	22
3.4	Picture of the final sample, 10.6 mm long and containing 250,000 multilayered micro-pillars of $10\ \mu\text{m} \times 10\ \mu\text{m}$ connected in series; each pillar is 250 nm thick.	23
3.5	GMR of three different granular systems studied: Co/Ag (top), Co/Cu produced at RT (middle) and at 573K (bottom) and sketches of the current and magnetic field orientations used for each measurement.	27
3.6	GMR of three different Co/Cu granular systems studied: sample 2479 (top), sample 880 (middle) and sample 1880 (bottom) and sketches of the current and magnetic field orientations used for each measurement.	28
3.7	Magnetic characterization for the three different granular systems studied: Co/Ag (a) and (b) and Co/Cu produced at RT (c) and (d) and at 573K (e) and (f). The measurements were performed on films deposited on kapton tape, with the field parallel to the film plane.	29
3.8	Field dependence of magnetization M at $T = 80\text{ K}$ for the Co/Cu films: sample 880 (left) and sample 1880 (right). The solid lines represent the gradient used to calculate χ . The measurements were performed on films deposited on glass, with the field parallel to the film plane.	30

3.9	Field dependence of magnetization M at $T = 80$ K for the Co sample (top) and the Co/Cu films: sample 2442 (middle) and sample 2479 (bottom). The solid lines represent the gradient used to calculate χ . The measurements were performed on films deposited on glass, with the field parallel to the film plane.	31
3.10	TEM micrograph of the Co/Cu sample ARdn4, evidencing the multilayered structure.	33
3.11	Giant magnetoresistance measurement of the Co/Cu multilayered nanowire sample ARdn4 in current perpendicular to plane and magnetic field in plane geometry.	34
3.12	Magnetization as a function of the applied magnetic field at $T = 300$ K for the Co/Cu multilayered nanowire sample ARdn4. The measurement was performed with the field perpendicular to the axis of the wires.	35
3.13	SEM micrograph of homogeneous sub-micron Cu wires, revealed by the etching of about $40 \mu\text{m}$ of the polyimide membrane with the use of an oxygen plasma (left), and STEM darkfield image obtained with the annular dark field detector (ADF) of a Co/Cu multilayered sub-micron wire (right) and electron diffraction pattern of Cu [112] zone axis showing monocrystallinity and the related indexation (inset, right).	36
3.14	Picture of the four samples system, ready for electrodeposition and of the 600 square vias, after Cu electrodeposition, evidencing Cu caps and clearly showing an inhomogeneous growth.	37
3.15	SEM micrograph of the bottom electrodes (left); tapping mode AFM image of the Co/Cu pillars deposited on the bottom contacts (middle) and SEM micrograph of the final contacted structure (right). Courtesy of Dr. Mohamed Abid, SFI Trinity laboratory (Ireland). . .	38
4.1	Probehead allowing current injection, referred to as the “new” probe.	42
4.2	RF output for one of the 8 phases of the sequence used and position of the echo in the acquisition window.	43
4.3	Sketches of the resonance circuits used for ^{59}Co zero-field NMR. . .	44
4.4	Zero-field lineshape of ^{59}Co in a Co/Ag multilayered nanowires sample, at $T = 80$ K; the wires are $20 \mu\text{m}$ long. The symbols represent the experimental points and the solid line, the fit. The vertical lines represent the positions of the bulk fcc and hcp Co frequencies. The dashed lines represent the Gaussian peaks comprising the fit.	45

4.5	Zero-field lineshapes of ^{59}Co in different Co/Au multilayered nanowires, at $T = 80\text{ K}$; the wires are $20\text{ }\mu\text{m}$ long. The symbols represent the experimental points and the solid lines, the fit. The vertical lines represent the positions of the bulk fcc and hcp Co frequencies. The dashed lines represent the Gaussian peaks comprising the fit.	48
4.6	Zero-field lineshape of ^{59}Co in the Co/Cu multilayered nanowires (sample ARdn4), at $T = 80\text{ K}$; the wires are $6\text{ }\mu\text{m}$ long. The symbols represent the experimental points and the solid line, the fit. The vertical lines represent the positions of the bulk fcc and hcp Co frequencies. The dashed lines represent the Gaussian peaks comprising the fit.	50
4.7	Zero-field lineshape of ^{59}Co in the Co/Cu multilayered micro-pillars, at $T = 80\text{ K}$. The symbols represent the experimental points and the solid line, the fit. The vertical lines represent the positions of the bulk fcc and hcp Co frequencies. The dashed lines represent the Gaussian peaks comprising the fit.	51
4.8	Zero-field lineshape recorded for ^{59}Co in the Co/Cu granular sample deposited at RT, measured at $T = 80\text{ K}$. The inset shows a zoom of the spectrum, for more clarity.	52
4.9	Zero-field lineshapes recorded for ^{59}Co in the Co/Cu granular sample deposited at RT, for several different temperatures (top). The inset shows the lineshapes corrected for the Boltzmann factor and for the frequency dependent factor. NMR frequency of ^{59}Co <i>vs.</i> $T^{3/2}$ obtained for our sample, compared to the results of Jaccarino (bottom).	53
4.10	Spin-echo integral as a function of 2τ values in the Co/Cu granular sample fabricated at RT, measured at 80 K ; the symbols represent the experimental points and the solid line, the fit. The inset shows the pulse sequence used for T_2 measurement; we used $\tau = 5\text{ }\mu\text{s}$	54
4.11	Spin-echo integral as a function of recovery time values in the Co/Cu granular sample fabricated at RT, measured at 80 K ; the inset shows the pulse sequence used for T_1 measurement; we used $\tau = 5\text{ }\mu\text{s}$ (top). Evolution of $1/T_1$ as a function of the temperature for zero external field (bottom). The symbols represent the experimental points and the solid line, the fit.	55
4.12	Zero-field lineshape recorded for ^{59}Co in the Co/Cu granular sample deposited at 573 K , measured at $T = 80\text{ K}$	57

- 4.13 (a) Zero-field lineshapes recorded for ^{59}Co in the Co/Cu granular sample deposited at 573 K, for several different temperatures; (b) Lineshapes corrected for the Boltzmann factor and for the frequency dependent factor; (c) Lineshapes corrected for the Boltzmann factor, for the frequency dependent factor and for T_2 ; (d) NMR frequency of ^{59}Co *vs.* $T^{3/2}$ obtained for our sample. 58
- 4.14 Pulse sequence used for T_1 measurement for the Co/Cu granular sample fabricated at 573 K (top). Illustration of the magnetization recovery at 80 K for different recovery times using the saturation sequence (middle). Evolution of $1/T_1$ as a function of the temperature for zero external field; the symbols represent the experimental points and the solid line, the fit (bottom). 59
- 5.1 Circuit diagram for electrically excited and detected FNR. The rf power from the power amplifier (left) is driven into the sample. The voltage at the contacts of the sample is detected by the receiver arm of a NMR spectrometer. 63
- 5.2 Zero-field amplitude of the voltaic signal of ^{59}Co in the Co/Cu granular sample 2442 *vs.* rf pulse length, for different pulse levels, relative to the maximum output of the rf pulse board. The rf pulses are further amplified with a set gain. At 0 dB, the rf pulse at the output of the power amplifier is of about 6 W. The spin echo sequence uses two pulses of equal lengths and equal phases. We used electrically excited and EDFNR, at $T = 80$ K and $\tau = 10 \mu\text{s}$ 64
- 5.3 Zero-field amplitude *vs.* pulse length for 6 W rf power on Co and Co/Cu (sample 2442) meanders at $T = 80$ K and for comparison, equivalent curve for inductive pick-up of the signal for sample 2442. 64
- 5.4 Lineshapes recorded for ^{59}Co in the Co/Cu granular sample 2442 measured at $T = 80$ K, obtained by standard NMR at zero field (squares) compared to the electrical excitation and detection directly on the sample (circles). The symbols represent the experimental points and the solid line, the fit. The vertical line represents the position of the bulk fcc Co frequency. 65
- 5.5 Zero-field amplitude *vs.* pulse length on the Co/Cu meander (sample 2479) at $T = 300$ K with (squares) and without (triangles) Cu shielding. The measurement was done at 0 dB. 66

- 5.6 Circuit diagram for electrically excited and EDFNR under additional continuous voltage. The rf power from the power amplifier and the continuous voltage I_{DC} provided by a Keithley 2400 current source are driven into the sample. A bias tee is used in order to drive the DC voltage through the sample and the AC voltage at the contacts of the sample is detected by the receiver arm of a NMR spectrometer. 67
- 5.7 Lineshape recorded for ^{59}Co in the Co/Cu granular sample 2442, measured at $T = 80$ K, obtained by electrically excited and EDFNR with no additional voltage (circles) compared to the lineshape obtained under $I_{DC} = 75$ mA (triangles). The symbols represent the experimental points and the solid line, the fit to several gaussians. The inset shows the resistance *vs.* current measurement carried out at $T = 80$ K. 68
- 5.8 Circuit diagram for electrically excited and EDFNR under additional pulsed voltage. The rf power from the power amplifier and the pulsed voltage provided by the amplified TTL pulses coming from the spectrometer are driven into the sample. Low and high pass filters replace the bias tee. The pulsed voltage is driven through the sample and the AC voltage at the contacts of the sample is detected by the receiver arm of a NMR spectrometer. 69
- 5.9 RF output and pulsed voltage sequences used for the experiment; we used $\tau = 5 \mu\text{s}$ (top). Lineshape recorded for ^{59}Co in the Co/Cu granular sample 2442, measured at $T = 80$ K, obtained by electrically excited and EDFNR with no additional voltage (circles) compared to the lineshape obtained under pulsed $I = 75$ mA (squares); the symbols represent the experimental points and the solid line, the fit to several gaussians (bottom). 70
- 5.10 RF output and pulsed voltage sequences used for the experiment (top). Lineshape recorded for ^{59}Co in the Co/Cu granular sample 2479, measured at $T = 80$ K, obtained by electrically excited and EDFNR with no additional voltage (circles) compared to the experimental points obtained under pulsed $I = 1.12$ A (triangles); the solid line represents the fit of the points taken without I (bottom). 71

- 5.11 RF output and pulsed voltage sequences (a), (b) and (c) used for the different experiments (**I**). Spin echo integral of ^{59}Co in the Co/Cu granular sample 2479 (**II**) and in the sample 880 (**III**) for several pulsed voltages configurations (a) to (c) as a function of the current I ; The measurements were done at $T = 80$ K by electrically excited and EDFNR, at the resonance frequency. 72
- 5.12 RF output and pulsed voltage sequences used for the experiment (left). Comparison of the normalized spin echo integral of ^{59}Co in the Co and Co/Cu (granular sample 2479) meander structures for several pulsed voltages I as a function of the length of the pulse t ; The measurement was done at $T = 80$ K by electrically excited and EDFNR, at the resonance frequency 217 MHz; The symbols represent the experimental points and the solid line, the fit with gaussians (right). 73
- 5.13 Normalized spin echo integral of ^{59}Co in the Co and in the different Co/Cu meander structures for voltages pulsed during $t = 4 \mu\text{s}$ after the first rf pulse as a function of the field. We used $\tau = 10 \mu\text{s}$. The measurements were done at $T = 80$ K by electrically excited and EDFNR, at the resonance frequency. 74
- 5.14 Normalized spin echo integral of ^{59}Co in the 350 nm thick Co with a “wide” meander structure for voltages pulsed during a time t after the first rf pulse as a function of t for two different currents. We used $\tau = 20 \mu\text{s}$. The measurements were done at $T = 80$ K by electrically excited and EDFNR, at the resonance frequency. The solid lines represent the fit to equation 5.9 and lead to the given values of B . . . 75
- 5.15 Normalized spin echo integral of ^{59}Co in the different Co/Cu meanders (a), (b), (c) and (d) for voltages pulsed during a time t after the first rf pulse as a function of t for different currents. We used $\tau = 20 \mu\text{s}$. The measurements were done at $T = 80$ K by electrically excited and EDFNR, at the resonance frequency. The solid lines represent the simulations obtained with equation 5.9 with B calculated using $\alpha = \alpha(0.5 \text{ A})$; the squares correspond to $I = 0.13 \text{ A}$, the circles to 0.295 A , the diamonds to 1 A and the triangles to 1.5 A 77

5.16	Normalized spin echo integral of ^{59}Co in the different Co/Cu meanders (a), (b), (c) and (d) for voltages pulsed during a time t after the first rf pulse as a function of t for different currents. We used $\tau = 20 \mu\text{s}$. The measurements were done at $T = 80 \text{ K}$ by electrically excited and EDFNR, at the resonance frequency. The solid lines represent the simulations obtained with equation 5.9 with B calculated using $\alpha = \alpha(0.13 \text{ A})$; the squares correspond to $I = 0.13 \text{ A}$, the circles to 0.295 A , the diamonds to 1 A and the triangles to 1.5 A	78
B.1	Spin echoes observed in the (Ga,Mn)As thin film, at $T = 8 \text{ K}$ and $f = 245 \text{ MHz}$. The detection method differs: standard NMR (dashed line) and electrical detection (solid line).	88
B.2	Zero-field lineshape of ^{55}Mn in the (Ga,Mn)As thin film, at $T = 8 \text{ K}$. The symbols represent the experimental points and the solid line, the fit.	89
C.1	(A) Schematic illustration of the microchannel network fabrication with embedded Au nanowires 3-D arrays; (B) SEM-FEG micrograph of the Au nanowires after selective plasma etching of polycarbonate; (C) SEM micrograph of the microchannel containing the metallic nanowires.	93

List of Tables

3.1	Number of Co atoms contained in a 600, 800 and 1000 vias sample. .	23
3.2	Characteristics of the Co/Ag and Co/Cu samples studied. LD stands for large distribution.	25
3.3	Characteristics of the Co and Co/Cu samples studied.	26
3.4	Magnetic Susceptibilities χ determined at 80 K for the different sam- ples of interest.	30
4.1	T_1 and T_2 relaxation times as a function of the temperature T for the Co/Cu granular sample fabricated at RT. T_1 and T_2 were measured at the maximum of the NMR line.	54
4.2	T_1 and T_2 relaxation times as a function of the temperature T for the Co/Cu granular sample fabricated at 573 K. T_1 and T_2 were measured at the maximum of the NMR line.	58
A.1	Main samples investigated during this thesis work.	85

Chapter 1

Introduction



Electrons possess a charge and a spin. By analogy to electronics, where charges are manipulated through an electric field, a new field of research has emerged, exploiting the spin and its influence on the electrical conduction in ferromagnets: **spintronics**, short for “spin-based electronics”. This emerging field is nowadays in rapid development.

The technical basis of spintronics goes back to the mid-1930s, when Mott proposed the spin-dependent conduction: ferromagnetic materials doped with impurities exhibited anomalous resistivity trends. The resistance of ferromagnets being a complex function of their impurities has been explained with a two spin-channel model. This model treats the charge carriers - spin up \uparrow and down \downarrow electrons - as relatively independent families between which spin-flip scattering rarely occurs. \uparrow and

Image above adopted from: “Putting electronics in a spin”, by Jonathan Fildes
<http://news.bbc.co.uk/1/hi/technology/6935638.stm>.

\downarrow represent respectively majority and minority spin directions, *i.e.* spin antiparallel and parallel to the local magnetization. We underline here that in the magnetic metals community, “spin up” and “majority spin” are synonymous and refer to the electron *magnetic moment* which is *antiparallel* to the electron *spin* for Fe, Ni and Co. Indeed, for a free electron: $\vec{\mu} = -g\mu_B\vec{s}/\hbar$, where $|\vec{s}| = \hbar/2$.

The conduction by the two independent channels is assumed to be parallel, if we do not take spin-mixing contribution into account.

An essential ingredient for spintronics is the very different density of states of the two different electron spins in a ferromagnetic metal. Any current that flows is primarily mediated by s-electrons, due to their smaller effective masses compared to the d-electron masses. However, the d-electrons present a very different density of states due to the splitting caused by the exchange interaction. Hence, the most frequent scattering event is from “s” electrons to “d” electrons. Consequently, the mobilities of the channels \uparrow and \downarrow are very different. Thus, a current flowing in a ferromagnetic metal with both s-like and d-like character at the Fermi surface E_F would be mediated primarily by the high mobility carriers, *i.e.* the majority carriers, which present the higher occupation number at the Fermi level. One must then expect spin-dependent conductivities. A major consequence of the spin-dependent conductivities is the ability to generate a spin-polarized current by passing a current from a ferromagnet to a paramagnet, as discussed below.

The 2007 Nobel Prize for Physics was awarded to Albert Fert [1] and Peter Grünberg [2] for “the discovery of giant magnetoresistance (GMR)”. GMR was discovered in thin films made of alternating magnetic and non-magnetic layers and is at the root of spintronics. This phenomenon occurs when conduction takes place in nanostructured materials where magnetic materials alternate with non-magnetic metals over distances shorter than the spin diffusion length l_{sf} (see below). A clear understanding of the GMR was given by Johnson [3]. In his description, Johnson uses the electron *spin* to establish a model of the density of states of multilayered magnetic/non magnetic/magnetic films. This model is simplified by giving the bands a simple shape and by allowing one spin subband to be entirely below E_F . At equilibrium, when no current is applied, the Fermi levels align (Figure 1.1 top). Let us now consider a current flowing perpendicularly to the interfaces, from the ferromagnet F1 to F2 (Figure 1.1 bottom). In F1, only electrons in the spin-up subband are available for transport, as they are near E_F . In this configuration, the current passing across the interface between the ferromagnet F1 and the paramagnet P will be spin-up polarized, if we consider that no spin-flip events occur.

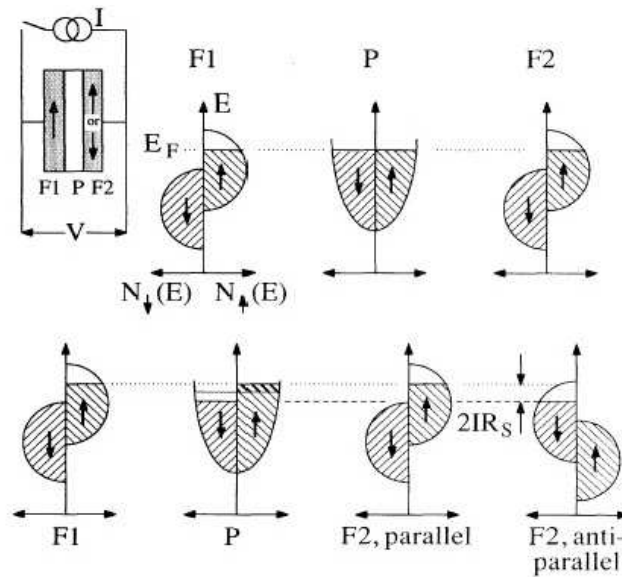


Figure 1.1: Model of the densities of states of two ferromagnetic films in interfacial contact with a paramagnetic film. In equilibrium, the Fermi levels align (top). When a current is driven through the sandwich the voltage drop across the trilayer depends on the orientations of the magnetizations of the ferromagnetic films (bottom). Inset: Configuration of the measurement and the sandwich structure under consideration. After [3].

Thus, the chemical potential of the spin-up subband in P will be raised above its equilibrium value, which will be compensated by a lowering of the spin-down subband. The rise of spin-up in P will have a back-effect on F1, by raising its chemical potential. If the magnetizations of the two adjacent ferromagnetic layers F1 and F2 are parallel, the chemical potential of F2 will also rise to align with that of the spin-up subband of P. Therefore, in this configuration the spin-up will have a highly conducting path, thus lowering the overall resistivity of the layers. However, if the magnetization of F2 is antiparallel to the one of F1, then its chemical potential will align with that of the spin-down subband of P and the chemical potential of F2 is lowered with respect to equilibrium. Consequently, each spin channel has to go through a combination of a path with a large conductivity and with a small one. A higher resistivity of the layers will be measured. Applying a magnetic field to the sample allows the magnetic layer to be changed from the anti-parallel state to the parallel state.

The historical data of the first observation of GMR by the group of A. Fert is given in Figure 1.2. Interest in GMR was stirred both in the research community as a challenge to understand spin-dependent transport and for its commercial applications, leading to an improvement of read heads sensibilities of computer hard disks and contributing to an increase in data storage density, but also for industrial

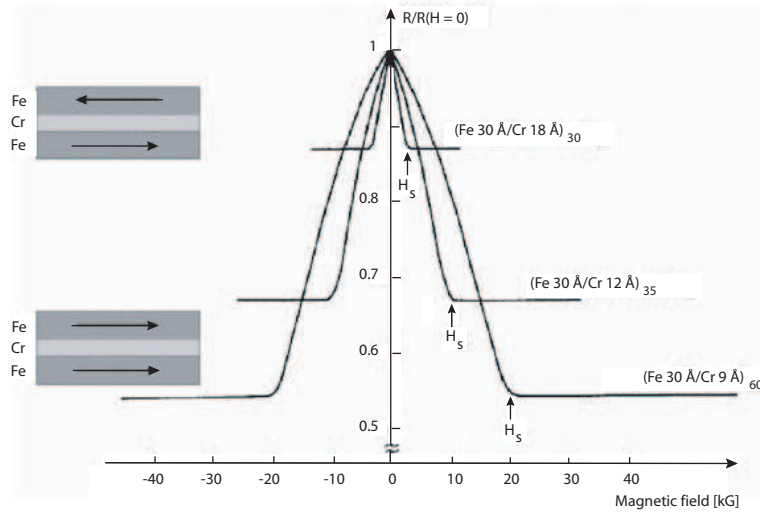


Figure 1.2: Experimental illustration of GMR. After [4].

sensors and devices.

Depending on how the current flows with respect to the metallic multilayer, there are two configurations: current in plane (CIP) [4, 5] and current perpendicular to plane (CPP) [6]. The CPP-GMR has revealed spin accumulation effects, governing the propagation of a spin-polarized current through a succession of magnetic and non-magnetic layers. Spin accumulation determines the exchange coupling between current and magnetization that is presently under investigation by various groups worldwide. It is a consequence of the spin dependence of the conductivity of ferromagnetic metals, which is responsible for the GMR effect. It has been described theoretically in [7]. In that paper, Valet *et al.* used a Boltzmann description of spin-dependent transport, which extended the standard treatment by assuming spin-dependent distributions for \uparrow and \downarrow spins, and using distinct, spin-dependent electrochemical potentials.

The physics of spin accumulation is explained in Figure 1.3, where electrons are flowing from the magnetic to the non-magnetic metal. Far from the interface in the ferromagnet, the spin up current is larger than the spin down while on the other side, far from the interface, the current is equally distributed between both spins. Therefore, there is an accumulation of spin up carriers at the interface and depletion of spin down carriers. This can be seen as a splitting $\Delta\mu$ between the Fermi energies (chemical potentials) of the spin up and spin down electrons. Spin accumulation decays exponentially away from the interface on a length scale called the spin diffusion length. Throughout [7], the authors considered the spin diffusion length to be much larger than the mean free path ($l_{sf} \gg \lambda$). An estimation of l_{sf} in

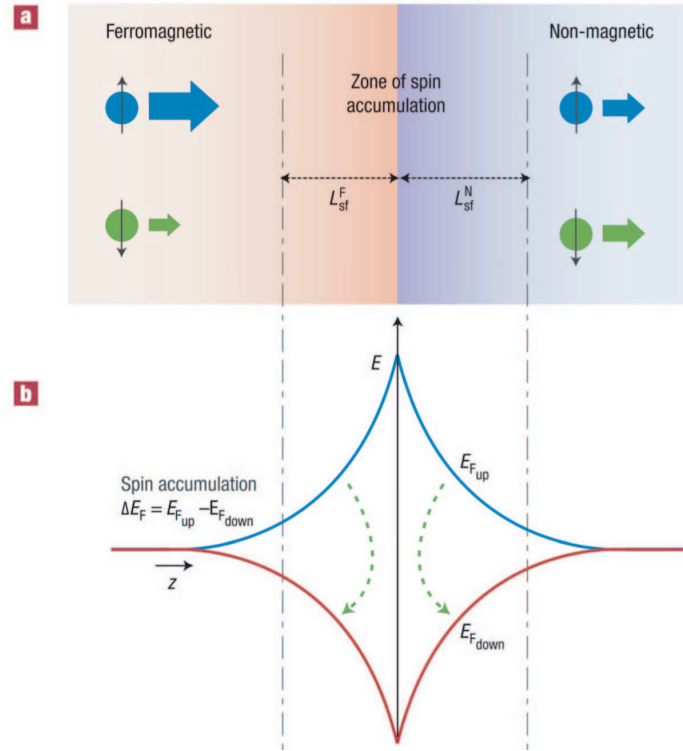


Figure 1.3: Schematic of spin accumulation at an interface between a ferromagnetic and a non-magnetic layer (a) spin up and down currents outside the spin accumulation zone; (b) Interfacial splitting of the chemical potentials $E_F \uparrow$ and $E_F \downarrow$. The arrows symbolize the spin flips that control the progressive depolarization of the electron current between the left and the right. After [1].

the Co layers was given by Piraux [8], from CPP-GMR data on Co/Cu multilayers: he found a value of about 60 nm at low temperature, getting down to about 40 nm at room temperature.

How large is a typical value for spin accumulation for multilayered nanowires? According to T. Valet *et al.* [7] (Figures 1.3 and 1.4), the maximum of the spin accumulation is at $z = 0$, *i.e.* at the interface between the two ferromagnetic metals. A numerical estimate of $\Delta\mu_{int} = \Delta\mu = \beta e \rho_F^* l_{sf}^F j$ is now given. β is the bulk spin asymmetry coefficient which measures the spin asymmetry of the Co resistivity and equals 0.36, according to [8], for Co/Cu multilayered nanowires produced by electrodeposition. We take $\rho_F^* = 6 \times 10^{-7} \Omega.m$ from the same reference; e is the electron charge and we substitute the typical number: $l_{sf}^F = 60 \times 10^{-9} m$ for Co. $\Delta\mu$ is proportional to the current density j : $\Delta\mu = r j$, where $\Delta\mu$ is in V, r is the interface resistance in $\Omega.m^2$ and j is in A/m^2 . A reasonable value for j is the experimental, approximate limit beyond which one has to worry about electro-migration, namely $j = 10^{10} A.m^{-2} = 10^6 A/cm^2$. This leads to $\Delta\mu = 1.3 \times 10^{-4} eV$,

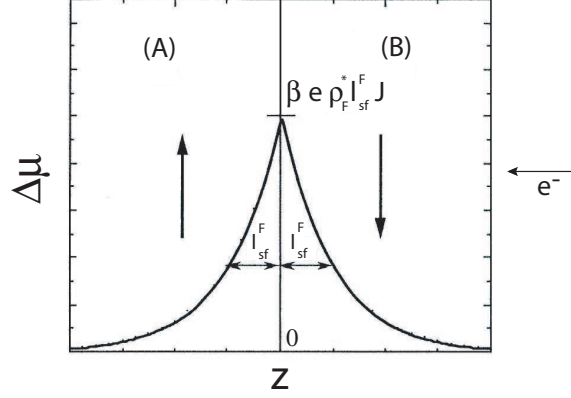


Figure 1.4: Result of the Valet-Fert model: position-dependence of the electrochemical potential on a bilayer system for the case of antiparallel arrangement of the magnetizations of two semi-infinite ferromagnetic metals. After [7].

which is the maximum possible value for $\Delta\mu$, at the interface. The minimum value, *i.e.* $\Delta\mu = 1.3 \times 10^{-5}$ eV is found by taking the resistivity of pure Co, $\rho_F^* = 6 \times 10^{-8}$ $\Omega\cdot\text{m}$. Therefore, we have for our samples:

$$1.3 \times 10^{-5} \text{ eV} < \Delta\mu \leq 1.3 \times 10^{-4} \text{ eV}$$

Whereas spin accumulation is conceptually evident, its experimental verification by direct measurement turns out to be a challenge. Direct evidence for spin accumulation comes from transport measurements. It was measured for the first time by Johnson and Silsbee [9] by using ferromagnetic/non-magnetic interfaces. To do so, they relied on a three terminal device in order to distinguish spin currents from charge currents. Nowadays, such measurements are carried out in configurations such as the one of Figure 1.5, referred to as non-local measurements [10, 11, 12]. A current I is driven into one ferromagnetic electrode (Co1) while the potential V of a second nearby electrode (Co2) is monitored at zero current. The current I is collected in a third electrode away from the voltage electrode. This measurement is analogous to a three-electrode configuration in an electrochemical measurement. If a non-zero voltage is detected, it must come from the electrochemical potential arising from spin accumulation effects.

A magnetic demonstration of spin accumulation was achieved with a non-local spin valve [13]. The accumulation of spins is thought to have caused the flipping of the magnetization of a nanomagnet positioned at the voltage-probing electrode. In this type of measurement of course, experimental arguments are needed to show that the current itself is not the cause of the switch.

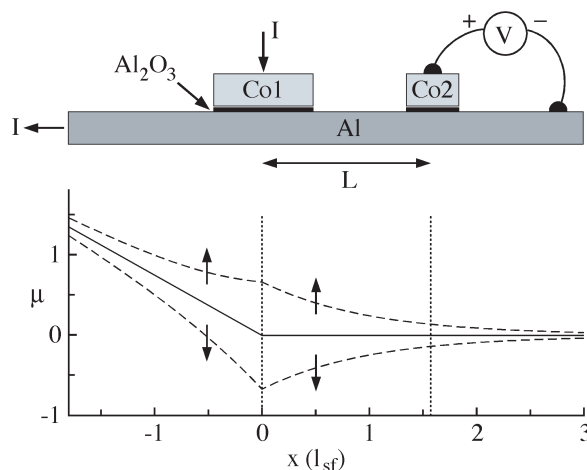


Figure 1.5: Non-local measurement configuration (top). Electrochemical potential for up and down spins, distances in units of the spin diffusion length; Solid line : electrochemical potential in the absence of spin effects (bottom). After [12].

The physics of spin accumulation is of great interest, as it plays an important role in many fields of spintronics. For instance, it remains one of the great challenges of spintronics using semiconductors to inject and modulate spin-polarized carriers electrically, without the application of external magnetic fields.

This thesis is devoted to a search by nuclear magnetic resonance (NMR) for evidence of the spin accumulation at interfaces between non-magnetic and ferromagnetic layers. NMR offers the possibility to use the nuclear spin as a *local* probe. Therefore this search aims to provide a local characterization of spin accumulation, independent of transport measurements and models.

Chapter 2

Design of the NMR experiment



2.1 NMR in ferromagnets

NMR is a powerful tool for the study of ferromagnetism, as the nuclei can be seen as probes of the electronic structure, due to the hyperfine field. In our case, *i.e.* for ^{59}Co -NMR, the magnetic moment is carried by the ion of interest. This makes the NMR of ferromagnets more complex than standard NMR, as the unpaired 3d-electron spins are the source of an effective magnetic field that affects the nuclei. This spontaneous field is the hallmark of NMR in ferromagnets. Due to the hyperfine field, NMR experiments can be performed without an external magnetic field.

Image above adopted from: <http://www.waite.adelaide.edu.au/NMR/NMR.htm>.

A magnet can be used but is not required. The Zeeman splitting of the nuclear spin states is mainly due to the internal hyperfine field.

We give in this section a brief review of the peculiarity of NMR in ferromagnets, by expressing the NMR Hamiltonian, addressing the hyperfine field and the enhancement factor.

2.1.1 NMR Hamiltonian

NMR consists of the excitation and detection of transitions between nuclear energy levels. The resonance frequencies observed correspond to the transition frequencies between eigenstates of the nuclear Hamiltonian:

$$\hat{\mathcal{H}}_{nuclear} = \hat{\mathcal{H}}_{Zeeman} + \hat{\mathcal{H}}_{quadrupole} + \hat{\mathcal{H}}_{electron-nucleus} + \hat{\mathcal{H}}_{internuclear} \quad (2.1)$$

A review of the four terms is given in [14].

The first term of (2.1) corresponds to the interaction of the nucleus with the external magnetic field. In NMR of ferromagnets, no external field is needed to lift the degeneracy of the nuclear spin levels. Due to the spontaneous magnetization, this can be achieved by the internal local field felt by the nuclear spin, that can be approximated to be the hyperfine field. We performed zero-field NMR in this thesis work.

Nuclei having spins larger than $I = \frac{1}{2}$ present a nuclear electric quadrupole moment. This moment can interact with the electric field gradients created by the crystal structure. In the case of a cubic environment, no effect of the electric field gradient is expected to be seen on the nuclei. Nevertheless, defects such as vacancies or deformations can lower the symmetry and could give rise to a quadrupolar splitting of the spin levels.

We refer to the interaction of the nuclear spin of a magnetic atom with its own uncompensated 3d (or 4f) electron shell as the hyperfine (hf) interaction. This has to be distinguished from the interaction between the nuclear spin and electron shells of foreign magnetic atoms, for which the main source is often the dipole-dipole interaction, which is a direct internuclear interaction. Indirect internuclear interactions can also take place via the electron spins (RKKY interactions with conduction electrons and Suhl-Nakamura interactions with virtual magnons).

For a magnetically ordered material and without an applied magnetic field, we can express the total effective field sensed by a nucleus as follows:

$$\mathbf{B}_{tot} = \mathbf{B}_{hf} + \mathbf{B}_{dipolar} \quad (2.2)$$

where \mathbf{B}_{hf} is the mean static hyperfine field used to describe the hyperfine coupling in Co atoms and $\mathbf{B}_{dipolar}$ is the dipolar field arising from the dipole-dipole interaction between the nuclear magnetic moment and the atomic magnetic moments of all the other atoms in the solid. This total effective field leads to a nuclear energy level splitting ΔE of magnitude $\Delta E = hf_{res} = \hbar\gamma |\mathbf{B}_{hf} + \mathbf{B}_{dipolar}|$ where f_{res} is the NMR resonance frequency.

2.1.2 The hyperfine field

The hyperfine field is due to the interaction of the nuclear spin with the net electron magnetization and lifts the degeneracy of the nuclear spin levels. It can be expressed as:

$$\hat{\mathcal{H}}_{hf} = \hat{\mathbf{I}} \cdot A \hat{\mathbf{S}} \quad (2.3)$$

where $\hat{\mathbf{I}}$ is the nuclear spin operator, A is the hyperfine interaction constant and $\hat{\mathbf{S}}$ is the total spin operator of the atom. According to [15], when the surroundings of the lattice sites where the nuclei are located is not of cubic symmetry, the parameter A is a tensor of second rank possessing the corresponding symmetry. Since in solids the electronic spin moment flipping time is very short compared to the time needed by a nuclear spin to achieve one Larmor precession, the nucleus feels an effective spin moment $\langle \mathbf{S} \rangle$. Equation (2.3) can then be written as

$$\hat{\mathcal{H}}_{hf} = \hbar\gamma_n \mathbf{B}_{hf} \cdot \hat{\mathbf{I}} \quad (2.4)$$

where γ_n is the nuclear gyromagnetic ratio and \mathbf{B}_{hf} is given by:

$$\mathbf{B}_{hf} = \frac{1}{\hbar\gamma_n} A \langle \mathbf{S} \rangle \quad (2.5)$$

In magnetically ordered materials, $\langle \mathbf{S} \rangle$ is significantly different from zero and for Co, \mathbf{B}_{hf} attains a value of 22 T.

It is the spatial distribution of electron spin polarization close to the observed nucleus that leads to the hyperfine field. \mathbf{B}_{hf} is the sum of three contributions [16]:

$$\mathbf{B}_{hf} = \mathbf{B}_{hfcontact} + \mathbf{B}_{hfdipolar} + \mathbf{B}_{hforbital} \quad (2.6)$$

where

- $\mathbf{B}_{hfcontact}$ is the Fermi contact field [17], which originates from the spin polarization of all electrons, essentially the s-shells within the volume of the nucleus. This contribution is the largest contribution to the hyperfine field, for 3d-ferromagnetic materials:

$$\mathbf{B}_{hfcontact} = \frac{8\pi}{3}\mu_B\mathbf{m}(0) \quad (2.7)$$

where $\mathbf{m}(0)$ is the spin density at the nucleus. From equation (2.7), the contact field vanishes unless there is an imbalance at the nuclear site between the spin up and the spin down electron densities. Core polarization occurs due to the majority s electrons that will be pulled into the region of the spin polarized 3d shell since the exchange interaction is attractive. This results in an excess of minority electrons at the nuclear position, *i.e.* a negative polarization (antiparallel to the local moment). The spin polarization arising from 4s electrons has two sources: the repopulation effect due to the presence of the 3d moment that leads to more majority and less minority occupied 4s states and therefore to a positive local contribution to $\mathbf{B}_{hfcontact}$; and the hybridization of the valence 4s wave functions with the spin polarized 3d wave functions of the neighboring atoms induces a weak 4s valence polarization leading to a transferred polarization. As the transferred contribution depends essentially on the magnetic moment of the neighboring atoms, the contact field is made sensitive to the local environment.

- $\mathbf{B}_{hfdipolar}$ is the dipolar field from electrons outside the nucleus volume, *i.e.* the spin density of the d-shell, which vanishes for sites with cubic symmetry.
- $\mathbf{B}_{hforbital}$ is the orbital field, which is not expected in a cubic environment either, due to the quenching of the orbital angular momentum. However, a small orbital moment can be induced due to spin-orbit coupling. This leads to a positive orbital hyperfine field, as the orbital moment is parallel to the spin moment for a more than half filled d shell, *i.e.* opposite to the contact field.

The hyperfine field is indicative of the local environment of the nucleus: the different phases present, if any and defects. Therefore, the NMR spectrum reflects the distribution of frequencies due to the distribution of local environments around the nuclei. As we already mentioned, Co can be found in two phases: hexagonal close packed (hcp) and face centred cubic (fcc). These two structures present different local hyperfine fields and it is therefore possible to discriminate between them (see

Chapter 4). The hyperfine field not only makes possible the detection of a NMR signal without any external field applied at the Larmor frequency $\omega_I = \gamma |B_{hf}|$ of the nuclei considered but also gives rise to an enhancement of the radio-frequency (rf) power both in excitation and in detection (see below).

2.1.3 The enhancement factor

In ferromagnets, it is the dynamic component of the hyperfine field induced by the applied rf field that excites the resonance rather than the external applied rf field itself [18, 19]. As $\gamma_e \simeq 10^3 \gamma_n$, radio-frequencies are almost static for the electron spins and the electron magnetization follows the applied rf magnetic field B_1 . Therefore, the nuclei feel the motion of the electron spins along B_1 *i.e.* a rf field B_{rf} that is very much larger than the external rf field: $B_{rf} = B_1 + \eta B_1$, where η is the enhancement factor, depending on the strength of the hyperfine coupling and ηB_1 is the field contribution due to the electronic magnetization. As usually $\eta \gg 1$, $B_{rf} \simeq \eta B_1$.

Moreover, after the rf excitation, the nuclei precess in the plane perpendicular to the effective field and this precession acts on the electron spins. As $\gamma_e \simeq 10^3 \gamma_n$, the electron spins follow the nuclear spins and it can be shown [15] that the e.m.f. created in the receiver coil by the electron spins is η times larger than the one created by the nuclear spins. Consequently, in ferromagnets, there is an enhancement of the signal both in excitation and in detection.

The enhancement factor gives rise to tremendously enhanced signals and we only need a low power level to flip the nuclear spins. As a consequence, the rf pulses used can be short (few hundred ns), which allows an excitation over a large range of frequencies. This is very convenient for us, as we are working with broad spectra (see chapter 4).

2.2 Effect of spin accumulation on the NMR

In this section, we give a quantitative estimate of the frequency shift and broadening that we could expect in the ^{59}Co -NMR line due to spin accumulation by using a formalism similar to the one used for Pauli paramagnetism in a non-magnetic metal.

We consider conduction electrons as an ensemble of spins $\frac{1}{2}$. We use the notation \pm for the absolute spin direction, $s_z = \pm \frac{1}{2}$. The energy levels $m = \frac{1}{2}$ and $m = -\frac{1}{2}$ split under a static homogeneous applied magnetic field. The populations of the lev-

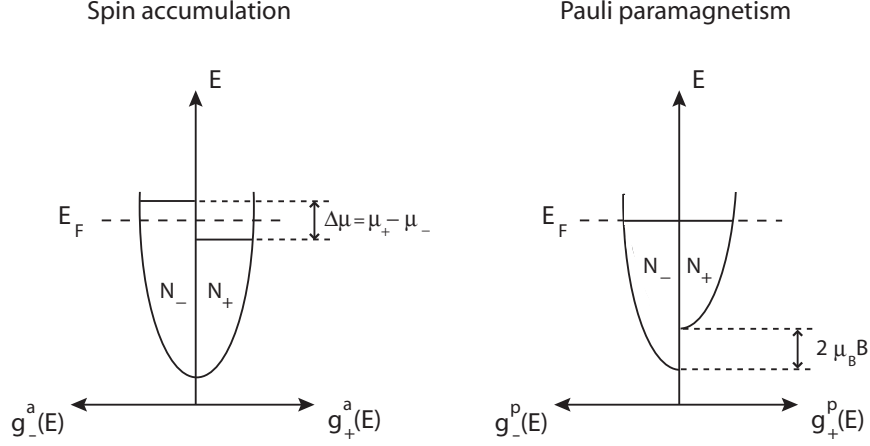


Figure 2.1: Density of states $g(E)$ of 4s bands: illustration of the imbalance in population due to spin accumulation (left); splitting of energy bands due to the effect of an applied field B for a spin parallel (+) or antiparallel (-) to B if we consider that the electrons interact with B only via their magnetic moment through the Zeeman interaction (right). E_F is the Fermi energy.

els are N_+ and N_- and the total amount of conduction electrons is: $N = N_+ + N_-$.

The polarization of the electronic spins can be written as: $\Delta N = N_+ - N_-$.

We introduce the density of states $g(E)$ of the electrons. Spin accumulation (a) will generate an imbalance in population, which can be compared to Pauli paramagnetism (p), as illustrated in Figure 2.1.

As the spin bands are assumed identical, the spin-dependent density of states for the spin accumulation is given by:

$$g_{\pm}^a(E) = \frac{1}{2} g(E) \quad (2.8)$$

In this case, we assume two spin populations in thermodynamic equilibrium with the bath, but not among themselves, that is, we write:

$$N_{\pm}^a = \int dE g_{\pm}^a(E) f_{FD}(E, \mu_0 \mp \frac{\Delta\mu}{2}) \quad (2.9)$$

where

$$f_{FD}(E, \mu_0) = \frac{1}{1 + e^{(E - \mu_0)/(k_B T)}} \quad (2.10)$$

and the second argument of f_{FD} in (2.9) is the Fermi level.

We can change the variable of integration, posing $E' = E \pm \frac{\Delta\mu}{2}$:

$$N_{\pm}^a = \int dE' \frac{1}{2} g(E' \mp \frac{\Delta\mu}{2}) f_{FD}(E', \mu_0) \quad (2.11)$$

We can compare this result with the one that is obtained when deriving Pauli paramagnetism, where the spin bands are shifted by the Zeeman splitting due to an applied field B. Thus, their density of states is:

$$g_{\pm}^p(E) = \frac{1}{2} g(E \mp \mu_B B) \quad (2.12)$$

As the spin system is assumed to have reached equilibrium in the field B, the Fermi level remains μ_0 for both spin bands. We therefore have the following spin populations in the Pauli paramagnetism case:

$$N_{\pm}^p = \int dE \frac{1}{2} g(E \mp \mu_B B) f_{FD}(E, \mu_0) \quad (2.13)$$

Equations (2.11) and (2.13) are similar.

In the paramagnetism case, we have $\mu_B B \ll E_F$, where E_F is the Fermi energy in zero field and in the spin accumulation case, we have, according to our calculation of $\Delta\mu$ (see Chapter 1): $\frac{\Delta\mu}{2} \ll \mu_{eq} \simeq E_F = \frac{1}{2} m_e v_F^2 = 3 \text{ eV}$. According to [20]:

$$M^p = -\mu_B (N_+^p - N_-^p) = \mu_B (\mu_B B) g(E_F) \quad (2.14)$$

Therefore, for the spin accumulation we have:

$$M^a = -\mu_B (N_+^a - N_-^a) = \mu_B (\frac{\Delta\mu}{2}) g(E_F) \quad (2.15)$$

From (2.14) and (2.15), we get:

$$\frac{M^a}{M^p} = \frac{\Delta\mu}{2\mu_B B} = \frac{B^a}{B} \quad (2.16)$$

where B^a is defined here as the effective field that would have to be applied to the nuclei in order to produce by paramagnetism as much spin polarization as the spin accumulation does.

By taking $\mu_B = 9.27 \times 10^{-24} \text{ J/T}$ and $\Delta\mu = 1.3 \times 10^{-4} \text{ eV}$ (see Chapter 1) we get:

$$B_{max}^a = \frac{\Delta\mu}{2\mu_B} = \frac{1.3 \times 10^{-4} \times 1.6 \times 10^{-19}}{2 \times 9.27 \times 10^{-24}} = 1.1 \text{ T}$$

And for $\Delta\mu = 1.3 \times 10^{-5} \text{ eV}$, we have $B_{min}^a = 0.11 \text{ T}$.

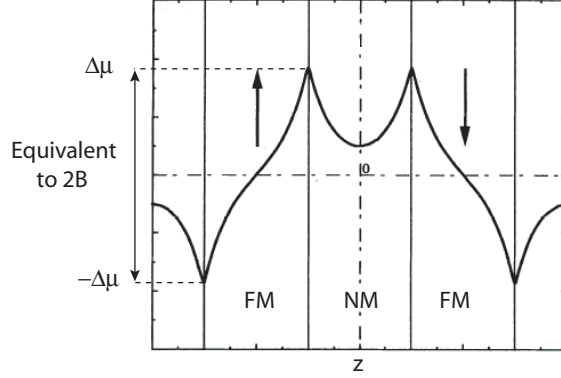


Figure 2.2: Form of the chemical potential in a multilayer: alternate ferromagnetic (FM) and non-magnetic (NM) layers. After [7].

We stress that the given estimates are optimistic, as we take the maximum value for spin accumulation, *i.e.* the value at the interface instead of taking into account the sinh shape of $\Delta\mu$ in the ferromagnetic layer (see Figure 2.2).

In NMR, the paramagnetic shift of the nuclear resonance is known in the literature as the Knight shift K [21].

$$K = \frac{\Delta f}{f} = \frac{\Delta B^p}{B} = \frac{8\pi}{3} \langle |u_{\mathbf{k}}(0)|^2 \rangle_{E_F} \chi^p \quad (2.17)$$

with $u_{\mathbf{k}}(\mathbf{r})$ is the modulating part of the Bloch function $\psi_{\mathbf{k}} = u_{\mathbf{k}}(\mathbf{r})e^{i\mathbf{k}\cdot\mathbf{r}}$.

According to [22], $K = \frac{\Delta f}{f} = 1.86\%$ in the ferromagnetic hcp phase of Co. Since the nuclei resonate at 226.7 MHz at 80 K, this means that the contribution of the conduction electron spin paramagnetism to this frequency is 4.2 MHz.

From B^a , we can deduce the shift in frequency expected from spin accumulation

$$\Delta f = K \frac{\gamma}{2\pi} B^a \quad (2.18)$$

$$\Delta f_{max} = \frac{1.86}{100} \times 10.054 \times 10^6 \times 1.1 = 0.2 \text{ MHz};$$

$$\Delta f_{min} = 20 \text{ kHz}$$

In a ferromagnet, the chemical potential always has the form depicted in Figure 2.2. Due to the sinh shape of $\Delta\mu$ in the ferromagnetic layer, $\Delta\mu$ varies from $-\Delta\mu$ to $\Delta\mu$. Therefore, the expected effect on the NMR line would be a broadening rather than a shift. The maximum shift has to be compared to the linewidth ob-

tained for ^{59}Co in our Co/Cu multilayered nanowires, *i.e.* 7.7 MHz (see subsection 4.4.2 in Chapter 4). We expect to be able to detect a broadening of a tenth of the linewidth. In the field B^a calculated above, conduction electrons would cause a shift spread over:

$$\Delta = K \frac{\gamma}{2\pi} (2B^a) = 2 \Delta f \quad (2.19)$$

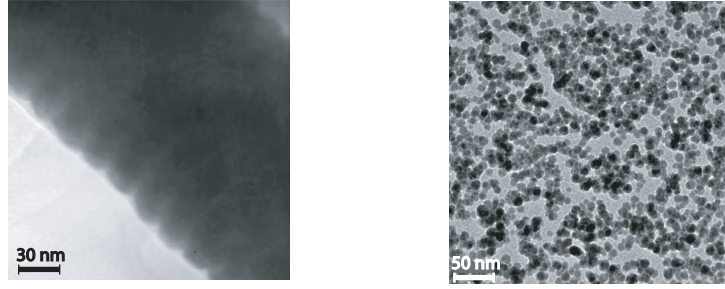
i.e. $\Delta_{max} = 0.4$ MHz and $\Delta_{min} = 0.04$ MHz. Unlike Δ_{min} , we could detect the broadening Δ_{max} directly on the lineshape. In order to detect the spread of frequency Δ_{min} , we could do dynamic measurements. Indeed, Δ_{min} causes a dephasing characterized by:

$$T_2^* = \frac{1}{K} \frac{2\pi}{\gamma} \frac{2\mu_B}{\Delta\mu} = \frac{1}{\Delta f_{min}} \quad (2.20)$$

i.e. $T_2^* = 50 \mu\text{s}$, which is an additional apparent relaxation process due to the voltage injected. This relaxation was measured in our case (see chapter 5).

Chapter 3

Samples and characterization



Producing a sample suitable for the detection of spin accumulation by NMR is a crucial step in this work. Therefore, in this chapter we would like to give a review of different samples which have been considered and of the methods used to characterize their properties.

It is well established that there are two types of materials displaying the giant magnetoresistance (GMR) effect: multilayered systems containing alternating ferromagnetic/non ferromagnetic metal layers [4, 6] and granular thin films containing magnetic impurities (clusters or nanoparticles) in a diamagnetic matrix [24, 25]. In this work, we investigated both types of samples and we characterized them with magnetic and magneto-transport measurements, electron and atomic force microscopies.

Figures above: TEM micrograph of Co/Ag multilayered nanowires, picture adopted from [23] (left); TEM micrograph of Co nanoparticles without the Cu matrix, courtesy of Prof. Antonio Domingues dos Santos, São Paulo University (Brazil) (right).

3.1 Sample design

Three parameters turned out to be of paramount importance for the design of the sample:

- We need to have **at least 10^{17} Co atoms** in order to have a good NMR signal to noise ratio, as shown in section 4.2;
- Co should have a **fcc** structure, as the corresponding peak in the NMR line is narrower than for the hcp. Also, the effect of a current applied to the sample would be more easily detected. It has been shown [26] that by doping the Co layer with Cu during the formation of multilayered nanowires by electrodeposition, Co crystallizes in the fcc phase;
- **a current density of 10^6 A/cm²** (see chapter 1) has to flow through the sample for the spin accumulation effect to be detected by NMR. This is the main limiting parameter and it imposes certain geometrical restrictions, together with the number of Co atoms required.

Two different types of samples that fulfilled the requirements itemized above were fabricated and studied during this thesis: **granular** and **multilayered** ones.

3.1.1 Granular sample (CIP configuration)

The granular samples offered the advantage of being shaped easily, by ultraviolet (UV) lithography. In order to utilize the maximum available surface of the NMR coil, we shaped the samples as meander stripes, as described in subsection 3.2.1. The substrates used for deposition were 2 inches in diameter and the mask used for the lithography is sketched in Figure 3.1 (right).

We considered two structures: a wide one, sketched in Figure 3.1 (left) and a narrow one. The dimensions of the metallic deposits considered were: several hundred nm

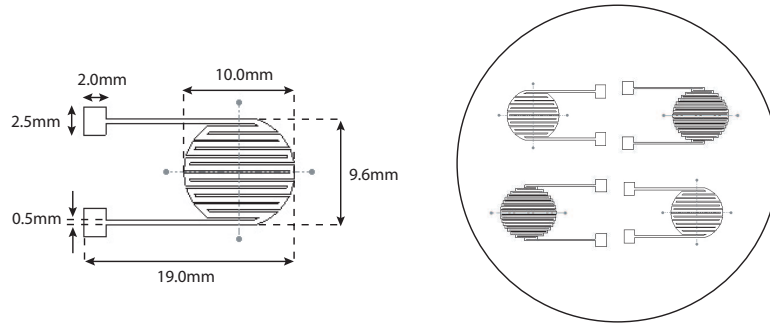


Figure 3.1: Sketches of the wide structure of the granular sample studied (left) and of the mask used for the lithography (right).

in thickness, $w = 0.25$ mm in width for the “narrow” structure; $w = 0.5$ mm in width and 140 mm in total length for the “wide” structure. The concentration of Co nanoparticles in the matrix was either 30 % or 35 %, leading to a total amount of Co atoms inside the NMR coil $> 10^{17}$. If we consider a thickness of 400 nm, these structures imply the injection of 2 A for the wide structure and of 1 A for the narrow one, in order to reach the current densities needed.

3.1.2 Multilayered sample (CPP configuration)

In parallel to the granular systems, we investigated another family of samples in this work: the multilayered one, either in the form of nanowires or micro-pillars. The spin accumulation in these systems, where the current is applied perpendicular to the plane, is larger than for the granular systems, where the current flows in the plane.

Nanowires

If we suppose that the maximum current that we can inject in the sample is $I_{max} = 2$ A, the total sample cross section has to be at a maximum S_{max} with $S_{max} = 2 \times 10^{-6}$ cm². In order to have 10^{17} Co spins, the volume of Co required is $V = 1.1 \times 10^{-6}$ cm³. Since our nanowires are Co/Cu multilayers, this means that we need to have a total length of 1.1 cm! Effectively, we should contact at least 1834 commercial polycarbonate membranes (6 μ m thick) in series, which is not realistic! However, we bypassed this problem by developing a device in a 75 μ m thick polyimide template that fulfills both requirements, the current density and the minimum amount of Co atoms needed in the sample. To do so, we adapted the flexible printed circuit board expressed in [27] to our purpose, in collaboration with Dr. Hanna Yousef and Prof. Klas Hjort of the Materials Department at Uppsala University (Sweden). We designed a lithographed device composed of cavities (vias) (Figure 3.2 (left)), defined by UV lithography and filled with sub-micron sized pores with specific characteristics (pore density, pore diameter, area of one via and number of vias). We sealed one side of the porous template with a Cu layer (the working electrode) which we then isolated in order to prevent deposition on it. We grew the wires by electrodeposition in the pores (220 to 350 nm diameter).

After deposition in such a device, electrical contacts were made on the top and bottom (by use of UV lithography). Thus, the sample consisted of interconnected sub-micron wire bundles **in series**. The top interconnections of Ni wires between two adjacent vias are illustrated in Figure 3.2 (right).

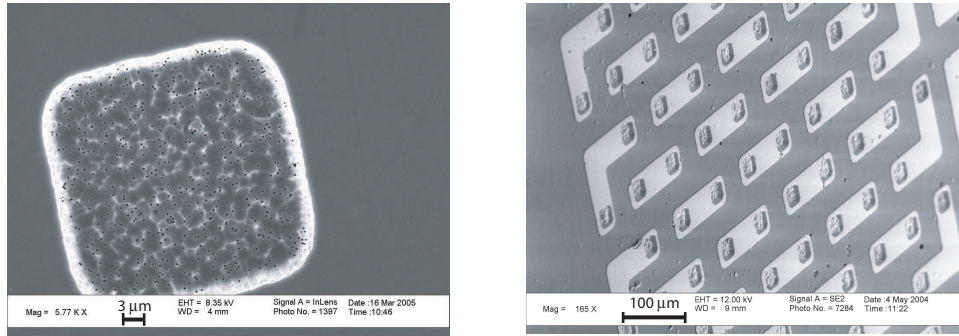


Figure 3.2: SEM pictures of one via revealing the pores (left), and top view of a device showing vias interconnected in series with Cu contacts, after electroplating; the caps above the wires are clearly visible (right). Courtesy of Dr. Hanna Yousef, Uppsala University (Sweden).

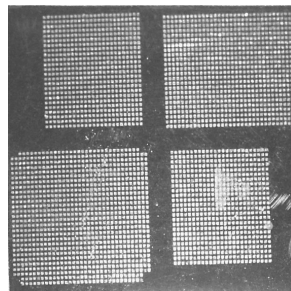


Figure 3.3: Picture of the four samples showing the 600 (on the upper left and bottom right sides), 800 (top right) and 1000 (bottom left) square vias.

Number of vias	Number of Co atoms
600	1.2×10^{17}
800	1.6×10^{17}
1000	2×10^{17}

Table 3.1: Number of Co atoms contained in a 600, 800 and 1000 vias sample.

The final system was composed of 4 different samples lithographed on a single $75 \mu\text{m}$ thick polyimide foil with 1000, 800 and twice 600 square via contacts (Figure 3.3). Each contact has a surface S_c of $120 \mu\text{m} \times 120 \mu\text{m}$, with a center-to-center distance between two contacts of $150 \mu\text{m}$.

The pore density is $d_p = 1.3 \times 10^7$ pores/ cm^2 and the pore diameter 200 nm , leading to a surface for one wire of $S_w = 3.14 \times 10^{-14} \text{ m}^2$. If we inject $I = 2 \text{ A}$ in the sample, the current density would be: $j = \frac{I}{S_c \times d_p \times S_w} = 3.4 \times 10^6 \text{ A/cm}^2$, which is a relevant value for our study. The number of Co atoms contained in each sample is summarized in Table 3.1.

The electrodeposition in such devices will be discussed in the subsection 3.3.4.

Micro-pillars

We also designed another type of multilayered samples, by UV lithography: micro-pillars. The pillars have been contacted in pairs at the bottom and at the top in such a way that we would get a structure **in series**. The final structure is pictured in Figure 3.4. The volume of interest (without the contact pads) had to fit in an area of $7.85 \times 10^{-5} \text{ m}^2$, *i.e.* the maximum surface of the NMR coil. In order to be able to inject 1 A in those samples to get the current density needed, the pillar area was $10 \mu\text{m} \times 10 \mu\text{m}$. The total thickness of a pillar was 250 nm (leading to an effective thickness of 125 nm of Co per pillar) and each metal layer was 5 nm thick. The pillars were spaced at $5 \mu\text{m}$ from one another. There were 250,000 pillars in total, leading to 2.84×10^{17} Co atoms in the sample.

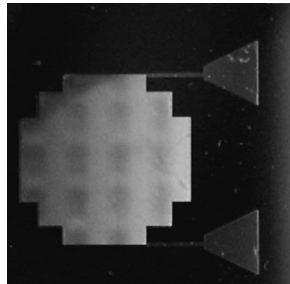


Figure 3.4: Picture of the final sample, 10.6 mm long and containing 250,000 multilayered micro-pillars of $10 \mu\text{m} \times 10 \mu\text{m}$ connected in series; each pillar is 250 nm thick.

3.2 Co/Ag and Co/Cu granular samples

3.2.1 Fabrication

We cleaned the glass and Si substrates successively with acetone, isopropanol and deionized water and dried them for 5 min at 160 °C. In order to improve the adherence of the metallic deposit to be sputtered, we also exposed the glass substrates to an oxygen plasma for 5 min, using the plasmaline 415 in the Institute of Quantum Photonics and Electronics (IPEQ) at EPFL. We used the following conditions: power of 100 W, O₂ flux of 60, pressure: 0.39 torr.

We spin coated the substrates with an adhesion promoter (Hexamethyl-1,1,1,3,3,3-disilazane, Merck), at 5000 rpms for 10 s prior to the spin coating with the photoresist AZ5214E, with the same rotational speed, for 30 s. The thickness of the photoresist at the end of the lithographic process was around 1.4 μm . After 3 min, we softbaked the sample at 90 °C for 3 min, in order to make the resist photosensitive. AZ5214E is a reversible photoresist which can be used both as positive or negative resist. We used it as a negative resist, which means that the areas exposed to UV light will polymerize. Exposure to UV light through the lithography mask was for 1.5 s. This step was followed by a post exposure bake (PEB). The exposed photoresist cross-links on PEB at 115 °C for 2 min and loses its photosensitivity. We achieved an exposure without mask for 15 s, in order to make previously unexposed areas soluble to the developer solution. Finally, the substrates were immersed in the developer (MF319) for 40 s in order to remove the non-exposed photoresist. We rinsed the patterned sample obtained with deionized water and we exposed it to a final oxygen plasma, for 5 min.

The Ag and Cu films containing Co nanoparticles were blanket-deposited at RT all over the substrates, covering the photoresist and areas in which the photoresist has been cleared. This work was done in a DC magnetron discharge by codeposition, meaning that both the nanoparticle gun (Co) and the sputtering gun (Cu, Ag) are working simultaneously. The sputtering has been done through collaborations with Dr. Yuansu Luo in Göttingen University (Germany), for Co/Ag and Prof. Antonio Domingues dos Santos, São Paulo University (Brazil), for Co/Cu.

We ended the process by removing the photoresist by lift-off: we removed the photoresist under the film with acetone, taking the film with it, and leaving only the film which was deposited directly on the substrate.

For the Co/Cu deposited at higher temperature (573 K), the sputtering was made directly on cleaned substrates. The lithography was achieved *after* deposition, using a positive resist (S1813), that was to protect the area of interest (meander

	Co/Ag	Co/Cu	Co/Cu
Name of the sample	3	2	2442, 2479
Temperature of deposition	RT	RT	573 K
Composition	Co ₃₀ Ag ₇₀	Co ₃₅ Cu ₆₅	Co ₃₀ Cu ₇₀
Thickness of the deposit (nm)	400	500	1000, 770
Area of the sample in NMR coil (mm ²)	55.6	85.8	55.6
Area of the entire structure (mm ²)	74.4	98.4	74.4
Number of Co atoms from M(H) curve:	RT	RT	80 K
- in NMR coil ($\times 10^{17}$)	2.5	9.0	5.3, 7.3
- in the entire structure ($\times 10^{17}$)	3.4	10.3	7.1, 9.8
Estimated size of Co nanoparticles (nm)	5	LD	LD
Substrate	Si	Glass	Glass
Lithography before/after deposition	before	before	after
Structure studied	wide	narrow	wide
Si ₃ N ₄ capping layer	no	no	yes

Table 3.2: Characteristics of the Co/Ag and Co/Cu samples studied. LD stands for large distribution.

stripes) from the argon etching. The lithography and etching were made by Dr. Mohamed Abid, in SFI Trinity laboratory (Ireland).

The Table 3.2 summarizes the different characteristics of the granular samples that we investigated. In order to evaluate the thickness of the metallic deposits, we made sure that no photoresist was left over the samples by cleaning them with acetone and then exposing the glass substrates to an oxygen plasma for 5 min, using the plasmaline 415 in IPEQ at EPFL. We used the following conditions: power of 100 W, O₂ flux of 60, pressure: 0.39 torr. We determined the thicknesses with a Surface Profiler, KLA-Tencor Alpha-Step IQ, in IPEQ. We stored the samples 3 and 2 under a N₂ atmosphere, but they got completely oxidized over a period of a month, which was revealed by the loss of the ⁵⁹Co zero-field NMR signal, CoO being antiferromagnetic. In order to prevent aging, storage was under continuous primary pumping and a thin capping layer of Si₃N₄ was sputtered over the samples, except on the contact pads to allow electrical contacts to be made. We also studied a Co reference sample (see subsection 5.3.2) where no spin accumulation is expected. Co was sputtered on glass by Dr. Mohamed Abid. In order to be in similar conditions as for the samples 2442 and 2479, we patterned the Co sample and studied the wide structure. Additional Co/Cu samples differing by about a factor of two in thickness (samples 880 and 1880) were made on glass at higher temperature, to improve the quality. The Table 3.3 summarizes the different characteristics of these three latter samples.

We made the contacts by gluing 0.125 mm thick Au wires with epoxy conductive glue on the contact pads of the samples and then heating the samples for 1 h at

	Co	Co/Cu	Co/Cu
Name of the sample	Co	880	1880
Temperature of deposition	RT	573 K	573 K
Composition	Co	Co ₃₀ Cu ₇₀	Co ₃₀ Cu ₇₀
Thickness of the deposit (nm)	350	880	1880
Area of the sample in NMR coil (mm ²)	55.6	55.6, 85.8	55.6
Area of the entire structure (mm ²)	74.4	74.4, 98.4	74.4
Number of Co atoms from M(H) curve at 80 K:			
- in NMR coil ($\times 10^{18}$)	1.9	1.6, 2.4	2.7
- in the entire structure ($\times 10^{18}$)	2.5	2.1, 2.7	3.6
Lithography before/after deposition	after	after	after
Structure studied	wide	wide, narrow	wide
Capping layer	Ta	Si ₃ N ₄	Si ₃ N ₄

Table 3.3: Characteristics of the Co and Co/Cu samples studied.

150 °C under a N₂ atmosphere.

3.2.2 Giant magnetoresistance and magnetic characterizations

The Co/Ag and Co/Cu granular samples that we studied presented GMR, at room temperature (RT), as illustrated in Figures 3.5 and 3.6. We define the GMR ratio by: $\frac{R_{AP}-R_P}{R_{AP}}$, where R_{AP} is the maximum resistance of the sample, observed when there is an antiparallel coupling between adjacent ferromagnetic layers and R_P the minimum resistance, when the layer magnetizations are all aligned with the direction of the external applied magnetic field. The magnitude and shape of GMR is typical for these types of materials.

We performed the magnetic characterization using a Quantum Design MPMS-7 superconducting quantum interference device (SQUID) magnetometer. The measurements were performed on films deposited either on kapton tape or on glass, with the field parallel to the film plane.

In order to investigate the various magnetic interactions taking place in the samples, we achieved Zero Field Cooled *vs.* Field Cooled (ZFC *vs.* FC) experiments. First, the sample is cooled to liquid He temperatures under no magnetic field applied. Then a small magnetic field (100 Oe) is applied and the net magnetization is measured while heating the sample: this is the ZFC part of the curve. FC is achieved by measuring the magnetization under a magnetic field while cooling. The FC curve will diverge from the ZFC one at the blocking temperature T_B . The ZFC *vs.* FC measurements as well as the magnetization as a function of the applied magnetic field (M (H)) curves that we obtained for the different granular samples are displayed in Figure 3.7. For our NMR experiment, it is necessary for the mag-

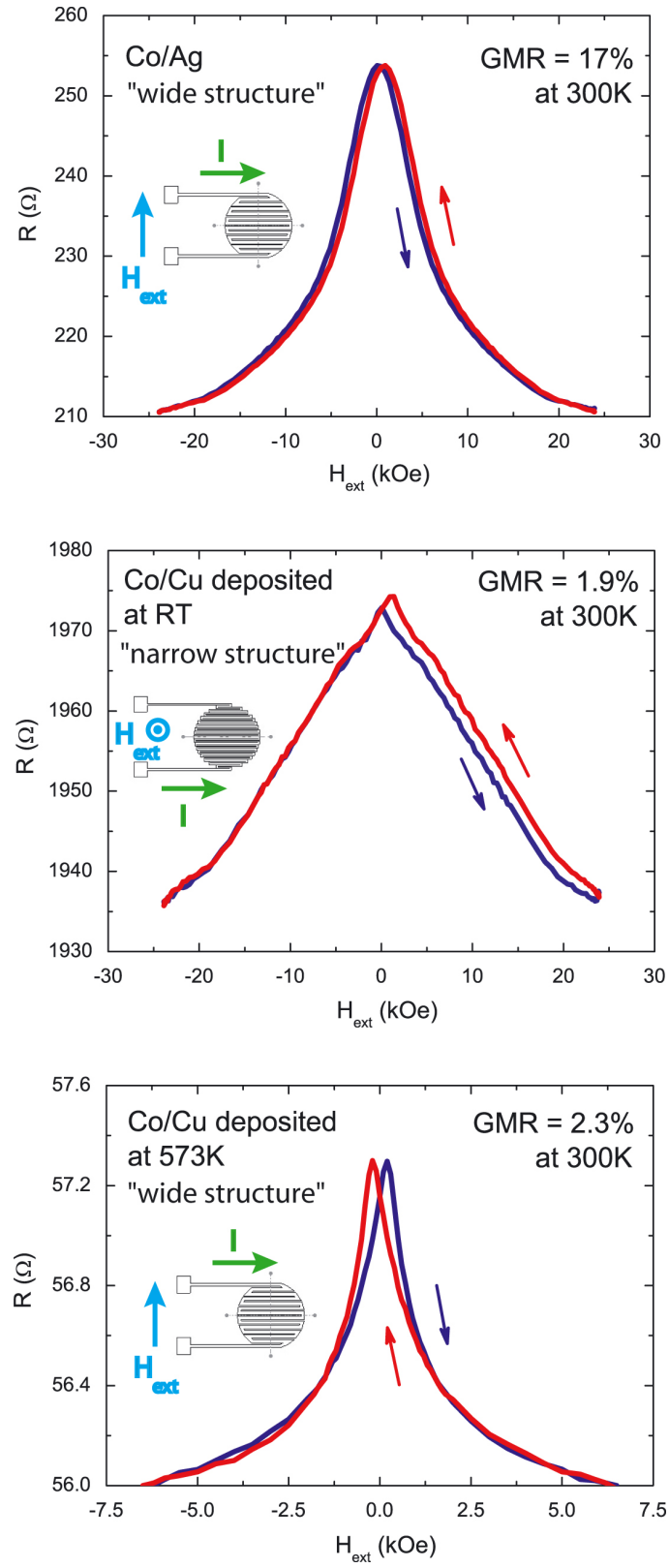


Figure 3.5: GMR of three different granular systems studied: Co/Ag (top), Co/Cu produced at RT (middle) and at 573K (bottom) and sketches of the current and magnetic field orientations used for each measurement.

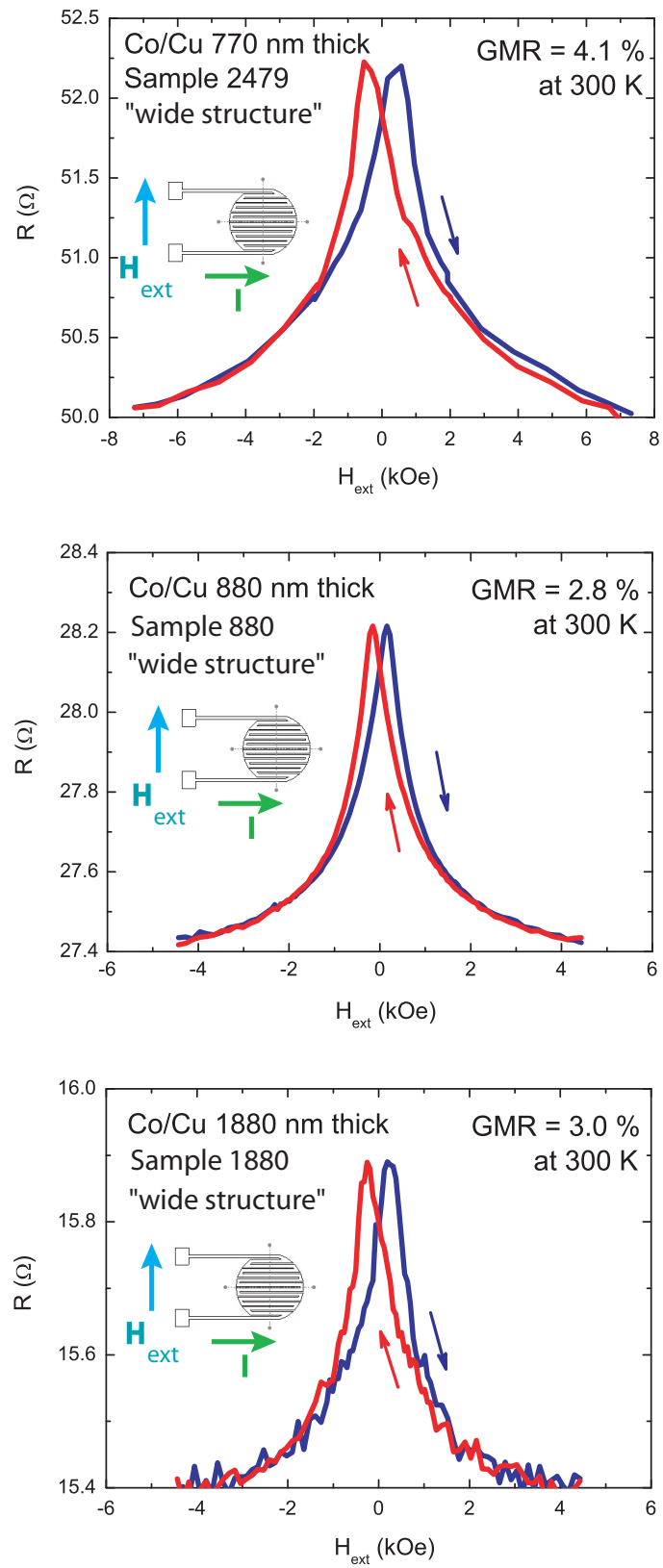


Figure 3.6: GMR of three different Co/Cu granular systems studied: sample 2479 (top), sample 880 (middle) and sample 1880 (bottom) and sketches of the current and magnetic field orientations used for each measurement.

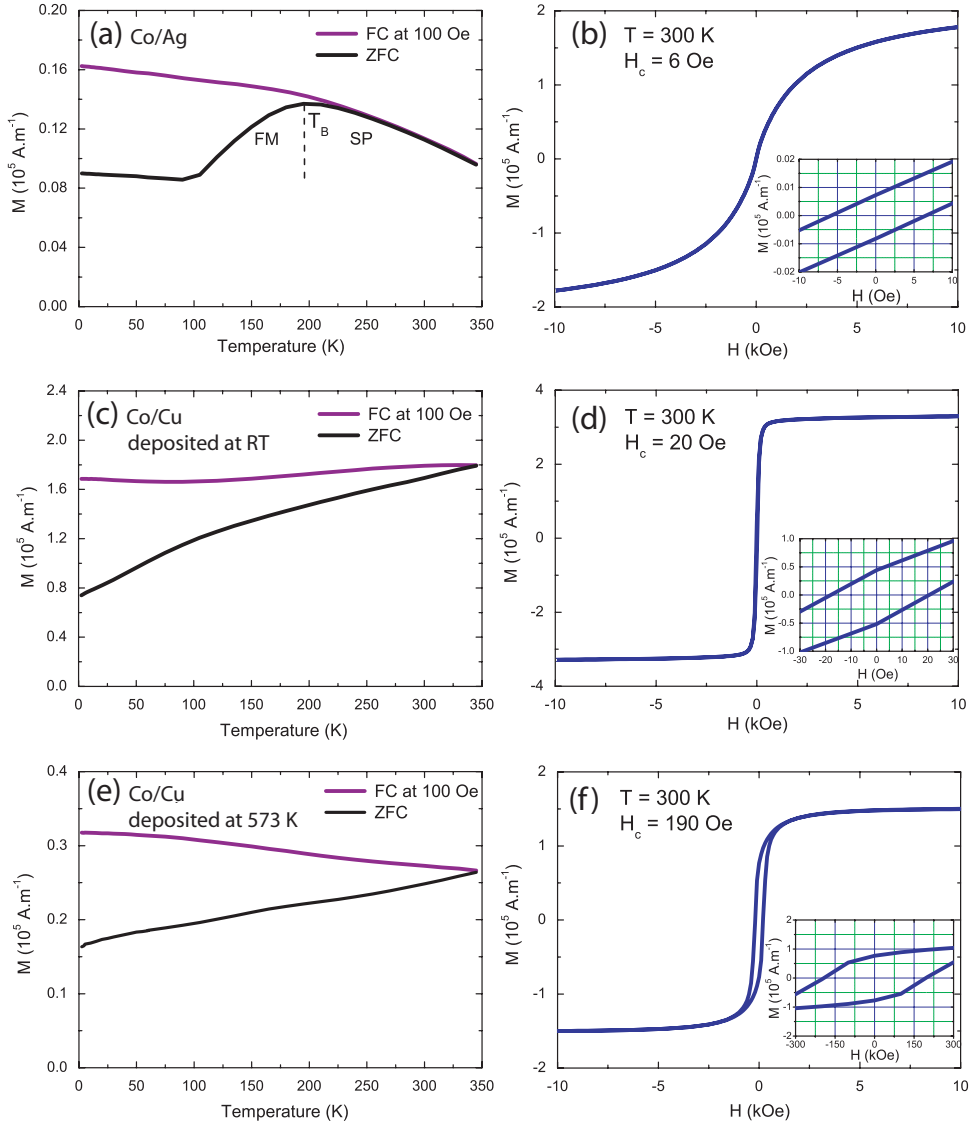


Figure 3.7: Magnetic characterization for the three different granular systems studied: Co/Ag (a) and (b) and Co/Cu produced at RT (c) and (d) and at 573K (e) and (f). The measurements were performed on films deposited on kapton tape, with the field parallel to the film plane.

netization to be blocked at 80 K, as we are working at liquid nitrogen temperatures. The Co/Ag sample (Figure 3.7 (a) and (b)) presented a typical behavior of magnetic nanoparticles with a blocking temperature $T_B \sim 200$ K. The T_B is below RT when the ferromagnetic particles are small. Below T_B is the ferromagnetic state (FM) and above T_B , the superparamagnetic state (SP). The SP at RT is supported by the shape of the $M(H)$ curve. The $M(H)$ curve also reveals a smaller value of the coercive field ($H_C = 7$ Oe) together with a lower magnetization value, compared to the Co/Cu samples.

Concerning the Co/Cu samples (Figure 3.7 (c), (d), (e) and (f)), the magnetic measurements revealed that they were in the ferromagnetic regime in the temperature range investigated, *i.e.* $T_C \gg 300$ K.

We determined the magnetic susceptibilities χ at 80 K from the $M(H)$ curves displayed in Figures 3.8 and 3.9 for the Co/Cu and for the Co films. The values that we obtained are summarized in Table 3.4.

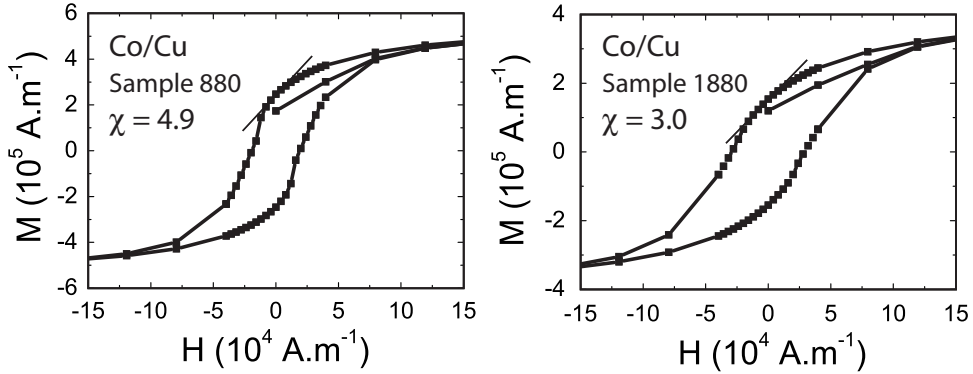


Figure 3.8: Field dependence of magnetization M at $T = 80$ K for the Co/Cu films: sample 880 (left) and sample 1880 (right). The solid lines represent the gradient used to calculate χ . The measurements were performed on films deposited on glass, with the field parallel to the film plane.

Sample	χ
Co/Cu 2442	4.9
Co/Cu 2479	1.7
Co/Cu 880	4.9
Co/Cu 1880	3.0
Co	9.6

Table 3.4: Magnetic Susceptibilities χ determined at 80 K for the different samples of interest.

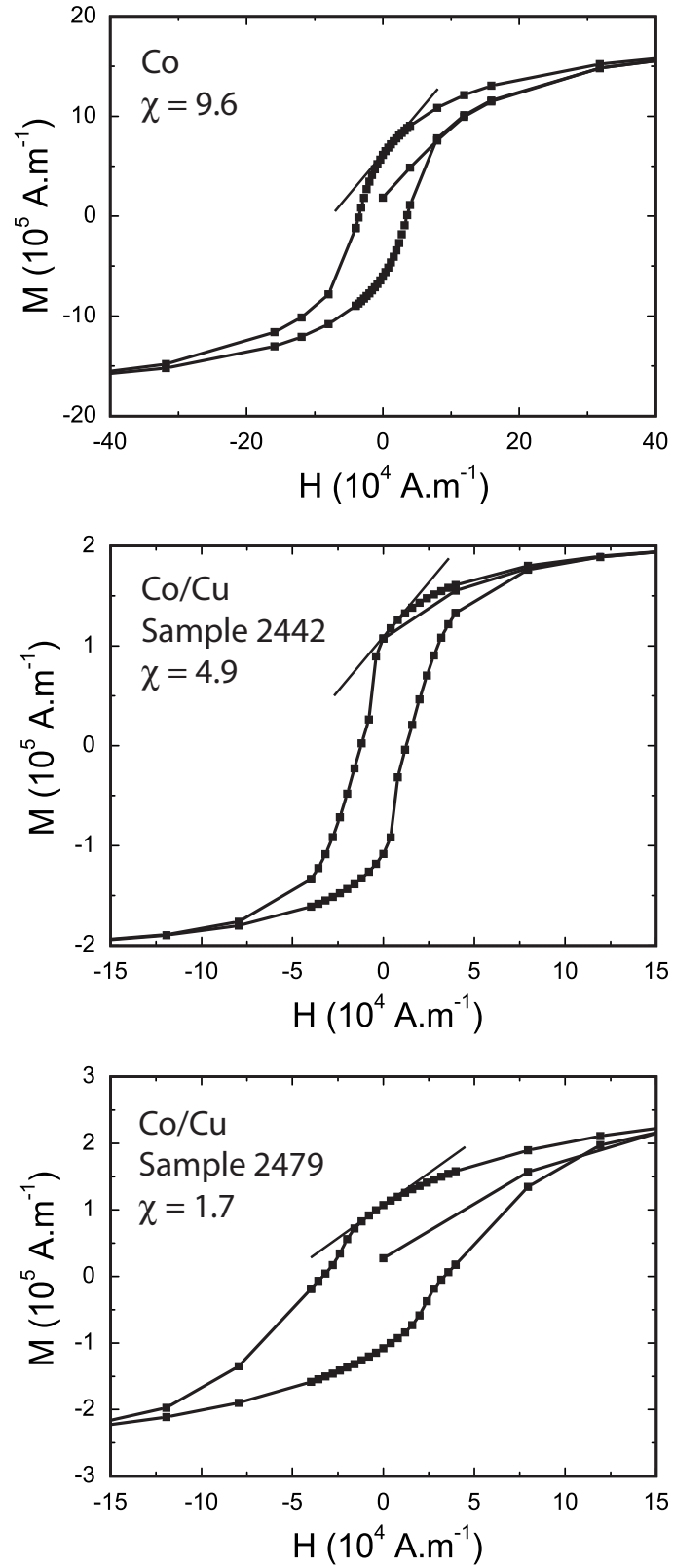


Figure 3.9: Field dependence of magnetization M at $T = 80 \text{ K}$ for the Co sample (top) and the Co/Cu films: sample 2442 (middle) and sample 2479 (bottom). The solid lines represent the gradient used to calculate χ . The measurements were performed on films deposited on glass, with the field parallel to the film plane.

3.3 Co/Ag, Co/Au and Co/Cu multilayered nanowires

3.3.1 Fabrication

To produce metallic multilayered nanowires in a simple, cheap and controlled way, we have used electrodeposition into ion track-etched polymer membranes [28, 29]. Electrodeposition allows us to modulate many parameters in order to optimize the process such as the pH of the electrolyte (acidic conditions in order to prevent oxide formation), the bath concentration, the temperature, and the applied DC current. We carried out the synthesis in a single-bath electrolyte with a three-electrode electrochemical cell, consisting of:

- *a working electrode*: one side of the porous membrane is made conductive by a sputtered layer of Au (or Pt/Ag), typically 300 to 500 nm thick and is isolated from the electrolyte. The working electrode acts as a cathode, where the reduction of the metallic ions occurs:



The filling up of the pores with the desired metal M layers (M = Ag, Au, Cu or Co) is done with a pulse-potential deposition technique by applying the optimized negative potentials for each species, yielded by a cyclic voltammogram of the bath;

- *an inert counter electrode* in Au (or Pt), which plays the role of an anode where oxidation takes place and provides the electrons necessary for the reduction (3.1);
- a saturated Ag/AgCl *reference electrode* filled with KCl, to stabilize the potential difference applied between the working and counter electrodes.

We did all the depositions under potentiostatic control, which means that the potential between the working and reference electrodes is kept at a given value. We monitored the current flow between the counter and working electrodes.

Co/Ag [23] and Co/Au [30] multilayered nanowires were fabricated in 20 μm long polycarbonate membranes by Dr. Sima Valizadeh in Uppsala, Sweden.

We electrodeposited the Co/Cu multilayered samples with an AMEL potentiostat, model 2049. We used 6 μm thick polycarbonate membranes as templates, with pore diameters of about 80 nm and a pore density of 6×10^8 pores/ cm^2 , that we sputtered on one side with Au. The electrodeposition window was a disk of 7 mm in diameter. We used the following electrolyte, containing: 1 M $\text{CoSO}_4 \cdot 7\text{H}_2\text{O}$ (Fluka),

0.025 M $\text{CuSO}_4 \cdot 5\text{H}_2\text{O}$ and 0.728 M H_3BO_3 , at pH 3.2 and we kept it at 35°C during deposition, under continuous stirring. The more reactive metal (here, Cu) will co-deposit with the less noble one (Co) and therefore its concentration in the electrolyte is kept dilute, in order to decrease the impurities in the Co layer. Calibrations of the time needed to fill the pores with each metal individually, evidenced by a rapid increase of the deposition current, provided the optimal deposition rates used for the multilayers.

One of the Co/Cu multilayered nanowire samples that we fabricated, named ARdn4, was used for a preliminary NMR study presented in subsection 4.4.2. For this sample, we deposited each layer of Cu for 0.6 s at $-0.5\text{ V vs. Ag/AgCl}$ and each Co layer for 0.08 s at $-1.0\text{ V vs. Ag/AgCl}$. This sample fulfilled the first two requirements mentioned in section 3.1 and its characterization by means of electron microscopies, magnetic and magnetotransport measurements will be described below.

3.3.2 Characterization by electron microscopy

We performed all the electron microscopy studies at the central facility and Interdisciplinary Center in Electron Microscopy (CIME) of EPFL.

We took scanning electron microscopy (SEM) micrographs using a XL30 FEG microscope in conventional mode. The investigations that we did with SEM showed that the nanowires were cylindrical and proved the high level of inhomogeneity of the growth throughout the membrane.

We used a Philips CM20 transmission electron microscope (TEM), operating at 200 kV in order to evidence the multilayered structure of the electrodeposited nanowires. We found a significant influence of the Co salt used on the electrodepo-

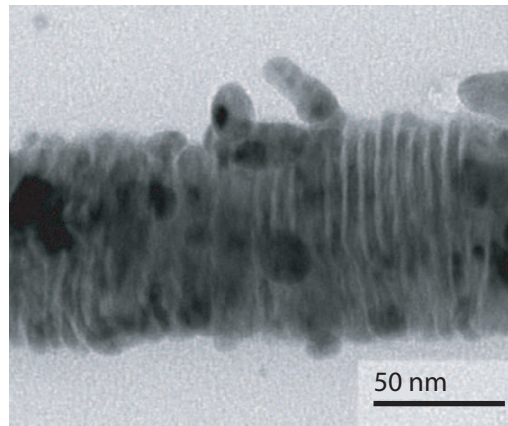


Figure 3.10: TEM micrograph of the Co/Cu sample ARdn4, evidencing the multilayered structure.

sition process. The salt which has always been used in the group ($\text{CoSO}_4 \cdot \text{H}_2\text{O}$) was not available commercially anymore so we had to use $\text{CoSO}_4 \cdot 7\text{H}_2\text{O}$. Transmission electron microscopy, as well as transport measurements, showed that the nanowires grown with Co sulfate heptahydrate salts from one supplier were granular, whereas the same salt from a different supplier gave multilayered nanowires. Figure 3.10 shows a TEM micrograph of ARdn4, evidencing the multilayered structure.

3.3.3 Giant magnetoresistance and magnetic characterization

Figure 3.11 shows a GMR ratio of about 14 %, obtained for the sample ARdn4. We applied the magnetic field in the plane of the layers and did the measurement in the current perpendicular to plane geometry. The blue and red curves represent the field sweep, respectively up and down.

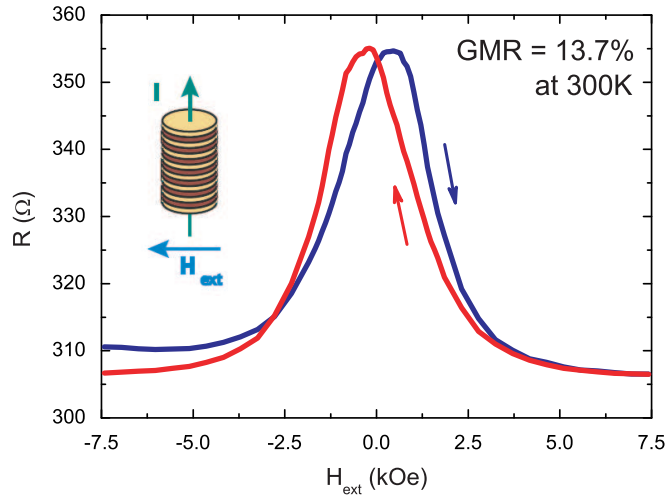


Figure 3.11: Giant magnetoresistance measurement of the Co/Cu multilayered nanowire sample ARdn4 in current perpendicular to plane and magnetic field in plane geometry.

The $M(H)$ curve that we measured at 300 K is given for sample ARdn4 (Figure 3.12). The measurement was performed with the field perpendicular to the axis of the wires. The Co/Cu multilayered nanowires behave as a soft ferromagnet, as the coercive field H_C is small, 220 Oe.

Knowing that the magnetic moment per Co atom in Co metal equals $1.7 \mu_B$, where μ_B is the Bohr magneton [31], we can deduce the number of Co atoms

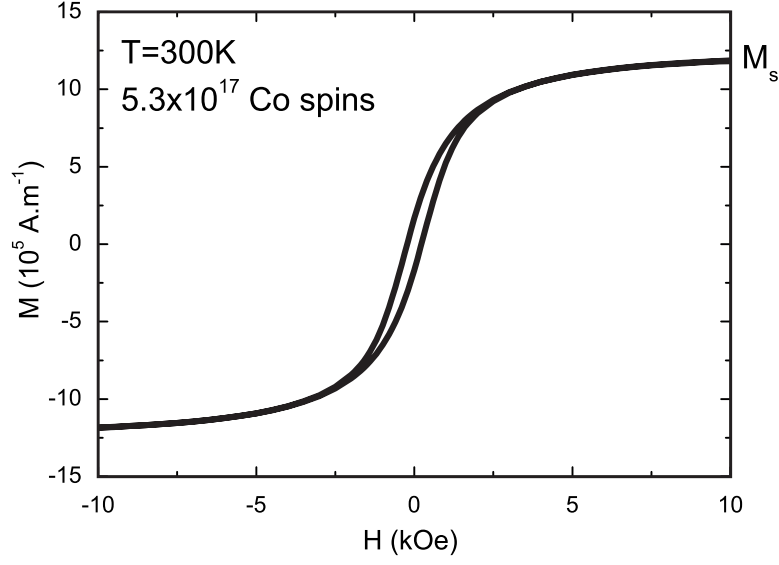


Figure 3.12: Magnetization as a function of the applied magnetic field at $T = 300 \text{ K}$ for the Co/Cu multilayered nanowire sample ARdn4. The measurement was performed with the field perpendicular to the axis of the wires.

contained in the samples from the saturation magnetization M_s , in A.m^{-1} :

$$N_{Co} = \frac{M_s V}{1.7 \mu_B}, \quad (3.2)$$

where $\mu_B = 9.274 \times 10^{-24} \text{ A.m}^2$, and V is the volume of the sample, in m^3 .

If we assume that all the pores were completely filled in the sample ARdn4, the volume of the sample is estimated to be $7 \times 10^{-12} \text{ m}^3$ which leads us to:

$$N_{Co} = \frac{11.9 \times 10^5 \times 7 \times 10^{-12}}{1.7 \times 9.274 \times 10^{-24}} = 5.3 \times 10^{17} \text{ atoms}. \quad (3.3)$$

The saturation magnetization value at room temperature for fcc Co [31] is 20 % larger than the value that we measured. This is compensated by the pore filling, which we overestimated.

In order to satisfy the current density requirement, we had to switch from commercial templates to the lithographed polyimide ones described in subsection 3.1.2, with interconnected sub-micron pores in series.

3.3.4 Longer nanowires interconnected in series

The first step of the work was for us to achieve deposition in non-lithographed polyimide templates, which also implied mastering the electrodeposition in longer pores. Prior to deposition, we immersed the membranes in a 50 % ethanol and 50 % water solution in order to improve the wettability of the pores. We successfully produced Cu, Co and Co/Cu nanowires in 75 μm thick polyimide membranes, with a pore density of 1.3×10^7 pores/ cm^2 and with etched pores of approximately 200 nm in diameter. We deposited the multilayers on a 8 mm diameter disk at 33 °C under continuous stirring of the solution described in subsection 3.3.1 with deposition times of $t_{\text{Cu}} = 4.2$ s and $t_{\text{Co}} = 0.08$ s, and the sample presented up to 14 % of GMR. We used O_2/CF_4 plasma etching (using Tepla equipment in the IPEQ, with a pressure of 0.71 mbar, 10 % CF_4 in O_2 and a power of 300 W) in order to remove the polyimide to image the sub-micron wires by SEM (see Figure 3.13, left) and by STEM.

STEM was achieved using a Philips CM300 microscope, operating at 200/300 kV at the CIME of EPFL in collaboration with Dr. Marco Cantoni. These studies were carried out in order to evidence the multilayered nature of the deposited sub-micron wires. Figure 3.13 (right) shows one such wire, collected from a sample that exhibited 11 % GMR and put on a holey carbon grid. Electron diffraction analysis (inset of Figure 3.13, right) showed that the samples fcc structure is monocrystalline over distances of the order of 1 μm .

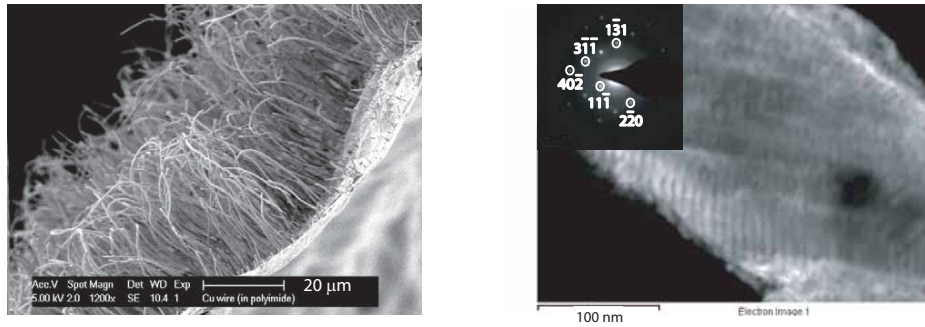


Figure 3.13: SEM micrograph of homogeneous sub-micron Cu wires, revealed by the etching of about 40 μm of the polyimide membrane with the use of an oxygen plasma (left), and STEM darkfield image obtained with the annular dark field detector (ADF) of a Co/Cu multilayered sub-micron wire (right) and electron diffraction pattern of Cu [112] zone axis showing monocrystallinity and the related indexation (inset, right).

The next step was to seek the optimal deposition parameters of Co and Cu in the sub-micron wires of the device described in subsection 3.1.2 and to use them

for the Co/Cu multilayered wires electrodeposition.

It was crucial to improve the wettability of the pores before deposition. For such a purpose, we investigated two different processes:

- soaking of the sample in water with a few drops of Triton X100, in the electrolyte or in a low-acidic solution of SnCl_2 [27] for times up to several hours;
- ultrasonication in a 50 % water and 50 % ethanol bath or in the electrolyte for times up to 20 min.

This step was followed by an immersion of the sample in the electrolyte for 30 min, in order to fill the pores to be deposited. A typical system of four samples mounted for electrodeposition as well as a Cu sample after deposition are showed in Figure 3.14.

A **high filling rate** of the pores across the entire exposed surface is the **mandatory** condition to end the lithographic process by contacting the caps of the nanowires between two adjacent vias and getting good electrical contacts. Unfortunately, we could not achieve this, independent of the wetting process used. Therefore, we abandoned this structure.

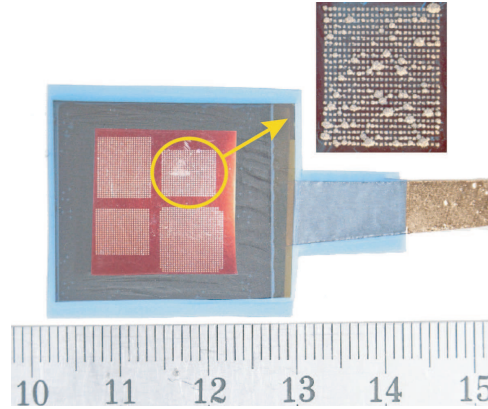


Figure 3.14: Picture of the four samples system, ready for electrodeposition and of the 600 square vias, after Cu electrodeposition, evidencing Cu caps and clearly showing an inhomogeneous growth.

3.4 Co/Cu interconnected pillars in series

The samples were fabricated by Dr. Mohamed Abid, on Si wafers by UV lithography and sputtering in a DC magnetron. The following procedure was used: a 5 nm thick Ti layer was sputtered all over the wafer, followed by a 70 nm thick Au layer. Then a positive photoresist (S1813) was spin coated and the lithographic mask with the bottom contacts (opaque on the mask) was placed over the wafer and submitted

to UV exposure. All the areas of the wafer that were exposed to the UV radiation were removed by reactive ion etching (RIE), under argon, leaving the substrate with the Au bottom contacts. The wafer was then cleaned with acetone, in order to remove the photoresist that was still on the top of the contacts. 5 nm Co/ 5 nm Cu multilayers were sputtered all over the substrate and again, the positive photoresist was spin coated. The second part of the lithographic mask, with $10 \times 10 \mu\text{m}$ opaque squares was carefully aligned on the substrate. RIE was used again, in order to remove the Co and Cu metal between the Co/Cu pillars of interest. An insulator, SiO_2 , was deposited in order to surround the pillars. Then the photoresist that was still over the pillars was removed, with acetone. A Ti/Au layer was sputtered all over the sample and a last photoresist layer was spin coated over it. The third part of the lithographic mask, with the top contacts, was aligned. This was followed by a UV exposure and by RIE in order to remove the Au around the contacts. Acetone was used to remove the leftover photoresist. And finally, a Ta layer was deposited over the sample in order to prevent it from oxidation.

The Figure 3.15 gives an overview of the sample at three different stages: the Au bottom electrodes (left), a tapping mode atomic force microscopy (AFM) image of the Co/Cu multilayered micro-pillars deposited on the bottom electrodes (middle) and a SEM micrograph of the final structure, in which all the 250,000 pillars are contacted in series (right).

The main limitation of this kind of samples was their very high resistance, between 13 and 44 kOhm. Nevertheless, we investigated them by NMR (see subsection 4.4.3), as the geometry remained very convenient for our experiment.

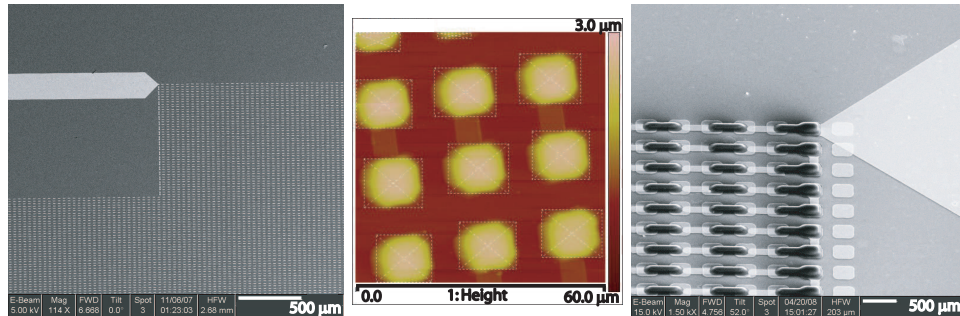


Figure 3.15: SEM micrograph of the bottom electrodes (left); tapping mode AFM image of the Co/Cu pillars deposited on the bottom contacts (middle) and SEM micrograph of the final contacted structure (right). Courtesy of Dr. Mohamed Abid, SFI Trinity laboratory (Ireland).

3.5 Conclusions

In this chapter, we have presented the different samples considered for the search of spin accumulation evidence by NMR.

Two different methods were used for their fabrication: electrodeposition in track-etched membranes and sputtering on lithographed substrates.

We also presented their characterization which was done with different methods, such as: magnetic and magneto-transport measurements, electron and atomic force microscopies.

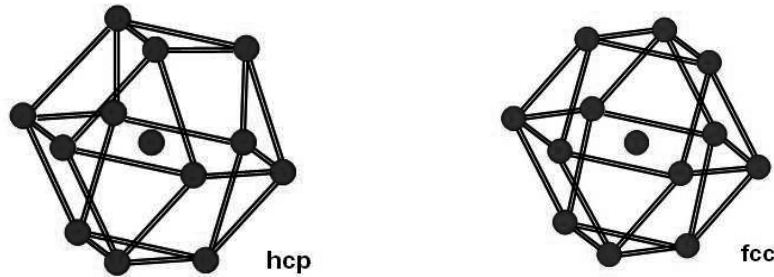
Some of the samples produced could unfortunately not be used for the NMR experiment under current: the structure with Co/Cu multilayered submicron wires connected in series was abandoned due to two main issues encountered during electrodeposition (high level of inhomogeneity and low filling of the pores).

The Co/Cu micro-pillars presented a resistance that was too high. Nevertheless we still investigated their NMR response.

Finally, the granular samples were judged to be good candidates to be measured both in standard NMR and in the NMR under current experiment, as presented in the following chapters of this thesis.

Chapter 4

Microscopic properties of Co nanostructures by NMR



NMR experiments yield both static and dynamic information about the nuclear environment through the analysis of lineshapes and relaxation times [14, 21], respectively. The NMR lineshape provides the distribution of the hyperfine fields in the samples; in particular, it gives local information about the structure (presence of the hcp and fcc phases, for instance) and the interfaces.

The pioneering work on zero-field NMR of a ferromagnetic transition metal was done by Gossard and Portis [18, 19], on ^{59}Co .

Hcp and fcc cobalt pictures adapted from I. Stankovic, M. Kröger, and S. Hess, "recognition and analysis of local structure in polycrystalline configurations," *Computer Physics Communications*, vol. 145, pp. 371-384, 2002.

In the present work, we used zero-field NMR as a main characterization in a study of the spin polarization of conduction electrons in magnetic nanostructures.

This chapter is devoted to studies by NMR of ^{59}Co in the different samples of interest, multilayered and granular, that were previously described. We had the opportunity, at the beginning of this work, to receive multilayered nanowires with different metal spacers. We examined what the NMR looked like in multilayered nanowires of Co/M, with $M = \text{Ag}, \text{Au}, \text{Cu}$. We examined also the Co-NMR of granular samples. We will address as well the spin-lattice (T_1) and the spin-spin (T_2) relaxation times for the main samples that we studied and report the temperature dependance of their lineshapes.

4.1 NMR spectrometer

The zero-field experiments were carried out on a home-made spectrometer that uses a fast digitizer (from Spectrum Systementwicklung Microelectronic GMBH, 8 bit data acquisition, 2 channels, 100 MHz sampling rate per channel usually operating at 50 MHz). The accumulation is done in a HT-Basic program.

We used a pulsed spin echo NMR experiment in this work. We performed the measurements with a so-called “dynamic” continuous flow cryostat, Oxford CF1200, and the temperatures were calibrated with a AuFe/chromel thermocouple.

During this thesis, a probe allowing current injection was fabricated, as illustrated in Figure 4.1. The point in view in designing this probe head was that we planned initially to have samples made of membranes on flat substrates. We wanted then a probe head that optimized the volume of the coil used to produce the rf field. A coaxial line brings the rf to the resonant circuit. Another coax is used to feed the current to the sample.

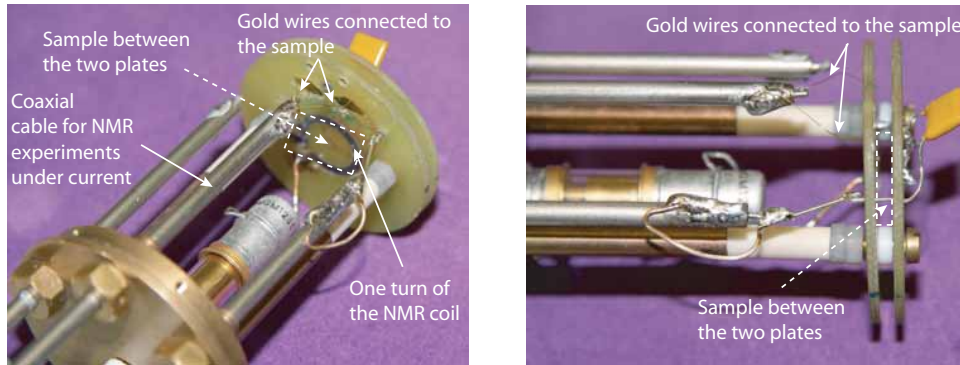


Figure 4.1: Probehead allowing current injection, referred to as the “new” probe.

4.2 Number of observed nuclei

We carried out experiments on the multilayered nanowires sample ARdn4 in order to determine the sensitivity of our NMR spectrometer. We extracted the number of Co atoms contained in the sample by SQUID measurements (see subsection 3.3.3). The signal-to-noise ratio obtained by NMR was satisfactory at 80 K, *i.e.* it corresponded to what can be expected for a sample of the same number of nuclei, set in a resonator of habitual shape. Another study was undertaken with Co powder and we showed that the minimum number of nuclei that we can hope to detect in a reasonable amount of time in order to carry out our various NMR characterizations and investigations under currents, is of the order of 10^{17} Co nuclei.

4.3 Preliminary remarks on ^{59}Co NMR

^{59}Co has a natural abundance of 100 %, a nuclear spin $I = 7/2$ and a gyromagnetic ratio of $\gamma_n = 2\pi \times 10.054$ MHz/T.

We used a spin-echo sequence to observe the NMR signals. This sequence, shown in Figure 4.2, is composed of two square pulses of identical duration t , separated by a variable delay time τ of several microseconds. The optimised pulse length was the one that maximized the spin-echo amplitude. Typically, $t = 0.18 \mu\text{s}$ for all the samples that we will describe below except for the granular one deposited at 573 K, where $t = 0.25 \mu\text{s}$. The estimated range of frequencies covered by such pulses is $\Delta\nu = \frac{1}{2t} = 2.8$ MHz and 2 MHz, respectively. The echo could not be observed after a single scan: every echo was measured by averaging at least 10,000 times (which takes approximately 4 min), going up to 100,000 times for the micro-pillars. This data taking time is determined, not by the repetition rate, but by the ability of the acquisition card, the interface and the computer to accumulate data properly.

We determined the lineshapes by measuring the echo integral at a certain number of discrete values of frequency (point-by-point method), due to the large width of the resonance line (up to 10 MHz).

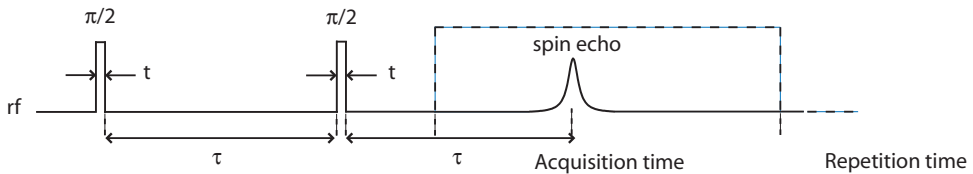


Figure 4.2: RF output for one of the 8 phases of the sequence used and position of the echo in the acquisition window.

As mentioned previously, Co can crystallize in two stable crystallographic structures: hcp, in the case of a ABABAB stacking and fcc for a ABCABC stacking; Co has 12 nearest neighbors in both structures. A difference in the magnitude between the hyperfine fields in the fcc and hcp phases leads to different resonance frequencies for both phases. The positions of the bulk ^{59}Co NMR lines are the following:

- At 80 K, the resonance frequency of the hcp Co phase is 226.7 MHz and for the fcc phase, 216.9 MHz.
- At RT, these values become: 221 MHz (hcp) and 213.1 MHz (fcc).

We underline that at 80 K the signal of 10^{17} Co spins is easily detected due to the amplification factor (see subsection 2.1.3) that increases the Co NMR intensity.

Figure 4.3 sketches the two resonance circuits used for the measurements presented in this chapter. The resonance circuits were made to suit the susceptibility of the samples being measured, independent of the probe used. Unlike the so-called “new” probe (on the right) the “old” probe (on the left) did not allow any current injection.

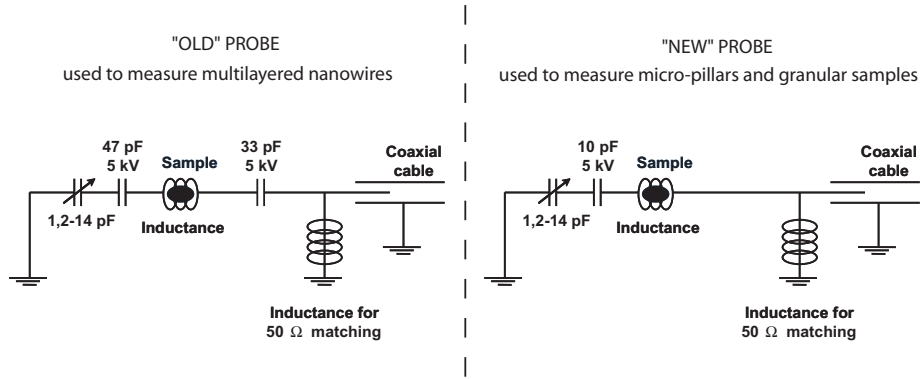


Figure 4.3: Sketches of the resonance circuits used for ^{59}Co zero-field NMR.

The description of the samples studied in the next sections is given in chapter 3. Well-defined and narrow lineshapes are prerequisite conditions for detecting spin accumulation on the NMR.

4.4 ^{59}Co NMR in multilayered samples

In this preliminary study, we investigated the ^{59}Co zero-field NMR lineshapes of different multilayered nanowires.

We found that the structural properties of the cobalt layers strongly depend on 3 parameters: the non-magnetic metal used as a spacer (Ag, Au or Cu); the thickness of the layers and the diameter of the nanowires.

4.4.1 Co/Ag and Co/Au nanowires

Co/Ag multilayered nanowires

The lineshape obtained for the Co/Ag multilayered nanowires is shown in Figure 4.4.

There are two main contributions to this spectrum: one arising from the **bulk** Co, above 210 MHz, called the main line and due to nuclei which are all equivalent and one from the **interfaces**, at lower frequencies. We fitted the experimental points with three Gaussians.

One can clearly distinguish three spectral features in Figure 4.4: besides the prominent line at 223.8 MHz, there is a line at 216.3 MHz and a tail, from 204 MHz down to 160 MHz.

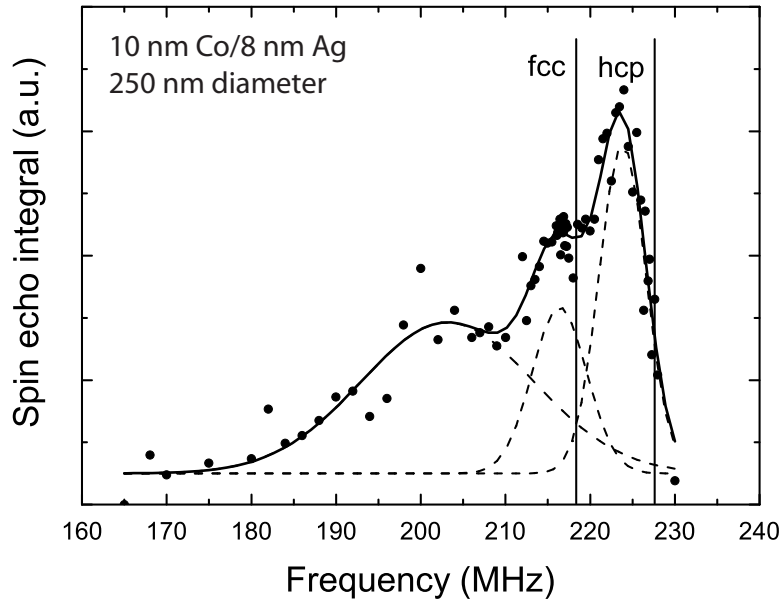


Figure 4.4: Zero-field lineshape of ^{59}Co in a Co/Ag multilayered nanowires sample, at $T = 80$ K; the wires are $20\ \mu\text{m}$ long. The symbols represent the experimental points and the solid line, the fit. The vertical lines represent the positions of the bulk fcc and hcp Co frequencies. The dashed lines represent the Gaussian peaks comprising the fit.

The prominent line, located between the hcp and fcc main resonance frequencies, could be due to intrinsic stacking faults ($\text{ABCA}^\perp\text{CABC}$), according to [32]. The faults could be produced by dislocations that compensate the lattice mismatch η

between Co and Ag, defined by: $\eta = \frac{a_{Co} - a_{Ag}}{\frac{1}{2}(a_{Co} + a_{Ag})}$, where a is the lattice constant; for adjacent layers, $\eta = -14\%$ according to [33]. The line at 216.3 MHz can be attributed to the bulk fcc resonance frequency. Finally, at lower frequencies, the broad line arises from Co atoms having Ag atoms in their nearest neighbor shell. Therefore, the broad decrease observed is a signature of diffuse interfaces. It has been shown in $\text{Co}_x\text{Ag}_{1-x}$ granular films [34] that each Ag atom substituted for Co decreases its resonance frequency by about 12 MHz. The line at 204 MHz would therefore correspond to Co atoms having one Ag neighbor. Co and Ag are immiscible elements, even less miscible than Co and Cu. We would then expect the part of the spectrum corresponding to the interface to be sharp, instead of presenting a long tail. However, the growth process generated by electrodeposition is far from equilibrium, so the notion of immiscibility is of little relevance in this case. For example, Co and Cu are known to be immiscible also, but the Co/Cu multilayered nanowires produced by our group for GMR studies were found to have as much as 15 % Cu in the Co. This is due to the fact that electrodeposition of Co is done at a potential of -1.0 V, whereas -0.1 V would be sufficient to deposit Cu. As a consequence, when applying -1.0 V, all ions get depositions at roughly the same rate. We limit the concentration of non-magnetic metal in the ferromagnet by using electrolytes with a very low concentration of ions of the non-magnetic metal. X-ray diffraction measurements have been achieved on the Co/Ag multilayered nanowires [23] and showed that the Co layers deposited contained 3 weight % of Ag, whereas the Ag layers were 100 % pure. van Alphen *et al.* interpreted sputtered Co/Ag multilayers NMR spectra [35], but for thinner layers than in our case. They also observed a tail in 1.5 nm Co/2 nm Ag multilayers, which has been interpreted from the first stages (2 Co monolayers) of the growth. Thus, in order to explain the high intensity of the interfacial spectrum that we observed (meaning that Co atoms are in imperfect surroundings), we can make the assumption that the Co in the wires presumably started to grow the same way as for [35], *i.e.* in many three-dimensional islands, that merged to form a continuous layer. This is in accordance with the facts that there are weak interactions between Co and Ag and that the surface energy of Co is much larger than the surface energy of Ag.

Diffuse interfaces are known to give poor GMR performance, and correlatively of low spin accumulation. We decided not pursue work with Ag spacers for this reason. Spin accumulation, when it arises, spreads over a distance from the interface of the order of the spin diffusion length. It is not limited to an atomic scale. It seemed that it made more sense to stay with systems that present the sharpest interfaces and the most GMR. It has been shown [35] for sputtered Co/Ag multilayers with

thin Co layers that an annealing treatment would sharpen the interfaces (“back-diffusion” of Co and Ag). We did not investigate this for our samples, as we would not be able to get to the current density needed for our NMR experiment under current with nanowires. This is because we were not able to contact the bundles of nanowires in the vias, as the filling rate was not high enough (see chapter 3).

Co/Au multilayered nanowires

We studied three Co/Au multilayered nanowires samples by NMR, with different Co and Au thicknesses and different pore diameters. The spin-orbit interaction plays an important role in Au, which would make the spin diffusion length much too short, imposing spacer thicknesses that are not controllable by our growth process. We have good control of layer thickness down to about 10 nm, not much less. In experimental measurements on *lateral* spin valve devices, large values of the spin diffusion length have been reported, from 63 nm at 10 K [36] to 168 nm at 15 K [37], however there is no consensus in these results. Therefore, Au would not be considered the ideal spacer layer for detection of spin accumulation by NMR. But in the interest of fully exploring the candidate spacer layers available, we did a NMR characterization which is presented in Figure 4.5.

All the envelopes present a full width at half maximum (FWHM) of around 10 MHz. For each sample, we fitted the experimental data with three Gaussians:

- **12 nm Co/4 nm Au** (Figure 4.5, top): the spectrum observed signals the presence of many stacking faults, certainly due to the small pore diameter (100 nm). Bubendorff *et al.* [38] showed a similar spectrum for 2 nm thick Co films electrodeposited on Au (111) using a solution with pH 4 and deposited under an overpotential of 0.18 V. They attributed the prominent line at 225 MHz either to a small lattice expansion of Co due to the large mismatch (14 %) between hcp Co and fcc Au or to defects in the hcp stacking. We also observe a contribution of the nuclei in the fcc phase, at 216.9 MHz. And at lower frequency, around 208 MHz, we clearly see the line corresponding to Co atoms with one Au neighbor, which is probably shifted due to faults.
- **10 nm Co/6 nm Au and 10 nm Co/4 nm Au** (Figure 4.5, middle and bottom): the pore diameter is 250 nm and we only observe lines at frequencies corresponding to the fcc structure, both in bulk and in stacking faults [32]. The signal arising from the bulk fcc phase dominates the one coming from the fcc stacking faults observed at 221.7 MHz for the Co/6 nm thick Au nanowires and at 222.5 MHz for the Co/4 nm Au nanowires. The samples

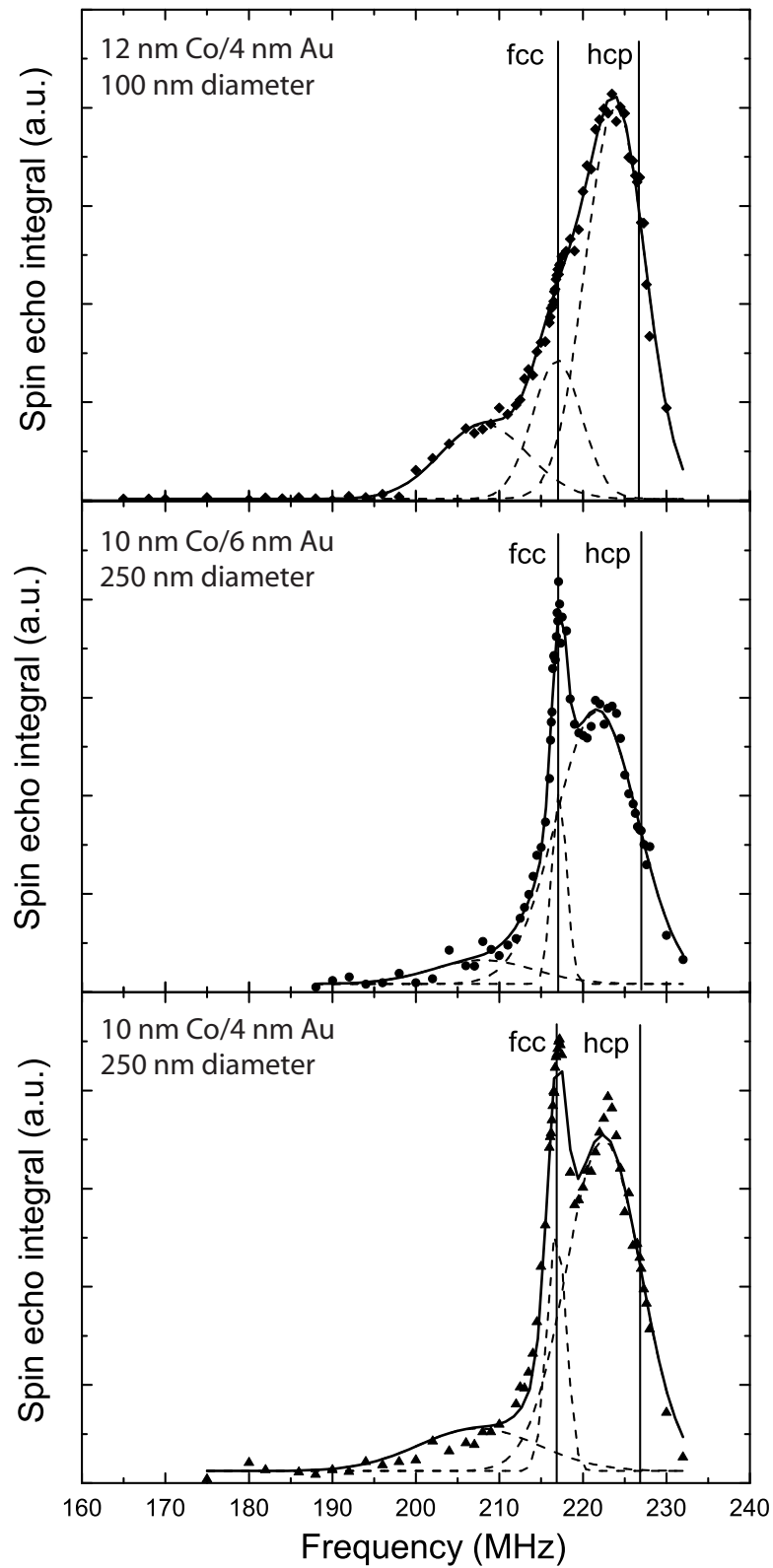


Figure 4.5: Zero-field lineshapes of ^{59}Co in different Co/Au multilayered nanowires, at $T = 80\text{ K}$; the wires are $20\text{ }\mu\text{m}$ long. The symbols represent the experimental points and the solid lines, the fit. The vertical lines represent the positions of the bulk fcc and hcp Co frequencies. The dashed lines represent the Gaussian peaks comprising the fit.

also show a small contribution at 208 MHz, due to Co atoms with one Au neighbor, probably shifted due to faults.

The stacking faults are omnipresent in each spectrum, probably due to the mismatch between the two elements. The relatively small pore diameter (100 nm) features mainly hcp stacking faults, whereas 250 nm diameter pores feature the fcc phase, either in bulk or with stacking faults.

In contrast to the Co/Ag multilayered nanowires, we found well-defined line-shapes for Co/Au multilayers. But out of concern regarding the strong spin-orbit interaction, Au was not further considered for our experiments.

4.4.2 Co/Cu nanowires

We present the NMR signals that we obtained on the sample ARdn4 in Figure 4.6. This sample has also been investigated by magnetic and magneto-transport measurements (see subsection 3.3.3).

We fitted the spectra with three Gaussians. As expected, only the fcc phase is present for our 5 nm Co/5 nm Cu sample.

The main line frequency is slightly lower (214.4 MHz) than that of bulk fcc Co, which can be attributed to strains resulting from the difference in the lattice constants between Co and Cu. In [39] thin films of Co/Cu multilayers were grown over oxidized silicon substrates by e-beam evaporation and the stress was studied by NMR. Indeed, changes in volume induce variations of the value of the hyperfine field: $\Delta B_{hf}/B_{hf} = -1.16\Delta V/V$; that is, a shift of the center of the peak of $\Delta f = \gamma\Delta B_{hf}$. The authors found 0.4 % of mismatch per MHz. Hence the shift of Figure 4.6 with respect to tabulated fcc corresponds to a mismatch of 1 %. Prof. Valerio Scarani had considered more closely the state of strain of electrodeposited nanowires, as a function of temperature. He concluded that the deposits appeared as if they were stretched out, or in other words, as if the atoms did not have enough time to find their equilibrium position before being blocked by further atoms being deposited. The line at 204 MHz corresponds to Co atoms having one Cu atom in their nearest neighbor shell and the line at 190 MHz shows the Co atoms with two Cu nearest neighbors.

The limitation induced by the requirements on sample shape (see section 3.1) contributed to our choice of **discarding** the Co/Cu multilayered **nanowires** for our experiment.

Nevertheless, **Cu was kept as a spacer**, for two main reasons: Co and Cu are two commonly sputtered elements (we remind the reader that sputtering is the technique used for micro-pillars and granular samples, that we will describe below)

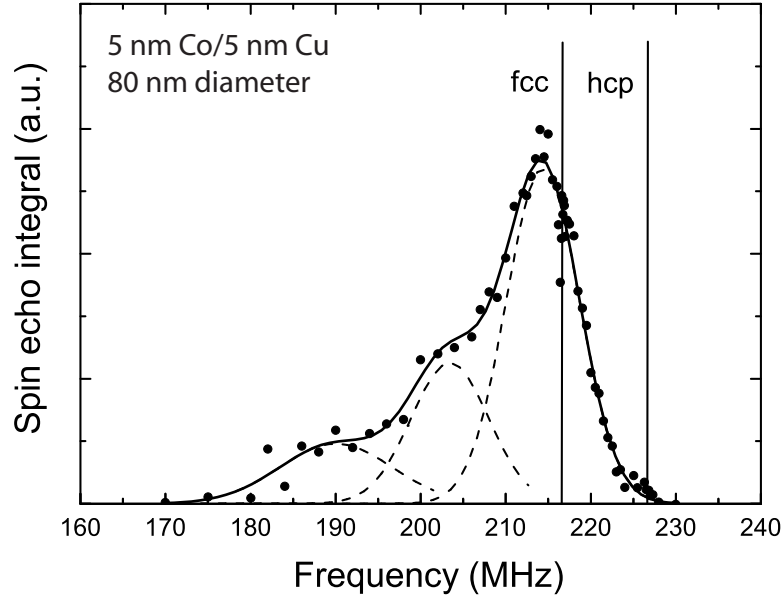


Figure 4.6: Zero-field lineshape of ^{59}Co in the Co/Cu multilayered nanowires (sample ARdn4), at $T = 80\text{ K}$; the wires are $6\text{ }\mu\text{m}$ long. The symbols represent the experimental points and the solid line, the fit. The vertical lines represent the positions of the bulk fcc and hcp Co frequencies. The dashed lines represent the Gaussian peaks comprising the fit.

and above all, Co/Cu samples present a high magnetoresistance.

4.4.3 Co/Cu micro-pillars

We investigated by NMR the $5\text{ nm Co}/5\text{ nm Cu}$ micro-pillars described in the previous chapter, after the whole lithographic process, before making the top connections. Even if the thicknesses of the Co and Cu layers were the same as for sample ARdn4, the different fabrication method used (sputtering instead of electrodeposition) results in a different lineshape (Figure 4.7). This dependence on the mode of fabrication has also been observed by Panissod [40] for several other fabrication techniques (molecular beam epitaxy, diode sputtering, *etc.*). The ^{59}Co signal was very low and therefore we had to accumulate 10 times longer than usual.

We fitted the experimental points with two Gaussians. As already described, the spectrum is typical of a fcc structure shifted from the bulk frequency due to strains (line at 214.6 MHz) and to nuclei in stacking faults (at 221.6 MHz).

This sample was not retained for the NMR experiment under current because of three main limitations: the low Co signal obtained (due to the low Co concentration in the sample), the shape of the NMR line observed and the very high resistance that this sample would have if we completed the contacting on top of the pillars. We would expect a resistance of tens of kOhms if we did. It would then not be

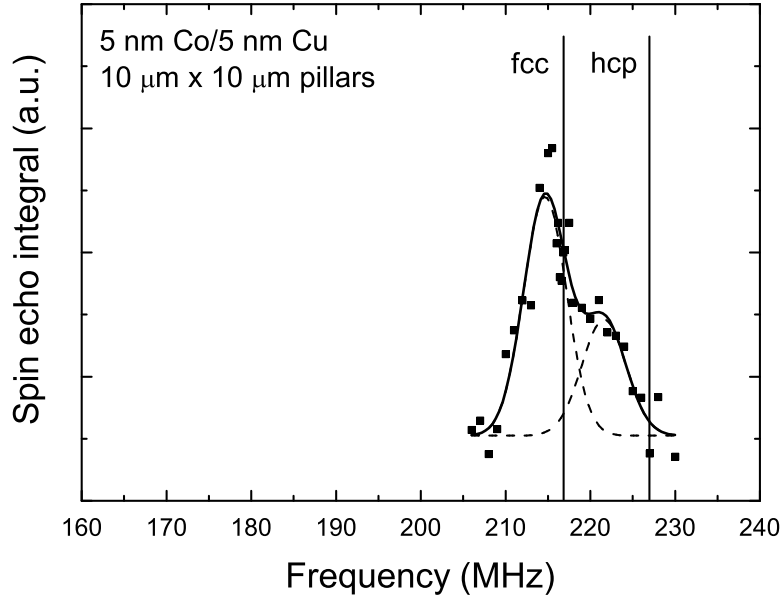


Figure 4.7: Zero-field lineshape of ^{59}Co in the Co/Cu multilayered micro-pillars, at $T = 80$ K. The symbols represent the experimental points and the solid line, the fit. The vertical lines represent the positions of the bulk fcc and hcp Co frequencies. The dashed lines represent the Gaussian peaks comprising the fit.

feasible to drive a large current density in this sample.

4.5 ^{59}Co NMR in Co/Cu granular samples

We could not detect any NMR signal on the Co/Ag granular samples, even at 10 K, *i.e.* below the blocking temperature (see Figure 3.7 (a) in subsection 3.2.2). The annealing of the sample at 400°C for one hour did not lead to a better result. The absence of NMR signal for these samples is currently not understood.

Nevertheless, we obtained very encouraging results on the Co/Cu granular samples, sputtered both at RT and at 573 K. We will present the lineshapes observed as well as the spin-spin and spin-lattice relaxation times that we measured. The effect of the temperature will also be addressed.

4.5.1 Co/Cu fabricated at RT

We studied a Co/Cu granular sample - referred to as sample 2 in the previous chapter - fabricated at RT and presenting 2 % GMR.

As illustrated in Figure 4.8, the NMR spectrum revealed a very narrow and well-defined line. Only the fcc phase was present with an FWHM of 0.7 MHz which was very promising for our purposes.

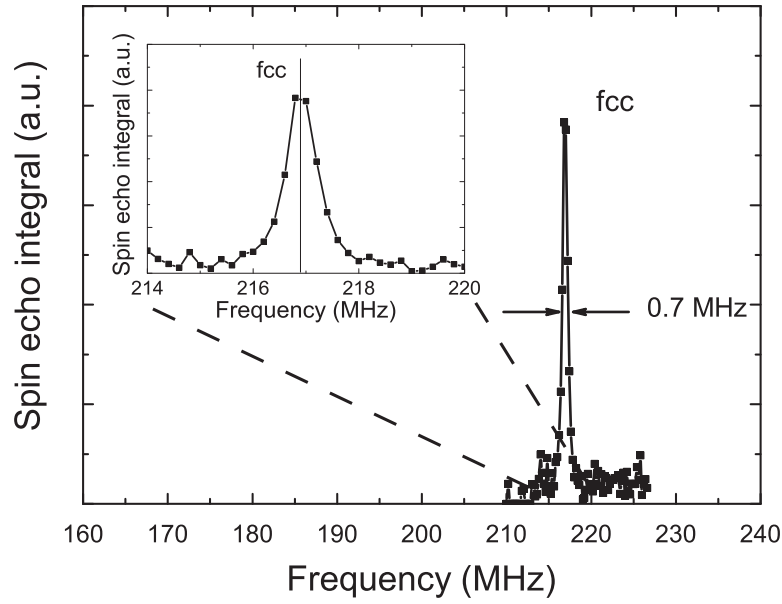


Figure 4.8: Zero-field lineshape recorded for ^{59}Co in the Co/Cu granular sample deposited at RT, measured at $T = 80$ K. The inset shows a zoom of the spectrum, for more clarity.

We also analyzed the temperature dependance of the ^{59}Co lineshape. In Figure 4.9 (top), we present the lineshape of ^{59}Co at several temperatures between 80 K and 300 K. We observed that the intensity of the line was greatly reduced with increasing temperature. We believe that this effect does not depend on T_2 , but that it is due to the Boltzmann factor $\hbar\omega/k_B T$ and to the frequency dependent factor coming from the e.m.f induced in the coil by the magnetization. This is illustrated in the inset of Figure 4.9 (top), where we present the lines corrected for both factors. The intensities of the lines obtained are constant over the temperature range considered. The width of the line does not seem to change between 80 K and 300 K.

In the temperature range of interest, the hyperfine field of Co in this sample presents a linear dependance *vs.* $T^{3/2}$ (Figure 4.9 (bottom)), as expected from the temperature dependence of the magnetization due to spin waves. This is in good agreement with previous studies on ^{57}Fe [41] and on fcc ^{59}Co [42] and hcp ^{59}Co [43]. The data that we obtained in the temperature range studied are in very good agreement with the data of Jaccarino [42], which is illustrated in Figure 4.9 (bottom).

Figure 4.10 illustrates the curve obtained for the T_2 measurement of this granular sample, at 80 K. We fitted the experimental points with a single exponential.

We used a saturation recovery sequence for the determination of T_1 , instead of an inversion recovery sequence. This was motivated by the fact that in ferromag-

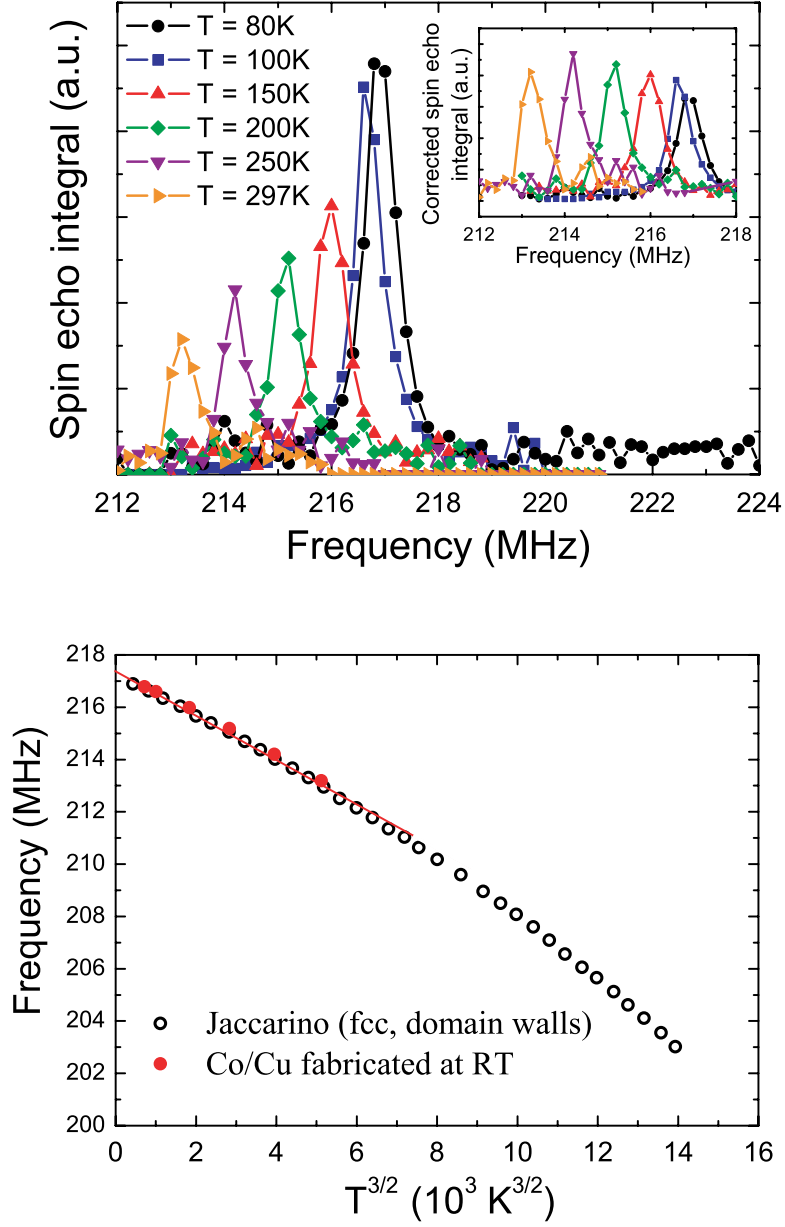


Figure 4.9: Zero-field lineshapes recorded for ^{59}Co in the Co/Cu granular sample deposited at RT, for several different temperatures (top). The inset shows the lineshapes corrected for the Boltzmann factor and for the frequency dependent factor. NMR frequency of ^{59}Co vs. $T^{3/2}$ obtained for our sample, compared to the results of Jaccarino (bottom).

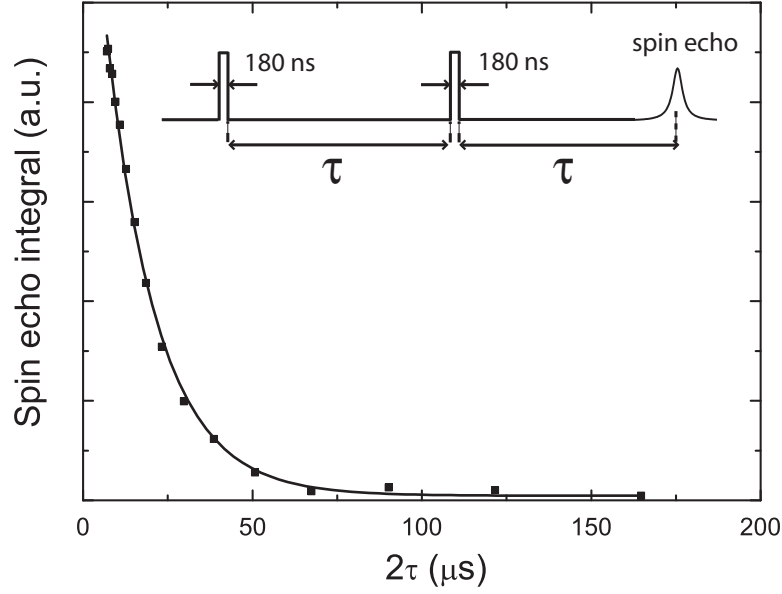


Figure 4.10: Spin-echo integral as a function of 2τ values in the Co/Cu granular sample fabricated at RT, measured at 80 K; the symbols represent the experimental points and the solid line, the fit. The inset shows the pulse sequence used for T_2 measurement; we used $\tau = 5 \mu\text{s}$.

netic metals, the $\pi/2$ and the π pulses are not well-defined. In the inset of Figure 4.11 (top), we present the sequence we used to measure T_1 in the Co/Cu granular sample deposited at RT. First, we destroyed the magnetization by a saturation sequence of pulses. Various pulse sequences can be used for such a purpose. Our destruction consisted of four long pulses, whose length is similar to the measured T_2 (10-20 μs). The application of these pulses in 4 different directions (x, -x, y, -y) in the plane perpendicular to the effective field gave a satisfactory destruction of the signal. Then, we waited a certain recovery time, called recovtime before measuring the signal with a spin echo sequence. We found a typical magnetization recovery curve by plotting the echo integral *vs.* the recovery time on a logarithmic scale as illustrated on Figure 4.11 (top). We obtained the spin-lattice T_1 relaxation times by fitting the magnetization recovery curves by single exponentials. T_1 and T_2 obtained for different temperatures are summarized in Table 4.1.

T (K)	T_1 (μs)	T_2 (μs)
80	341	15.6
150	255	14.5
300	163	12.7

Table 4.1: T_1 and T_2 relaxation times as a function of the temperature T for the Co/Cu granular sample fabricated at RT. T_1 and T_2 were measured at the maximum of the NMR line.

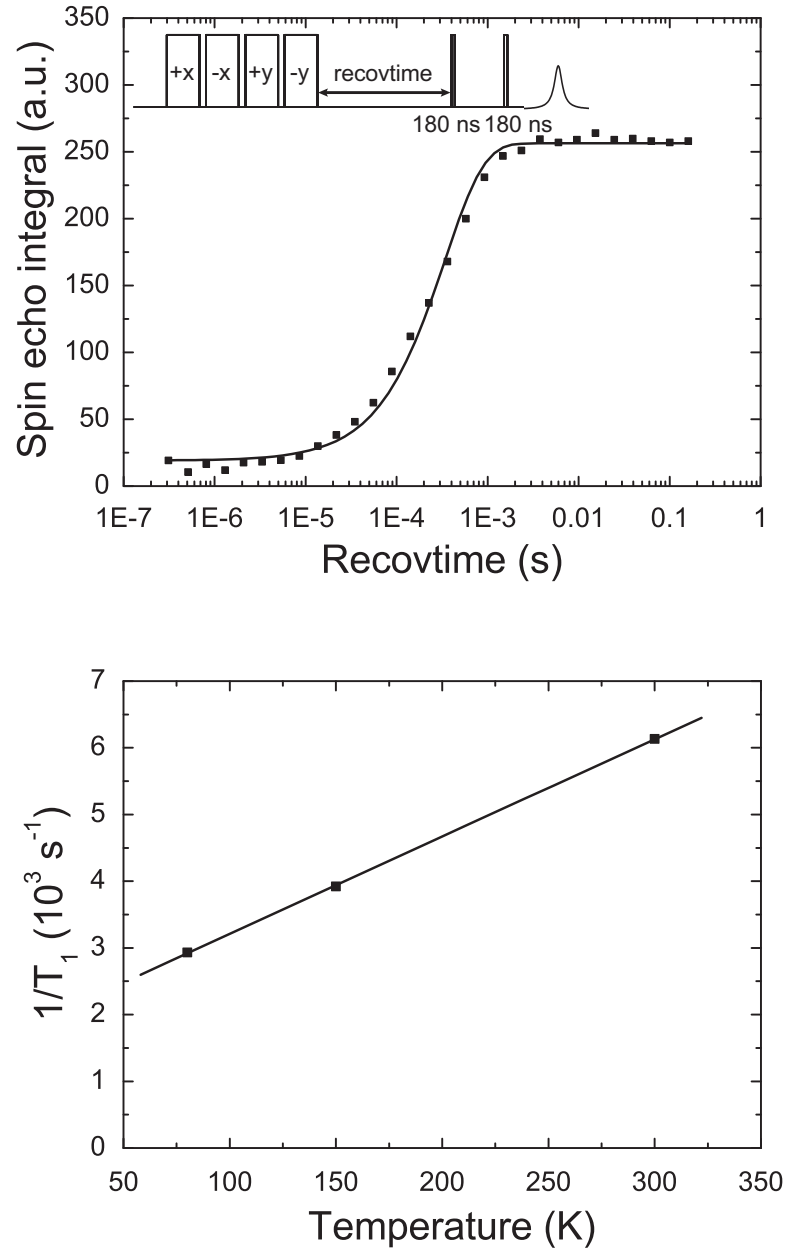


Figure 4.11: Spin-echo integral as a function of recovery time values in the Co/Cu granular sample fabricated at RT, measured at 80 K; the inset shows the pulse sequence used for T_1 measurement; we used $\tau = 5 \mu\text{s}$ (top). Evolution of $1/T_1$ as a function of the temperature for zero external field (bottom). The symbols represent the experimental points and the solid line, the fit.

$1/T_1$ is proportional to the temperature over the whole investigated temperature range and under zero external magnetic field in the Co/Cu granular sample fabricated at RT, as illustrated in Figure 4.11 (bottom).

There are various possible contributions to the nuclear spin relaxation rates. The work achieved on both theoretical and experimental understanding of the spin-lattice relaxation times in Co was quite controversial, as presented in [44]. The signal can arise either from spins in a domain wall or in a domain, according to Weger [45], who attributes an exponential relaxation and linear temperature dependence of $1/T_1$ to nuclei in domains. The temperature dependence of the nuclear spin relaxation rates $1/T_1$ in our sample is well described by: $\frac{1}{T_1} = CT + D$ with $C = 14.6 \text{ (sK)}^{-1}$ and $D = 1753 \text{ s}^{-1}$. The slope was close to the value of 13 (sK)^{-1} obtained by Weger [45] and Jaccarino [46].

Unfortunately, we had an issue with oxidation of this sample, and due to the loss of NMR signal, we did not drive any current into it. In order to reduce the oxidation to the minimum, an additional Si_3N_4 capping layer was deposited on top of all the following samples.

To improve the quality of the following samples, their fabrication was done at higher temperatures (573 K) and the shaping of the samples in the form of meanders was done after a uniform deposition, by reactive etching. As reported below, we never again obtained spectra with such a narrow resonance. It is not clear why this sample had such a narrow resonance. It may be that it had large grains of fcc structure only.

4.5.2 Co/Cu fabricated at 573K

The Co/Cu granular sample fabricated at 573 K that we will describe below was protected against oxidation with a Si_3N_4 layer. The lineshape that we observed (Figure 4.12) presented a larger FWHM (6.4 MHz) than the granular sample deposited at RT. Nevertheless, only the fcc phase was present.

A study of the lineshapes for different temperatures was also carried out, as shown in Figure 4.13 (a). The loss of signal with temperature was even more obvious than for the sample deposited at RT. We corrected the spectra for the Boltzmann and the frequency dependent factors coming from the e.m.f induced in the coil by the magnetization (see Figure 4.13 (b)). Nevertheless, there remained a loss of intensity that we attributed to the decrease of T_2 when increasing temperature for this sample. This was compatible with our T_2 data (Table 4.2). Assuming that T_2 is frequency independent, we observed no effect of temperature anymore on the integral of the corrected NMR line when we added the correction for T_2 effects

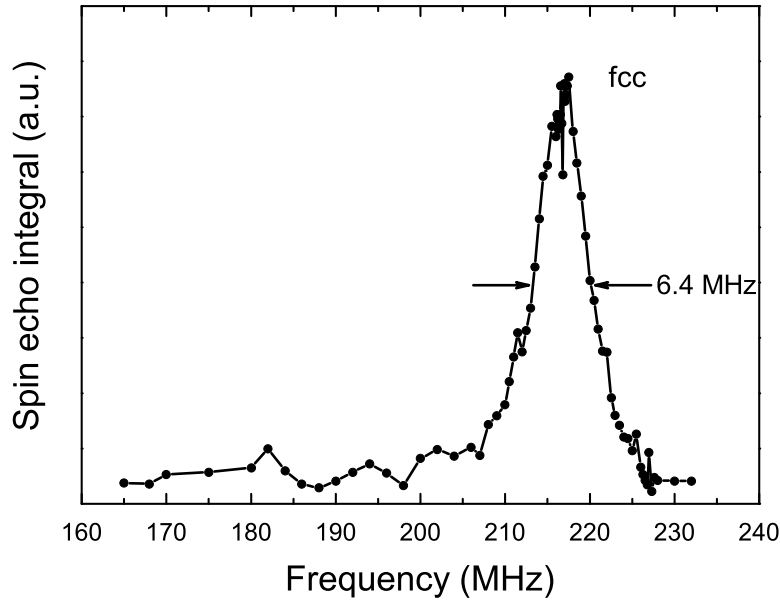


Figure 4.12: Zero-field lineshape recorded for ^{59}Co in the Co/Cu granular sample deposited at 573 K, measured at $T = 80$ K.

(Figure 4.13 (c)). We also obtained a linear dependence of the ^{59}Co NMR frequency *vs.* $T^{3/2}$, in agreement with [41, 42, 43], illustrated in Figure 4.13 (d).

T_1 was measured as described previously with the saturation recovery sequence sketched in Figure 4.14 (top). In order to visualize the effect of such a sequence, we Fourier-transformed the echo obtained at the resonance frequency for several recovery times. The results are presented in Figure 4.14 (middle). For a very small recovery time value, we observed a hole in the spectral line, produced by the destruction of the magnetization. Magnetization recovery took place by varying the recovery time.

T_1 values are summarized in Table 4.2, together with T_2 values.

The temperature dependence of the nuclear spin relaxation rates $1/T_1$ obtained under zero external magnetic field in the Co/Cu granular sample fabricated at 573 K is linear, as illustrated in Figure 4.14 (bottom). $1/T_1$ is well described by: $\frac{1}{T_1} = CT + D$ with $C = 42.4 \text{ (sK)}^{-1}$ and $D = 2097 \text{ s}^{-1}$. These values are somewhat higher than the ones obtained for the sample deposited at RT. The origin of this increase is currently not understood.

This sample was studied under current, as we will describe in the following chapter.

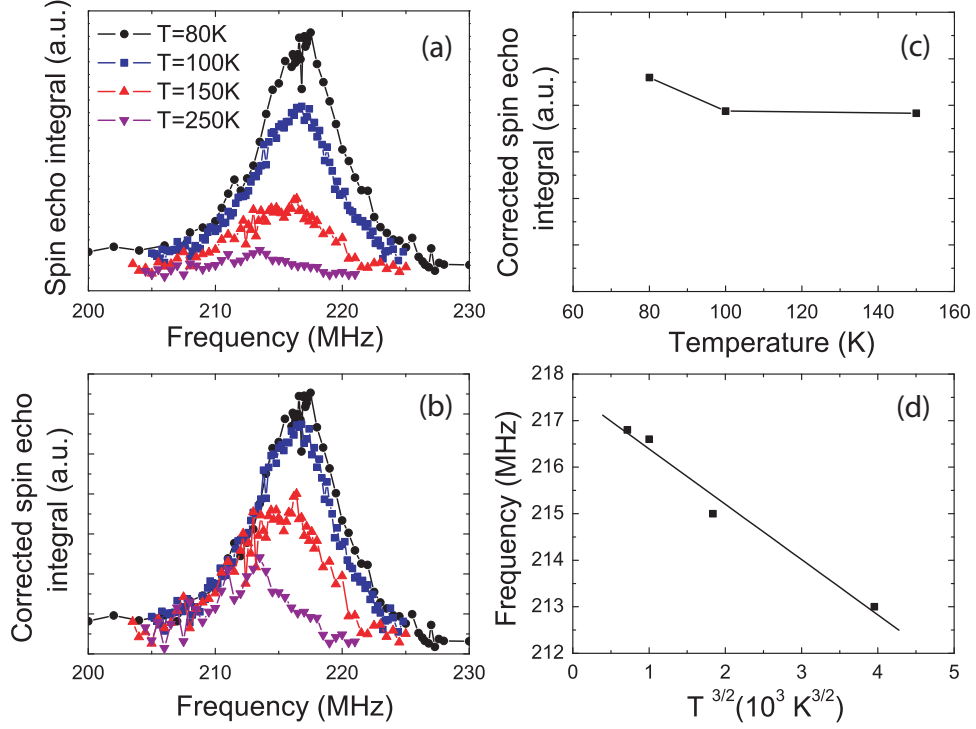


Figure 4.13: (a) Zero-field lineshapes recorded for ^{59}Co in the Co/Cu granular sample deposited at 573 K, for several different temperatures; (b) Lineshapes corrected for the Boltzmann factor and for the frequency dependent factor; (c) Lineshapes corrected for the Boltzmann factor, for the frequency dependent factor and for T_2 ; (d) NMR frequency of ^{59}Co vs. $T^{3/2}$ obtained for our sample.

T (K)	T_1 (μs)	T_2 (μs)
80	175	15.7
100	123	14.8
150	67	10.4

Table 4.2: T_1 and T_2 relaxation times as a function of the temperature T for the Co/Cu granular sample fabricated at 573 K. T_1 and T_2 were measured at the maximum of the NMR line.

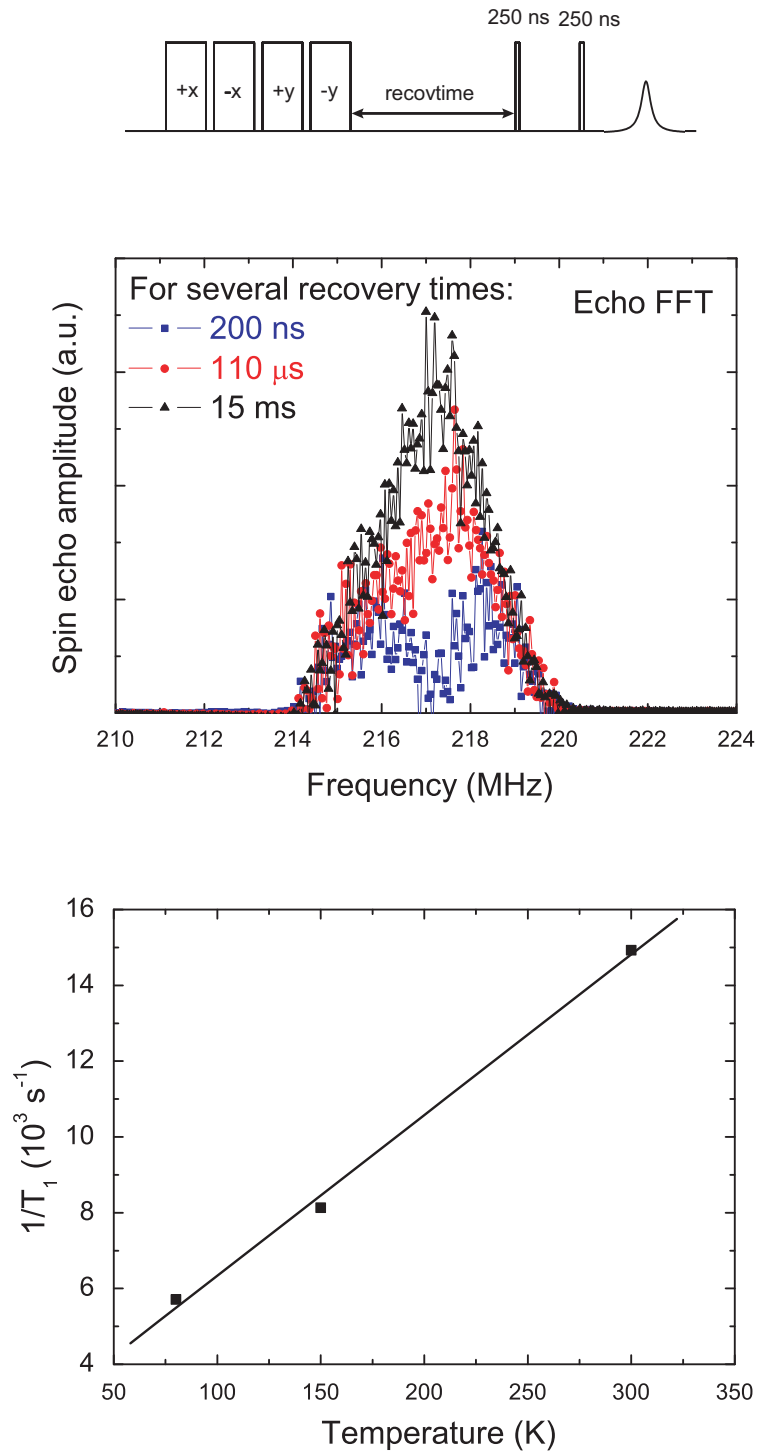


Figure 4.14: Pulse sequence used for T_1 measurement for the Co/Cu granular sample fabricated at 573 K (top). Illustration of the magnetization recovery at 80 K for different recovery times using the saturation sequence (middle). Evolution of $1/T_1$ as a function of the temperature for zero external field; the symbols represent the experimental points and the solid line, the fit (bottom).

4.6 Conclusions

In this chapter, we have addressed a ^{59}Co NMR study, encompassing the lineshapes obtained for different magnetoresistive samples, T_1 and T_2 as well as the temperature dependence of the lineshapes and relaxation times.

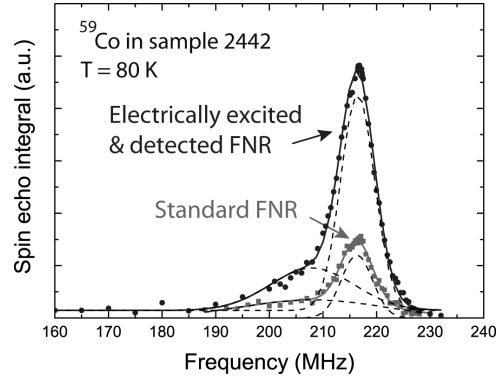
We were interested to have a fcc phase only, as well as a narrow and well-defined NMR line. We found that Cu was a good candidate for our purposes. We turned to granular films, as they were in the end the only feasible method of insuring a sufficient sample size and yet a small enough cross section that we could reach the current densities that we aimed for. This was supported by a fairly good magnetoresistance found in these samples. However, this choice meant that we lost the assurance that the current would be entirely driven through the Co/Cu interface. It was a compromise we had to make in order to move on to exploring the effect of a current on the NMR, rather than taking the risk of working further on the making of an ideal sample.

Two main Co/Cu granular samples were studied by NMR. The first one was deposited at RT and was very promising, due to a narrow and well-defined fcc line, as well as good signal over noise ratio up to RT. We carried out a study of the temperature dependence of the lineshape, which was in very good agreement with the literature, in the temperature range investigated. The decrease of the signal with increasing temperature was interpreted as coming from the Boltzmann factor, together with the frequency factor due to the e.m.f induced in the coil by the magnetization. Unfortunately, the sample oxidized and we could not go to further studies, under current. Even though the lineshape was broader for the second sample (sample 2442), only the fcc phase was present. The temperature dependence of the lineshape was found to be due to T_2 for this sample. For the two Co/Cu granular samples, T_1 and T_2 relaxation times were measured. In both cases, T_1 was well fitted by single exponentials, so we could attribute the signal as arising from the nuclei in domains.

Additional samples were made at higher temperature (573 K), to improve the quality and were as well protected against oxidation with a Si_3N_4 layer. These samples together with the sample 2442 were studied further, under current. This will be described in section 5.3 of this thesis.

Chapter 5

Electrically excited and detected ferromagnetic nuclear resonance



5.1 Introduction

Our journey to search evidence of spin accumulation by NMR - also called ferromagnetic nuclear resonance (FNR) - lead us to a potentially powerful tool in the perspective of looking at very small samples: the electrically excited *and* electrically detected FNR (EDFNR). On one hand, the excitation was made using the spin-echo technique by sending pulsed voltages at radio frequencies, directly to the sample. In this chapter the pulse applied will be referred to as the equivalent current arising

in the sample, I_{rf} . And on the other hand, the peculiarity of EDFNR is to detect the voltage at the contacts of the magnetoresistive sample by the receiver arm of a NMR spectrometer. This detection can also be referred to as voltaic detection. As others have proposed [47], we have attempted to detect the coherent motion of the electronic magnetization as a variation in the resistance of the magnetoresistive sample because it is expected to push further the limitation of a minimum sample size. It turns out that the voltaic signal is much larger than any magnetoresistive signal one might have had in our samples. So in effect, we remained with the voltaic detection. An additional DC voltage enables us to seek for spin accumulation. In this case also, the applied voltage is expressed in term of the equivalent current. The magnetoresistive samples chosen for this study are the granular meander 2442 and his twin-brother, sample 2479 as well as samples 880 and 1880.

In this chapter, we first compare standard FNR to electrically excited and detected FNR. Next, we address the main results obtained by sending an additional DC voltage to the sample, seeking for spin accumulation evidence. Because of the effect of Joule heating encountered during the DC experiments, voltage was then applied in short pulses. A high current density (up to 5×10^5 A/cm²) was applied to the samples and we will show and discuss its effect on all the granular systems of interest.

5.2 Comparison between NMR and electrically excited and detected FNR

In our electrically excited FNR experiment, we excited directly the samples by pulsed I_{rf} . No resonant circuit was longer needed, which was very convenient. The 50 Ω matching issue of the probe was overcome by the resistance of the samples themselves, close to 50 Ω at RT for the samples 2442 and 2479. At 80 K, the resistances were: $R = 36.5 \Omega$ for sample 2442 and $R = 38.3 \Omega$ for sample 2479.

Filipkowski *et al.* predicted that it is feasible to detect electrically nuclear spin echoes in fcc Co thin films [47]. They claimed that it should be possible to detect a signal from a sample of *any* size, as long as it is above the superparamagnetic limit, below which fluctuations of the magnetization can decrease T_2 . In fact, we can show that the limit of current density implies a limit on the volume of sample that can be measured by magnetoresistive measurements. After much effort, we were unable to detect a magnetoresistive signal. It is possible that the random orientation of the magnetic grains and the fact that roughly all spins precess together throughout the sample, imply that there is no change in the resistance due to the precession of

the nuclear spin. As no signal was detectable by this method, we used the electrical detection which consists in monitoring the voltage across the sample after the rf current (and any DC voltage) has been turned off.

The circuit diagram used for the electrically excited and detected FNR experiment is illustrated in Figure 5.1.

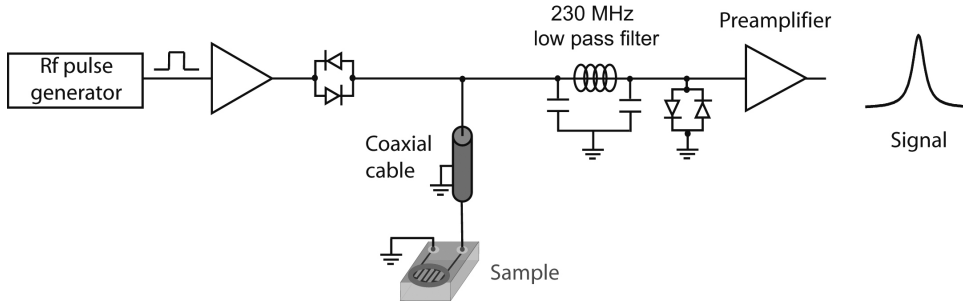


Figure 5.1: Circuit diagram for electrically excited and detected FNR. The rf power from the power amplifier (left) is driven into the sample. The voltage at the contacts of the sample is detected by the receiver arm of a NMR spectrometer.

A study of the voltaic signal amplitude as a function of the rf pulse length, for several different attenuations (pulse levels) has been carried out by electrical excitation and detection. The result, showed in Figure 5.2 is very similar to what can be observed in standard NMR: the higher the rf power level, the greater is the signal at the optimal pulse length. This is explained for the most part by the fact that the line is broad compared to the effective rf field. This dependence of signal intensity on rf level is well known in FNR. A review of FNR in zero field can be found in [44].

In Figure 5.3 we show the signal *vs.* pulse length for a granular sample where it is likely that spin accumulation is at play and for a pure Co sample, where surely no spin accumulation is expected. We get about the same response curve for both samples; The differences are consistent with the voltage driven through the samples at a set power level, because the resistance of the samples vary and because the pure Co sample has about 2 times larger susceptibility than the granular Co/Cu sample (see Figure 3.9, chapter 3).

For comparison, standard NMR has been carried out, using a resonant circuit for both excitation and detection. The sample was connected to the coaxial cable, in order to be in similar experimental conditions than for electrically excited and detected FNR. We connected a $50\ \Omega$ terminaison to the other end of the coax. However, the signal obtained when the sample was disconnected did not differ by much in signal intensity from the signal obtained when the coax was connected. When carrying out electrically excited and detected FNR, the rf coil was disconnected.

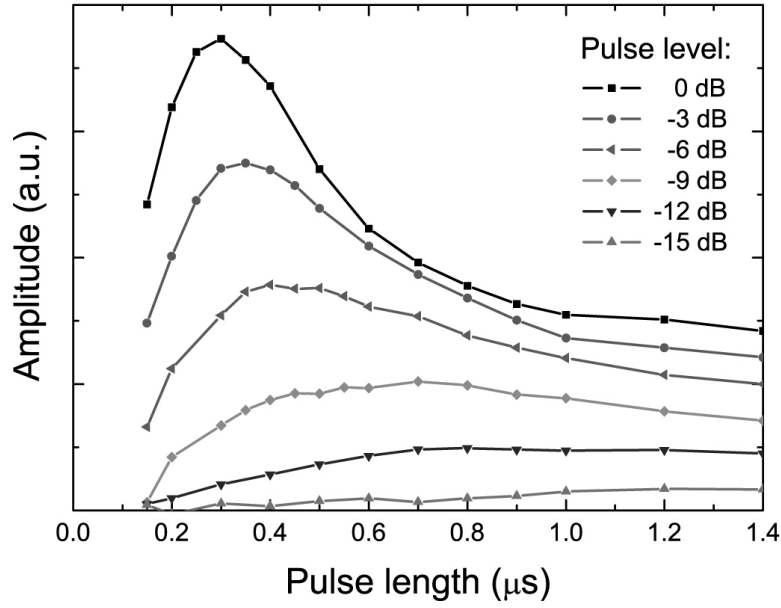


Figure 5.2: Zero-field amplitude of the voltaic signal of ^{59}Co in the Co/Cu granular sample 2442 *vs.* rf pulse length, for different pulse levels, relative to the maximum output of the rf pulse board. The rf pulses are further amplified with a set gain. At 0 dB, the rf pulse at the output of the power amplifier is of about 6 W. The spin echo sequence uses two pulses of equal lengths and equal phases. We used electrically excited and EDFNR, at $T = 80\text{ K}$ and $\tau = 10\text{ }\mu\text{s}$.

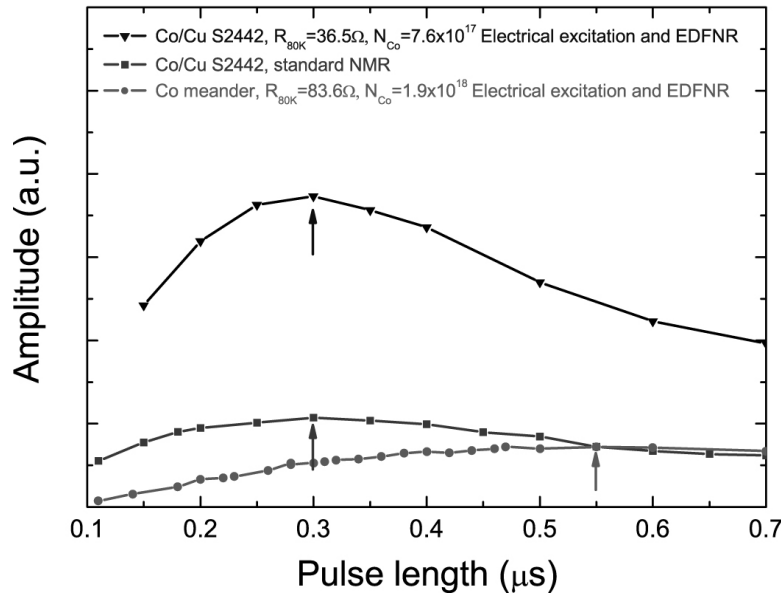


Figure 5.3: Zero-field amplitude *vs.* pulse length for 6 W rf power on Co and Co/Cu (sample 2442) meanders at $T = 80\text{ K}$ and for comparison, equivalent curve for inductive pick-up of the signal for sample 2442.

A comparison between the lineshapes recorded for standard NMR and electrically excited and EDFNR at the optimal pulse length ($0.3\text{ }\mu\text{s}$) and at 0 dB atten-

uation is presented in Figure 5.4. If normalized, the curves match. We fitted each spectrum by two Gaussians. The bulk fcc Co resonance frequency is at 216.5 MHz and the line at 208 MHz can be attributed to Co atoms with one Cu neighbor that is probably shifted due to stacking faults.

We point out here that depending on the experimental conditions, the signal intensity can be comparable for the two techniques. This depends on the coil used for NMR (due to the filling factor), and on the resistance of the sample (mismatch problem) and the available rf power for electrical excitation and detection. Nevertheless, the use of the sample itself as an “antenna” instead of the tuned circuits is very convenient, especially for broad lines because no tuning is longer needed. And electrically excited and detected FNR could be more convenient for small samples.

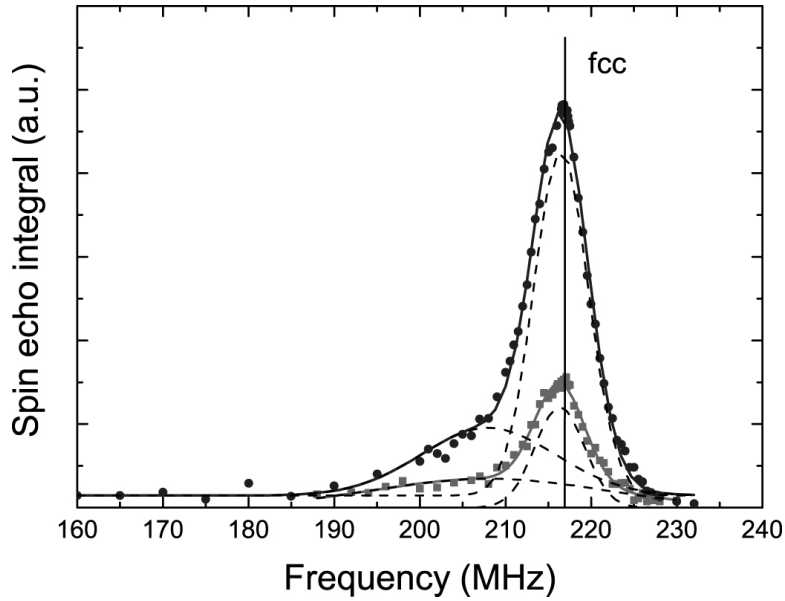


Figure 5.4: Lineshapes recorded for ^{59}Co in the Co/Cu granular sample 2442 measured at $T = 80$ K, obtained by standard NMR at zero field (squares) compared to the electrical excitation and detection directly on the sample (circles). The symbols represent the experimental points and the solid line, the fit. The vertical line represents the position of the bulk fcc Co frequency.

In order to prove that the observed signal is not due to a field created in the loop formed by the leads and the sample, we compared the amplitude of the spin echo *vs.* pulse length obtained with and without Cu shielding (see Figure 5.5). We clearly see that the shielding does not affect at all the optimal $\frac{\pi}{2}$ pulse length *i.e.* the rf field needed to flip the nuclear spin by an angle $\frac{\pi}{2}$. As the rf fields are the same with and without shielding, we can conclude that there is no effect of an external field due to the leads and sample. Therefore, the signal observed is due to the self-inductance of the sample.

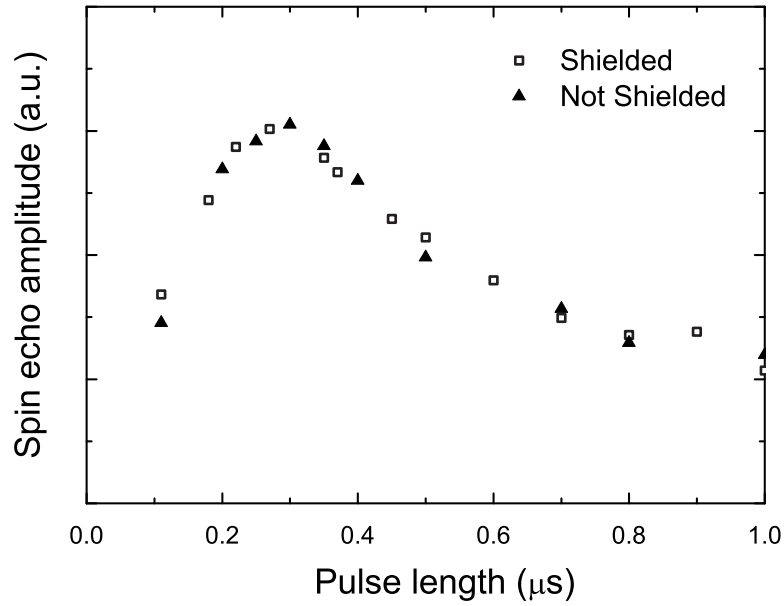


Figure 5.5: Zero-field amplitude *vs.* pulse length on the Co/Cu meander (sample 2479) at $T = 300$ K with (squares) and without (triangles) Cu shielding. The measurement was done at 0 dB.

Evidently, in the present context of the search for NMR evidence of spin accumulation, pushing the detection limits was significant in data taking time. We attribute the electrical signal to the voltage obtained by the self-inductance of the sample. As the rf field is channelled into the sample itself, the filling factor is 1. With this technique, we were able to detect 3×10^{16} Co atoms (the number of atoms being confirmed by SQUID measurements) at room temperature, on a 5 mm long piece of sample 2479. Straightforwardly, the electrical excitation and detection were efficient, despite the very small size of the sample. We recall that this sample size corresponds to 10 monolayers of Co on a 1 cm^2 . All the results presented next were obtained with this technique.

5.3 Electrically excited and EDFNR under additional bias current

We used the granular samples and the electrical excitation and detection to study the effect on the NMR of an additional voltage applied to the sample, thus imposing a steady or pulsed current through the sample in order to seek evidence of spin accumulation.

5.3.1 Continuous voltage

The circuit diagram used for the experiment is sketched in Figure 5.6. A 270 MHz low pass filter has been added at the output of the rf pulse generator in order to decrease the fluctuations of the rf pulses. The current source used was a Keithley 2400. 120pF, 1kV capacitors were added in series to the crossed-diodes in order to prevent the DC voltage from entering into the transmitter arm of the NMR spectrometer. A bias tee was also used to ensure that the DC voltage is applied to the sample only and to ensure all of the AC voltage is across the contacts of the sample in the receiver arm of the NMR spectrometer.

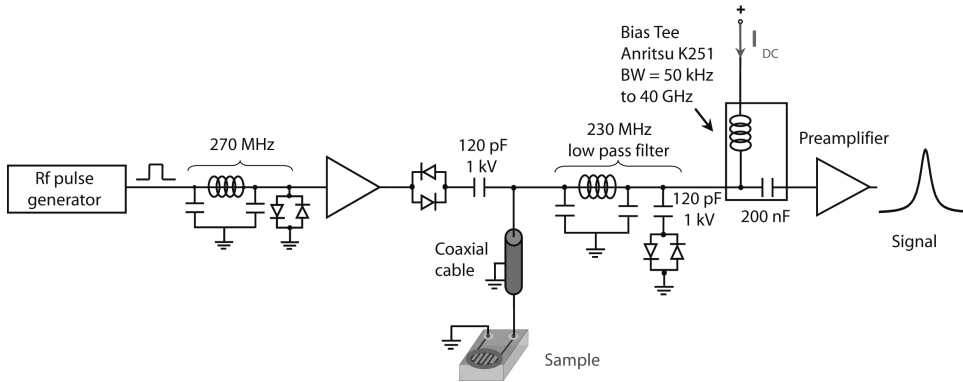


Figure 5.6: Circuit diagram for electrically excited and EDFNR under additional continuous voltage. The rf power from the power amplifier and the continuous voltage I_{DC} provided by a Keithley 2400 current source are driven into the sample. A bias tee is used in order to drive the DC voltage through the sample and the AC voltage at the contacts of the sample is detected by the receiver arm of a NMR spectrometer.

We recorded the ^{59}Co line under a continuous current of 75 mA by averaging every echo 1,000 times and we compared it to the line obtained without any additional DC voltage under the same conditions. We used the full rf power. The results are shown in Figure 5.7. A shift of ~ 0.5 MHz of the line occurred under DC voltage. This corresponds to a heating of ~ 30 K (see Figure 4.13, chapter 4). We confirmed the heating is due to the Joule effect by measuring the resistance *vs.* DC current (showed in the inset of Figure 5.7). This measurement was carried out with the Keithley current source connected directly to the sample coaxial cable.

We figured out that the bias tee was leaking, *i.e.* part of the rf signal was going into the current source and, more troubling, DC current was flowing into the preamplifier because the capacitance of the bias tee is quite large and we operate on a time scale not long enough compared to the RC time constant of this capacitor ($R = 50 \Omega$) for a complete isolation. This resulted in the saturation of the preamplifier. These issues were dealt with by replacing the bias tee with low and high

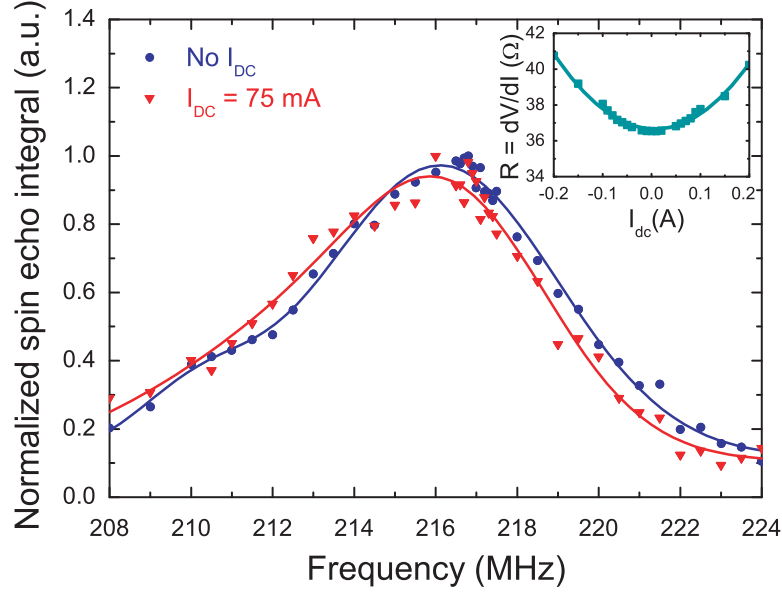


Figure 5.7: Lineshape recorded for ^{59}Co in the Co/Cu granular sample 2442, measured at $T = 80$ K, obtained by electrically excited and EDFNR with no additional voltage (circles) compared to the lineshape obtained under $I_{DC} = 75$ mA (triangles). The symbols represent the experimental points and the solid line, the fit to several gaussians. The inset shows the resistance *vs.* current measurement carried out at $T = 80$ K.

pass filters for all the following measurements. In order to avoid the effect of Joule heating encountered during the DC experiments, we then applied the voltage in short pulses.

5.3.2 Pulsed voltage

The setup used for the experiments under pulsed voltage is sketched in Figure 5.8. The additional voltage pulses expressed as I were generated by the NMR spectrometer itself, by amplifying the TTL pulses with Apex voltage amplifiers. We used two different amplifiers: PA05 supplied by an EL 302 T current source could amplify up to 11 V and PB50 supplied by an Acopian power supply Model W90NT280, up to 80 V. We also replaced the bias tee by low and high pass filters.

The same lineshape measurement as the one described above for the DC voltage has been carried out when the voltage was pulsed, as sketched in Figure 5.9 (top). Every echo was measured by averaging 1,000 times. The purpose of this measurement was to verify that the heating effect was suppressed. We were not aiming for a detection of a line shape change due to spin accumulation. Hence the choice of only 1,000 echoes for this averaging. We used the amplifier PA05, and the voltage was pulsed during the first half of the spin echo sequence. The result obtained for

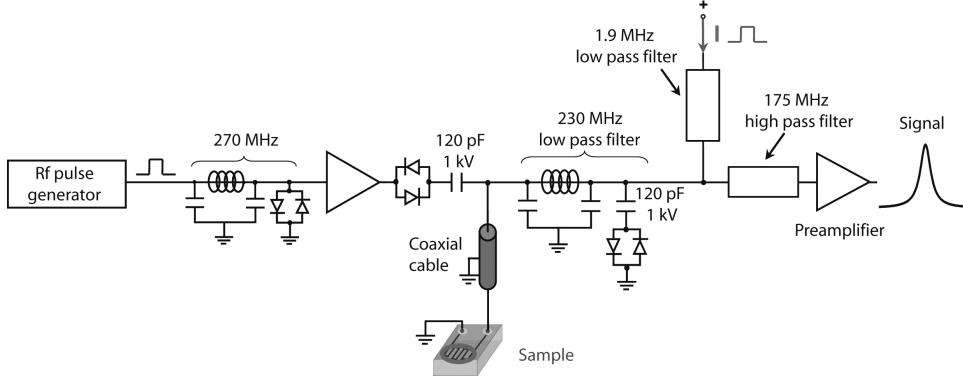


Figure 5.8: Circuit diagram for electrically excited and EDFNR under additional pulsed voltage. The rf power from the power amplifier and the pulsed voltage provided by the amplified TTL pulses coming from the spectrometer are driven into the sample. Low and high pass filters replace the bias tee. The pulsed voltage is driven through the sample and the AC voltage at the contacts of the sample is detected by the receiver arm of a NMR spectrometer.

pulsed $I = 75 \text{ mA}$ is showed in 5.9 (bottom), together with the lineshape measured without any additional voltage. No shift of the line was observed anymore and therefore, we can state that the effect of Joule heating no longer occurs.

Furthermore, a pulsed current as high as $I = 1.12 \text{ A}$ was able to be applied during the entire echo sequence, as illustrated in Figure 5.10. The sample used was the twin-brother of sample 2442, sample 2479. We recall that its resistance at 80 K was 38.3Ω . The solid line represents the fit, with two Gaussians, of the points taken without additional voltage (circles). The experimental points taken under I (triangles) are not shifted from the line which confirms that no effect of Joule heating could be detected in the sample due to the voltage, even under these conditions.

Several different experiments were carried out depending on the position of the voltage pulses I with respect to the echo sequence. The voltage pulse length was $t = 3 \mu\text{s}$ in the configurations (a), (b) and (c) as sketched in Figure 5.11 (**I**). The effect of the voltage on the spin echo integral obtained at the resonance frequency of ^{59}Co in the Co/Cu granular sample 2479 was investigated for each configuration. Similar behaviors were also found in the sample 880 and confirmed the trend. The results obtained are shown in Figure 5.11 (**II** and **III**). Applying the voltage pulse after the first rf pulse (configuration (b)) or after the second one (configuration (a)) leads to a similar behavior, that is a significant decrease of the spin echo integral as a function of the applied I . In the configuration (c), one expects a refocusing of the spins and indeed no decrease of the signal integral was detected.

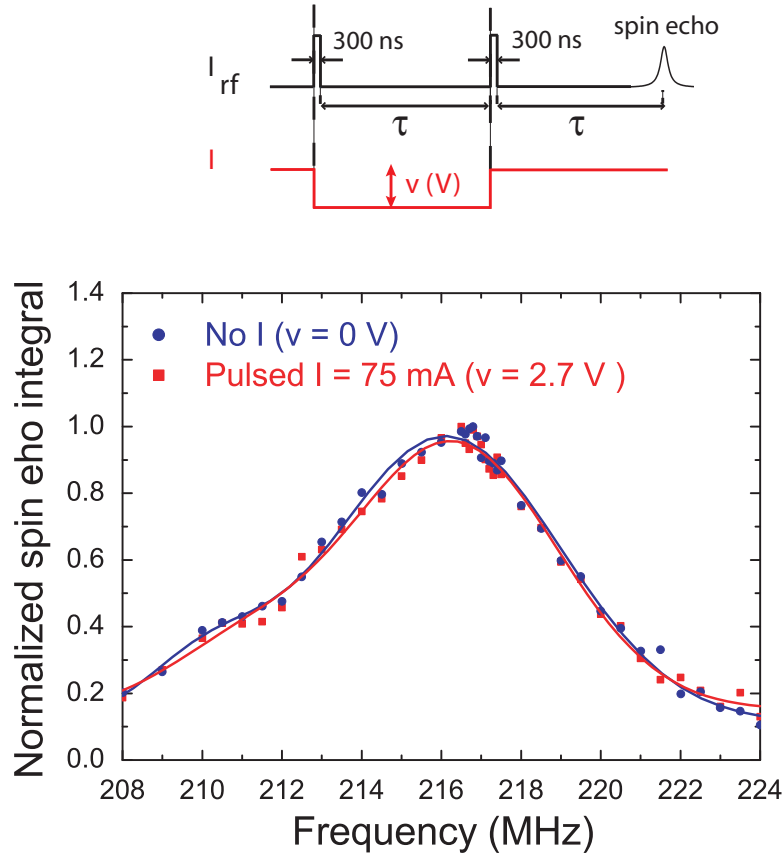


Figure 5.9: RF output and pulsed voltage sequences used for the experiment; we used $\tau = 5 \mu s$ (top). Lineshape recorded for ^{59}Co in the Co/Cu granular sample 2442, measured at $T = 80$ K, obtained by electrically excited and EDFNR with no additional voltage (circles) compared to the lineshape obtained under pulsed $I = 75$ mA (squares); the symbols represent the experimental points and the solid line, the fit to several gaussians (bottom).

In order to investigate further the decrease obtained in configuration (a) of Figure 5.11 and determine whether the effects observed are due to the field induced by the current during the voltage pulses only, or if there is a fingerprint of spin accumulation in our measurements, we repeated the measurement on the Co meander thin film made by Dr. Mohamed Abid. No spin accumulation is expected in such a sample. The resistance of the Co sample at 300 K was 179Ω and at 80 K, 83.6Ω . We present here the results obtained for $\tau = 20 \mu s$, which shows a similar behavior to $\tau = 10 \mu s$. We first carried out an experiment in order to find out which current I provided the same magnetic induction B for the two different samples (Co and CoCu). To do so, we normalized and plotted the spin echo integral obtained as a function of I for the two samples. We found an identical destruction of the signal, *i.e.* the two currents would create a similar B in the sample for $I_{Co} = 500$ mA and

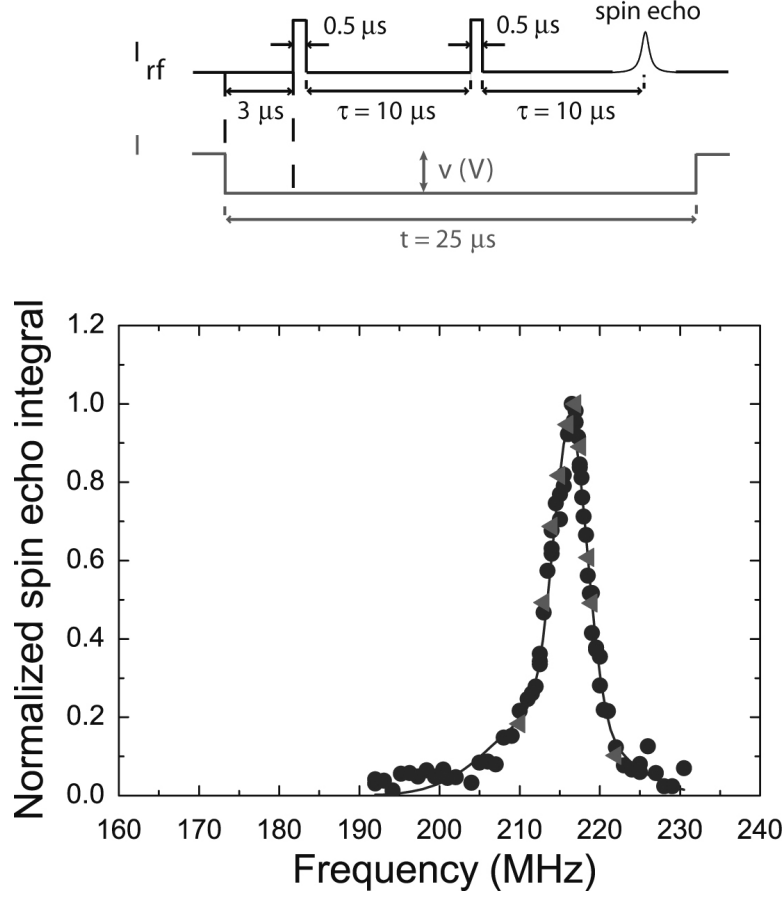


Figure 5.10: RF output and pulsed voltage sequences used for the experiment (top). Lineshape recorded for ^{59}Co in the Co/Cu granular sample 2479, measured at $T = 80$ K, obtained by electrically excited and EDFNR with no additional voltage (circles) compared to the experimental points obtained under pulsed $I = 1.12$ A (triangles); the solid line represents the fit of the points taken without I (bottom).

$$I_{CoCu} = 1 \text{ A.}$$

Several voltages I , from 130 mA to 1 A, were pulsed after the second rf pulse for a set time t (Figure 5.12 (left)). After the voltage is turned off, we inspect the nuclear signal. We show the results obtained for the Co sample, compared to the CoCu sample in Figure 5.12 (right). The data were fitted by Gaussians (see equation 5.9 below). We observe that at a given B , *i.e.* for $I_{Co} = 500$ mA and $I_{CoCu} = 1$ A, the two samples show a similar behavior. Thus, the effect observed is probably due to the field created by the current, which could hide the spin accumulation effect in such micron-sized structures.

In order to check whether the effects that we are observing are *only* due to the field induced by the current, we plotted the data observed for the Co and the different Co/Cu samples as a function of the field B that is created by the $4 \mu s$ long voltage pulses, applied after the first (similarly the second) rf pulse (Figure 5.13).

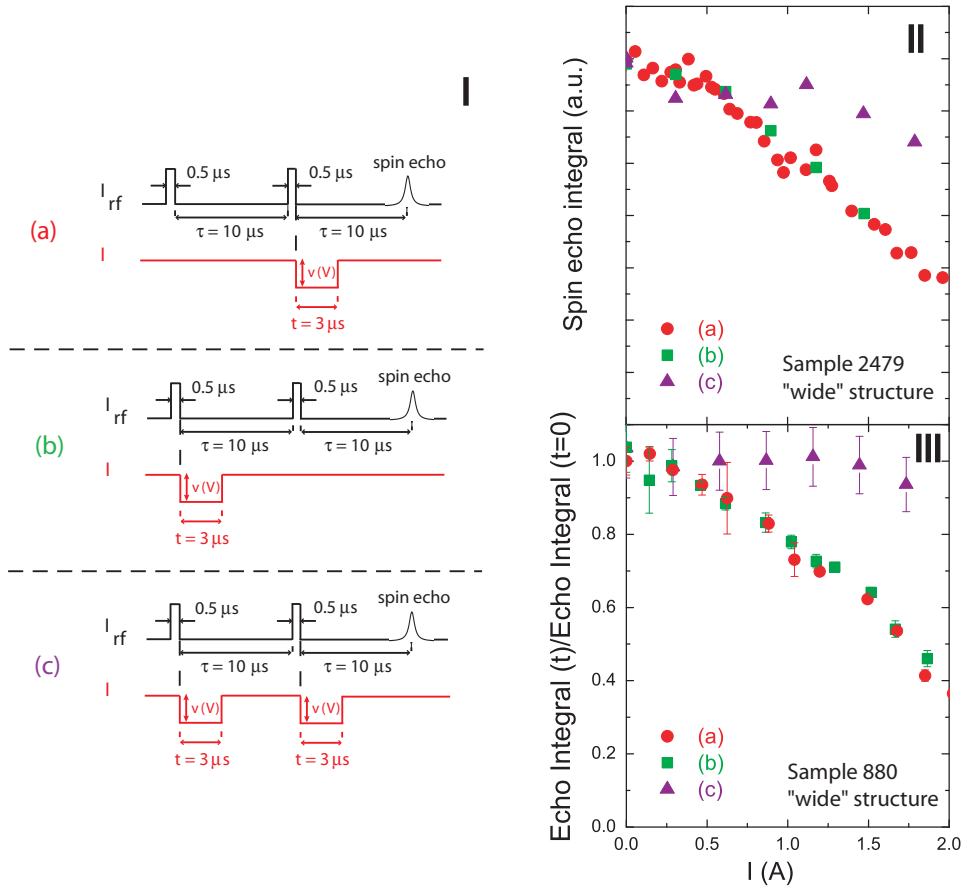


Figure 5.11: RF output and pulsed voltage sequences (a), (b) and (c) used for the different experiments (I). Spin echo integral of ^{59}Co in the Co/Cu granular sample 2479 (II) and in the sample 880 (III) for several pulsed voltages configurations (a) to (c) as a function of the current I ; The measurements were done at $T = 80$ K by electrically excited and EDFNR, at the resonance frequency.

If we consider that the magnetization \mathbf{M} is linearly related to the magnetic field \mathbf{H} , the relationship between \mathbf{B} and \mathbf{H} can be written as:

$$\Delta \mathbf{B} = \mu_0 \Delta (\mathbf{H} + \mathbf{M}) = \mu_0 (1 + \chi) \Delta \mathbf{H} \quad (5.1)$$

In our samples, the field at the surface of the wire can be approximated by: $H = \frac{I}{2w}$, where I is the current pulsed after the first rf pulse and w is the width of the meander (0.5 mm for the “wide” structure and 0.25 mm for the “narrow” structure). Thus:

$$B = \mu_0 (1 + \chi) \frac{I}{2w} \quad (5.2)$$

B is therefore proportional to $I \cdot (1 + \chi)/w$, where χ is the magnetic susceptibility determined in subsection 3.2.2 of chapter 3. Figure 5.13 shows a similar trend for all the samples, except for sample 2479. The different behavior obtained with this

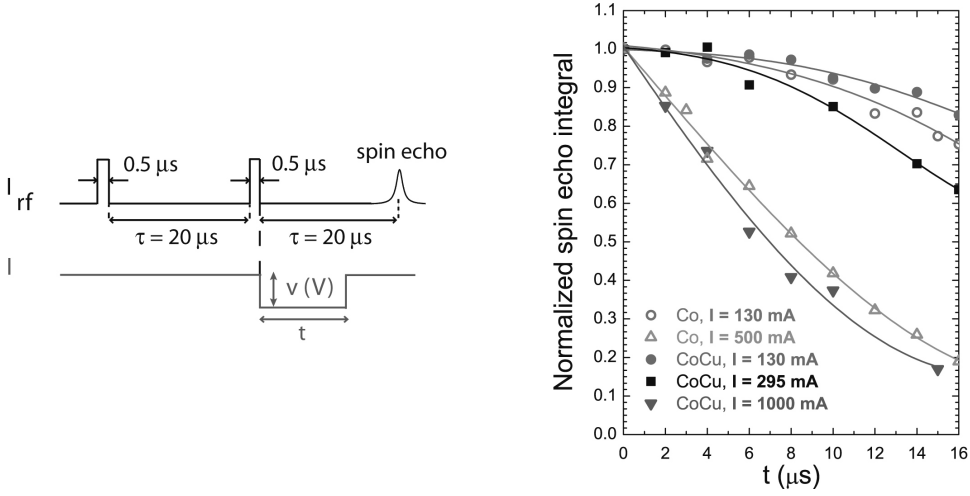


Figure 5.12: RF output and pulsed voltage sequences used for the experiment (left). Comparison of the normalized spin echo integral of ^{59}Co in the Co and Co/Cu (granular sample 2479) meander structures for several pulsed voltages I as a function of the length of the pulse t ; The measurement was done at $T = 80$ K by electrically excited and EDFNR, at the resonance frequency 217 MHz; The symbols represent the experimental points and the solid line, the fit with gaussians (right).

latter sample is not yet understood. Thus we have a successful scaling of the data for both a sample of Co where we do not expect spin accumulation and for granular samples where we hope to have it. This indicates that, for current pulses of 4 μs , most if not all of the decay observed is due to the field induced by the current. Nevertheless, we do not expect to detect any spin accumulation for the short times t , as discussed in chapter 2, so we investigated what happens at longer times. The different graphics where the normalized echo integrals are plotted *vs.* the length of the applied voltage pulses t (Figures 5.14, 5.15, 5.16) can allow us to estimate the Oersted field created, by the procedure explained below.

As we have seen above, the current flowing in the samples produces an additional source of spin echo decay. The value of the magnetic field produced by the current can be extracted from the corresponding decay curves. We use the general formalism of Recchia *et al.* [48] and consider an ensemble of nuclear spins pointing along the z axis, which corresponds to the direction of the local hyperfine field. After the first rf pulse, the nuclear spins point along the x axis and start to rotate within the xy plane under the presence of the local fluctuating field B_z accumulating at phase $\phi(t)$. The derivation is performed in the rotating frame. The second rf pulse will change the sign of the phase and the signal observed at 2τ is given by:

$$M(2\tau) = M_0 \frac{\int \cos\phi \cdot P(\phi) d\phi}{\int P(\phi) d\phi} \quad (5.3)$$

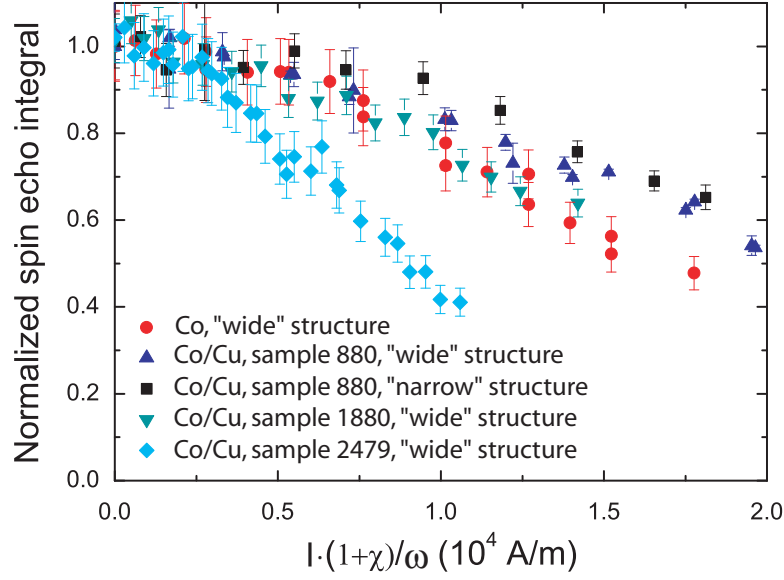


Figure 5.13: Normalized spin echo integral of ^{59}Co in the Co and in the different Co/Cu meander structures for voltages pulsed during $t = 4 \mu\text{s}$ after the first rf pulse as a function of the field. We used $\tau = 10 \mu\text{s}$. The measurements were done at $T = 80 \text{ K}$ by electrically excited and EDFNR, at the resonance frequency.

where M_0 is the signal at $\tau = 0$ and $P(\phi)$ is the probability distribution factor for the accumulated phase. We consider a Gaussian distribution of the phases:

$$P(\phi) = \frac{1}{\sqrt{2\pi\langle\phi^2\rangle}} \exp\left(-\frac{\phi^2}{2\langle\phi^2\rangle}\right) \quad (5.4)$$

and the signal at $M(2\tau)$ is given as:

$$M(2\tau) = M_0 \cdot \exp\left(-\frac{\langle\phi^2\rangle}{2}\right) \quad (5.5)$$

where $\langle\phi^2\rangle$ is the second moment of $P(\phi)$. Thus, the determination of the signal amplitude reduces to the determination of $\langle\phi^2\rangle$.

Back to our case, the application of dc voltage pulses gives rise to an additional phase $\delta\phi$:

$$\phi'(2\tau) = \phi(2\tau) + \delta\phi \quad (5.6)$$

and

$$\langle\phi'^2(2\tau)\rangle = \langle\phi^2(2\tau)\rangle + \langle\delta\phi^2\rangle + 2\langle\phi \cdot \delta\phi\rangle = \langle\phi^2(2\tau)\rangle + \langle\delta\phi^2\rangle \quad (5.7)$$

since $\langle\phi\rangle = 0$.

Finally:

$$\langle \phi'^2(2\tau) \rangle = \langle \phi^2(2\tau) \rangle + \gamma^2 B_{\perp}^2 t^2 \quad (5.8)$$

where t is the duration of the voltage pulse and B_{\perp} is the longitudinal component of the magnetic field produced by the current. As a result, the echo decay is given as:

$$\frac{M'(2\tau)}{M_0 \cdot \exp\left(-\frac{\langle \phi^2 \rangle}{2}\right)} = A \cdot \exp\left(-\frac{\gamma^2 B_{\perp}^2 t^2}{2}\right) \quad (5.9)$$

where A is a constant determined by the best fit to the experimental data and B_{\perp} can be written as:

$$B_{\perp} = CB = C \frac{\mu_0}{2} \frac{(1+\chi)I}{w} = \alpha \frac{(1+\chi)I}{w} \quad (5.10)$$

where C is a proportionality factor and $\alpha = C \frac{\mu_0}{2}$ can be extracted from the data obtained from the Co meander shown in Figure 5.14. Equation 5.9 has been applied to fit as well as to the simulations of the NMR data in the following analysis.

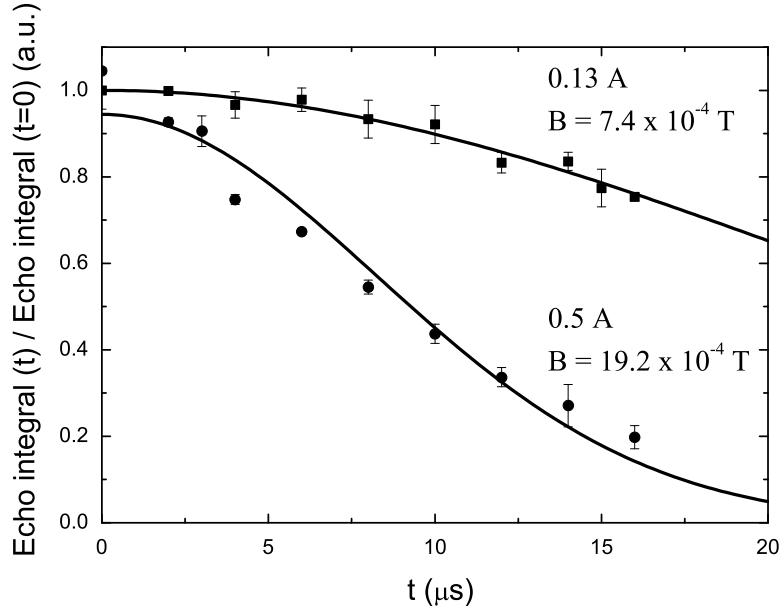


Figure 5.14: Normalized spin echo integral of ^{59}Co in the 350 nm thick Co with a “wide” meander structure for voltages pulsed during a time t after the first rf pulse as a function of t for two different currents. We used $\tau = 20 \mu\text{s}$. The measurements were done at $T = 80 \text{ K}$ by electrically excited and EDFNR, at the resonance frequency. The solid lines represent the fit to equation 5.9 and lead to the given values of B .

From the fits to the data shown in Figure 5.14 for pure Co, we can extract B at 0.13 A, where the signal drops by 35 % and B at 0.5 A where the drop becomes 95 %:

$B(0.13 \text{ A}) = 7.4 \cdot 10^{-4} \text{ T}$ and $B(0.5 \text{ A}) = 19.2 \cdot 10^{-4} \text{ T}$, leading to:

$$\alpha(0.13 \text{ A}) = \frac{B_{\perp} w}{I(1 + \chi)} = \frac{7.4 \times 10^{-4} \times 0.5 \times 10^{-3}}{0.13 \times 10.6} = 2.7 \times 10^{-7} \text{ T.m.A}^{-1}$$

and

$$\alpha(0.5 \text{ A}) = \frac{B_{\perp} w}{I(1 + \chi)} = \frac{19.2 \times 10^{-4} \times 0.5 \times 10^{-3}}{0.5 \times 10.6} = 1.8 \times 10^{-7} \text{ T.m.A}^{-1}$$

We would like to point out here that α can also be determined from a normalized spin echo curve *vs.* current, for a fixed time $t = 4 \mu\text{s}$: for this method we obtained the same value for α as the value of $\alpha(0.13 \text{ A})$ above. However, we cannot decide with certainty which value of α is the most likely. Since both values are acceptable, we will simulate the data obtained on Co/Cu with each of them.

Figure 5.15 shows the normalized spin echo integral of ^{59}Co *vs.* t in the different Co/Cu meanders for voltages pulsed during a time t after the first rf pulse, for several different currents. The symbols represent the data and the solid lines, the simulations obtained by calculating B in equation 5.9 taking the value of α found in the Co sample, at a current of 0.5 A, $\alpha(0.5 \text{ A})$. The samples 880 and 1880 differ by a factor of about 2 in thickness. Therefore, we can compare what we obtain in samples that have the same induced field, but one has twice as large a current density as the other. The general trend, for all the samples considered, is to have the experimental data *under* the simulations, *i.e.* we expect that an additional field sums up to the field created by the current. We would like to see here a signature of spin accumulation.

Nevertheless, Figure 5.16 presents the simulations obtained by calculating B in equation 5.9 taking $\alpha(0.13 \text{ A})$. Except for the sample 2479 (Figure 5.16 (d)) where the data are below the simulations for every current, it does not confirm this trend. We cannot explain why this particular sample shows a different behavior to the others, as all of them present a similar GMR ratio (see subsection 3.2.2 in chapter 3) and therefore spin accumulation is expected for all of them. The results obtained show that the simulations describe nicely the data obtained at low current (up to 0.295 A) for the samples 880 (“wide” structure) and 1880 (see Figure 5.16 (a) and (c)). The spin echo decay of these data can therefore be explained entirely by

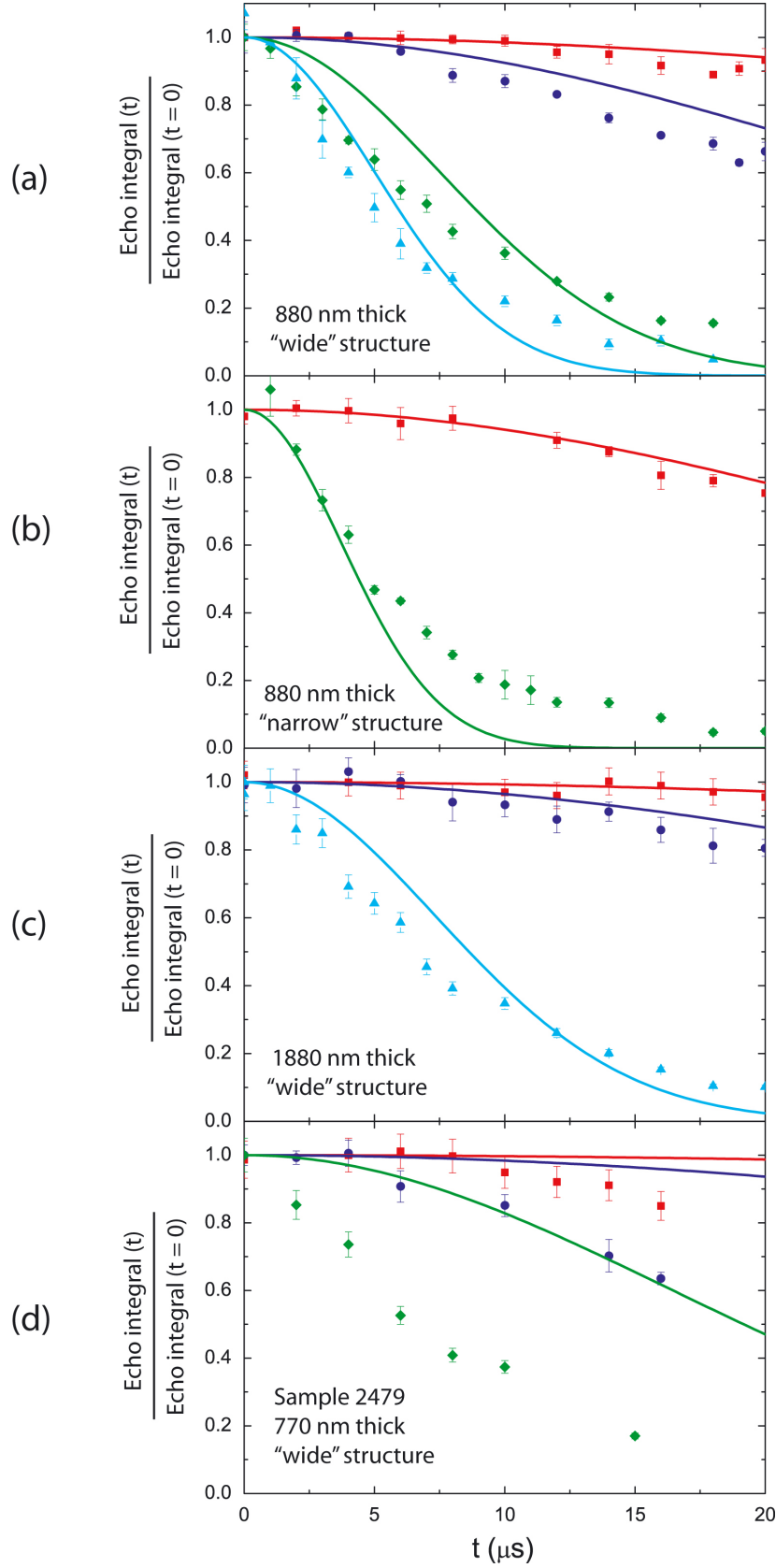


Figure 5.15: Normalized spin echo integral of ^{59}Co in the different Co/Cu meanders (a), (b), (c) and (d) for voltages pulsed during a time t after the first rf pulse as a function of t for different currents. We used $\tau = 20 \mu\text{s}$. The measurements were done at $T = 80$ K by electrically excited and EDFNR, at the resonance frequency. The solid lines represent the simulations obtained with equation 5.9 with B calculated using $\alpha = \alpha(0.5 \text{ A})$; the squares correspond to $I = 0.13$ A, the circles to 0.295 A, the diamonds to 1 A and the triangles to 1.5 A.

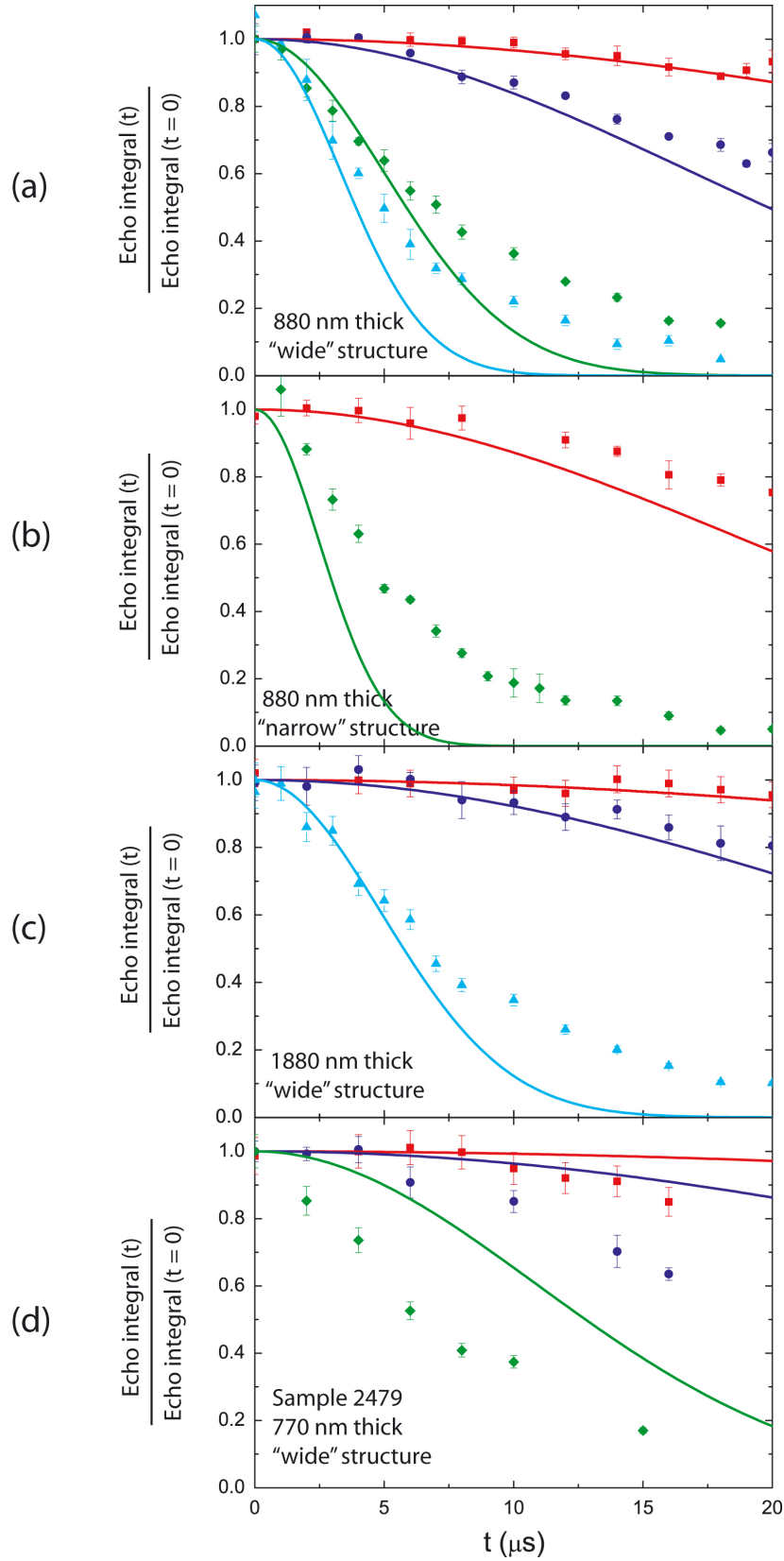


Figure 5.16: Normalized spin echo integral of ^{59}Co in the different Co/Cu meanders (a), (b), (c) and (d) for voltages pulsed during a time t after the first rf pulse as a function of t for different currents. We used $\tau = 20 \mu\text{s}$. The measurements were done at $T = 80 \text{ K}$ by electrically excited and EDFNR, at the resonance frequency. The solid lines represent the simulations obtained with equation 5.9 with B calculated using $\alpha = \alpha(0.13 \text{ A})$; the squares correspond to $I = 0.13 \text{ A}$, the circles to 0.295 A , the diamonds to 1 A and the triangles to 1.5 A .

the field created by the injected current. At higher currents and for the “narrow” structure of the sample 880, the simulations are always under the experimental data (Figure 5.16 (a), (b) and (c)), meaning that the spin echo decay created by the current is smaller than expected from the calculated field. This may be due to the fact that our calibration of α was done with a wide structure and it may not apply to the narrow structure. In other words, the approximation $H = \frac{I}{2w}$ may be too rough.

5.4 Conclusions

The search for evidence of spin accumulation lead us to the electrically excited and detected FNR, which is a very interesting technique because no coil and no resonant circuit are needed. It would also allow us to measure smaller samples.

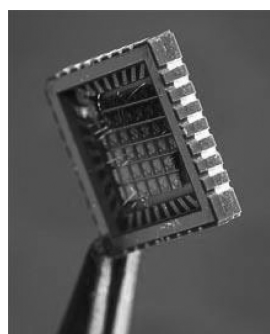
We showed in this chapter that pulsed voltages had to be applied in order to remove any Joule heating effect. Several granular samples were studied. One sample behaved as if it had a very strong effect of spin accumulation. However, we believe rather that this sample is a fluke, there is something strange about it, though none of our characterizations (SQUID measurements, NMR lineshape and GMR) show any peculiarity compared to the others. We believe that the results obtained with this sample were not relevant, as the influence of the field created by the additional voltage on all the other micron-sized samples seems pretty well under control as shown by the scaling of the spin echo decays. The other samples show evidence for a decay beyond the effect of the field induced by the current, provided one of our estimates of the calibration of this field is correct. It should be kept in mind that if we were to trace error bars about the estimated decay due to the induced field, the data points would appear inside the error bars.

We can see two ways of getting beyond the present status of the experiment:

- We make samples of the same shape, but with smaller thicknesses, differing by a factor of two. Thus, we compare what we have in samples that have the same induced field, but one has twice as large a current density as the other.
- We can improve our detection limit, thanks to EDFNR, so that we can work with much smaller samples, opening the possibility to go back to the multi-layered nanowires, *i.e.* to a CPP geometry where we know that the current has to cross the different interfaces.

Chapter 6

General conclusions and perspectives



The principal method employed in this work to search for evidence of spin accumulation was NMR. The main advantage of this technique is that it can be seen as a local probe of the nuclei.

For this study, the samples had to be large enough in order to provide enough Co atoms to be detected by NMR and at the same time small enough to get a high current density by injecting as low current as possible. Several different samples were therefore chosen and were investigated by various methods, from magnetic and mag-

Image above adopted from: http://www.technologyreview.com/files/11009/Spintronics_chip_x220.jpg

netoresistive characterizations to electron microscopy. We have shown throughout this thesis that even though some of the samples presented very interesting properties, such as a good GMR observed in the multilayered nanowires suggesting a high spin accumulation at the interfaces, they did not fulfill all the requirements needed. The granular Co/Cu systems appeared to be the best choice for our study, even though 2 to 4 A were needed in order to reach a current density of 10^6 A/cm².

A preliminary ⁵⁹Co NMR study was made on different samples, notably on the granular samples. We were interested to have a fcc phase only and a narrow and well-defined NMR line. We also investigated the temperature dependance of the lineshapes and T₁ and T₂ relaxation times. As T₁ was well fitted by single exponentials, we could attribute the signal as arising from the nuclei in domains.

We found that the electrically excited and detected FNR was opening the possibility to work with a smaller number of Co atoms than possible with standard NMR.

In the model that we used to fit the data that we obtained in the NMR experiments carried out under current, we assumed that the effect observed on the spin echo decay was due to the Oersted field created by the current. We showed that this field was large in these samples, due to their dimensionality. It could therefore possibly hide the effect of spin accumulation that we were seeking.

The data presented in this thesis may serve as an input for future experiments. The measured granular samples were too thick, *i.e.* we needed to apply too much current in order to detect the desired effect. We could therefore repeat the different measurements in thinner samples (few tens of nanometer thick), where the field created by the current injected would be less, as the current would be less to reach the same current densities. But we remind the reader here that in granular systems, the current path is complex. Therefore, if we had layers in the CPP configuration such as in Co/Cu multilayered nanowires, we would know that the current has to cross all the interfaces. Now, with the prospect of efficient detection of the NMR by means of the electrical detection described in chapter 5, there is the possibility that a much simpler structure could be sufficient to detect the NMR. This simpler structure would be much more likely to be produced in a reasonable time and effort. The possibility offered by electrically excited and detected FNR to decrease the sizes of the samples could allow us to measure samples in the CPP geometry, *i.e.* multilayered nanowires. For such samples, spin accumulation could be detected by

injecting lower currents. Another interesting experiment would be to work at lower frequencies: Figure 4.6 in chapter 4 shows that the Co/Cu multilayered nanowires present a clear shoulder in the NMR spectrum arising from Co atoms having one Cu neighbor in their nearest neighbor shell. This would be the spectral place to look for spin accumulation. The sample size has so far prevented us from going in this direction. This can be reconsidered as we manage to measure much smaller samples by EDFNR than by regular inductive FNR.

Appendix A

Samples investigated

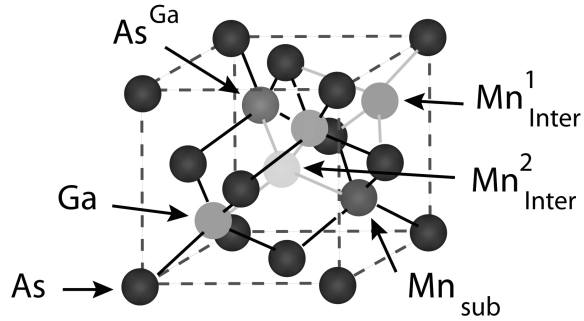
To help the reader, Table A.1 presents the main samples investigated during this work. Only some granular ones were suitable (\checkmark) for the NMR experiment under additional current.

Type of sample	Composition	Name	Characterization achieved	Comments
Nanowires	Co/Cu	ARdn4	GMR, SEM, TEM, M(H), ZFCFC, NMR	current density requirement into 10^{17} atoms not fulfilled
Long nanowires	Co/Cu	-	GMR, SEM, TEM	current density requirement not fulfilled
Long interconnected nanowires in series	Co/Cu	-	optical microscope	too low filling rate, lithographic process not ended
Interconnected pillars in series	Co/Cu	-	SEM, AFM, NMR	very high resistance
Granular meanders	Co/Ag	3	GMR, M(H), ZFCFC	no NMR signal
Granular meanders	Co/Cu	2	GMR, M(H), ZFCFC, NMR	sample oxidized
Granular meanders	Co/Cu	2442, 2479	GMR, M(H), ZFCFC, NMR	\checkmark
Granular meanders	Co/Cu	880	GMR, M(H), ZFCFC, NMR	\checkmark
Granular meanders	Co/Cu	1880	GMR, M(H), ZFCFC, NMR	\checkmark
Granular meanders	Co	Co	GMR, M(H), ZFCFC, NMR	\checkmark

Table A.1: Main samples investigated during this thesis work.

Appendix B

^{55}Mn Zero field NMR in a (Ga,Mn)As thin film



(Ga,Mn)As is a III-V based DMS that has been discovered recently [49, 50, 51]. Magnetization measurements revealed the presence of ferromagnetic order at up to 185 K in (Ga,Mn)As films [52, 53]. It is known that the impurity phase MnAs can be formed, *i.e.* Mn^{3+} ions.

^{55}Mn has a natural abundance of 100 %, a nuclear spin $I = 5/2$ for Mn and a gyromagnetic ratio of $\gamma_n = 2\pi \times 10.6 \text{ MHz/T}$.

Image above adopted from: “Determination of the local concentrations of Mn interstitials and antisite defects in GaMnAs”, F. Glas, G. Patriarche, L. Largeau, A. Lemaître, Phys. Rev. Lett. 93, 86107 (2004): GaMnAs unit cell. In addition to Mn substitutional, two kinds of defects are present: As antisites on Ga sites, and Mn interstitials. Two types of interstitials are considered, 1 and 2, with either As or Ga neighbors. The authors identified the first species as the dominant one.

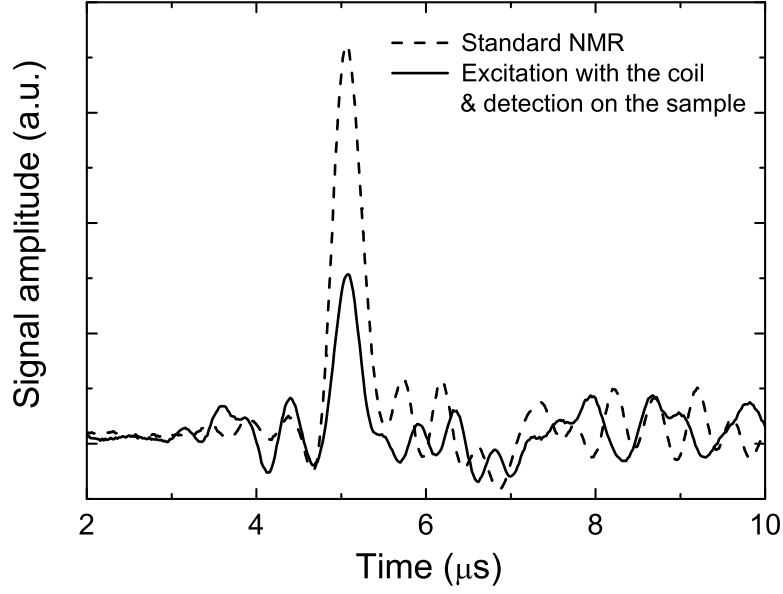


Figure B.1: Spin echoes observed in the (Ga,Mn)As thin film, at $T = 8$ K and $f = 245$ MHz. The detection method differs: standard NMR (dashed line) and electrical detection (solid line).

We performed both zero-field NMR and electrical detection (with standard excitation with the coil) on a thin film of GaAs doped with 6 % of Mn and covered with a layer of As to protect it against oxidation. The sample was provided to us by Dr. Sima Valizadeh in Uppsala, Sweden. The dimensions of the sample are: 200 nm in thickness, 12 mm in width and 13 mm in length. If we consider a density $\rho_{\text{GaAs}} = 5.32 \text{ g.cm}^{-3}$ for GaAs, the sample should contain approximately 4.16×10^{16} Mn spins.

The sample was wrapped in Teflon tape and inserted into a home-made rf coil of 5 turns and 0.8 mm inner diameter. The excitation was made with the rf coil. In order to achieve electrical detection on the sample, we made two contacts on a diagonal of the film. Due to the high resistance observed (around 800Ω), the signal that we detected was lower than the one observed by standard NMR, as illustrated in Figure B.1. We carried out zero-field NMR where the number of scans/point used was 30,000 and $\tau = 5 \mu\text{s}$. We found an optimal pulse length of $t = 1 \mu\text{s}$. The ^{55}Mn lineshape that we obtained is given in Figure B.2. The experimental points were fitted by a gaussian line centered at 231 MHz. The resonance frequencies are about 5 MHz lower than those observed for bulk ferromagnetic MnAs [15, 54], MnAs being the most probable magnetic impurity in GaMnAs phase. This difference may be attributed to an orthorhombic distortion of the unit cell [55]. The signal for Mn^{2+} is expected around 670 MHz and up to 710 MHz [56, 57]. This confirms that the signal arises from Mn^{3+} and not from Mn^{2+} , *i.e.* the majority ions in GaMnAs, as

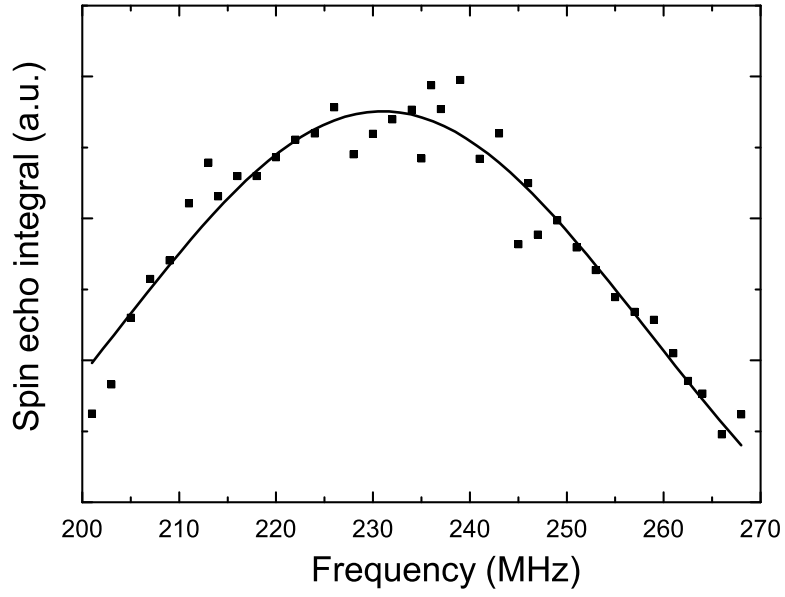


Figure B.2: Zero-field lineshape of ^{55}Mn in the (Ga,Mn)As thin film, at $T = 8$ K. The symbols represent the experimental points and the solid line, the fit.

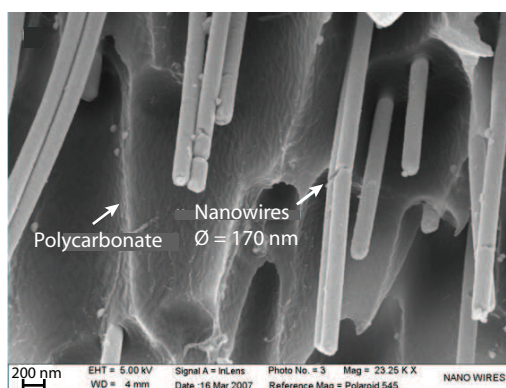
we would have expected.

After we performed this measurement, we became aware of the zero-field NMR of the Mn^{3+} in the MnAs impurity phase in a film of GaMnAs reported by Hwang *et al.* in [58]. They also detected the Mn^{3+} in MnAs in the same frequency range. We don't know of anyone having detected the Mn^{2+} signal in GaMnAs.

It is now needed to achieve NMR at higher frequency (*i.e.* 670 MHz and above) in order to detect Mn^{2+} .

Appendix C

Electrodeposition of Au nanowires



This work was done in collaboration with Dr. Mohamed Abid and Dr. Jean Gamby at the Pierre et Marie Curie University in Paris, France and led to a paper in *Lab on a Chip* (see the reference to the image above).

Random arrays of gold nanowires were made by electrodeposition into a track etched polycarbonate (PC) membrane (30 μm thick). A thin metal film of gold was

Image above adopted from: “Polycarbonate microchannel network with carpet of Gold NanoWires as SERS-active device”, J. Gamby, A. Rudolf, M. Abid, H. H. Girault, C. Deslouis, B. Tribollet, *accepted in Lab Chip*, DOI:10.1039/B820802F (2009): SEM-FEG micrograph showing the Au nanowire network inside the microchannel after selective plasma etching of the polycarbonate membrane. The size of most nanowires is estimated to be in the range 170–180 nm.

sputtered on one side of the porous membranes to serve as the cathode. The growth was performed at 55 °C in a conventional one-compartment cell with three electrode configurations: A gold foil acts as the counter electrode, a reference electrode of Ag/AgCl and the working electrode is the gold layer deposited on the polycarbonate. A solution of sodium gold (I) sulfite bath (Metakem) (gold content = 5 g/L) was used to electrodeposit gold on the polycarbonate membranes with a pore density of 10^8 pores per cm^2 (pore diameter 200 nm). The deposition potential was -0.65 V. The nanopores filling was monitored by measuring the plating current. The deposition was stopped before three-dimensional caps began to form on top of the few first emerging wires, which was revealed by a sudden increase of the plating current. After removing the conductive gold layer, one layer of polyethylene-terephthalate (PET) was laminated on each side of the membrane. The PET/PC gold nanowires/PET system was exposed to an ArF excimer laser beam in order to define a 35 μm deep cavity, which reaches the surface of the polycarbonate (see Figure C.1 (A) and (C)). We used argon plasma etching with an argon pressure of 380 mbar and a power of 100 W applied for 4 hours in order to remove 15 μm of polycarbonate (Figure C.1 (B)).

The Au nanowires in the microchannel are Surface-enhanced Raman scattering (SERS) active systems. Observation of large increases in the Raman cross section allowed us the collection of vibrational signatures which are not detectable in a straightforward manner by Raman techniques due to the high fluorescence level of bare PC. This device seems a promising tool for sensing the absorption of biomolecules.

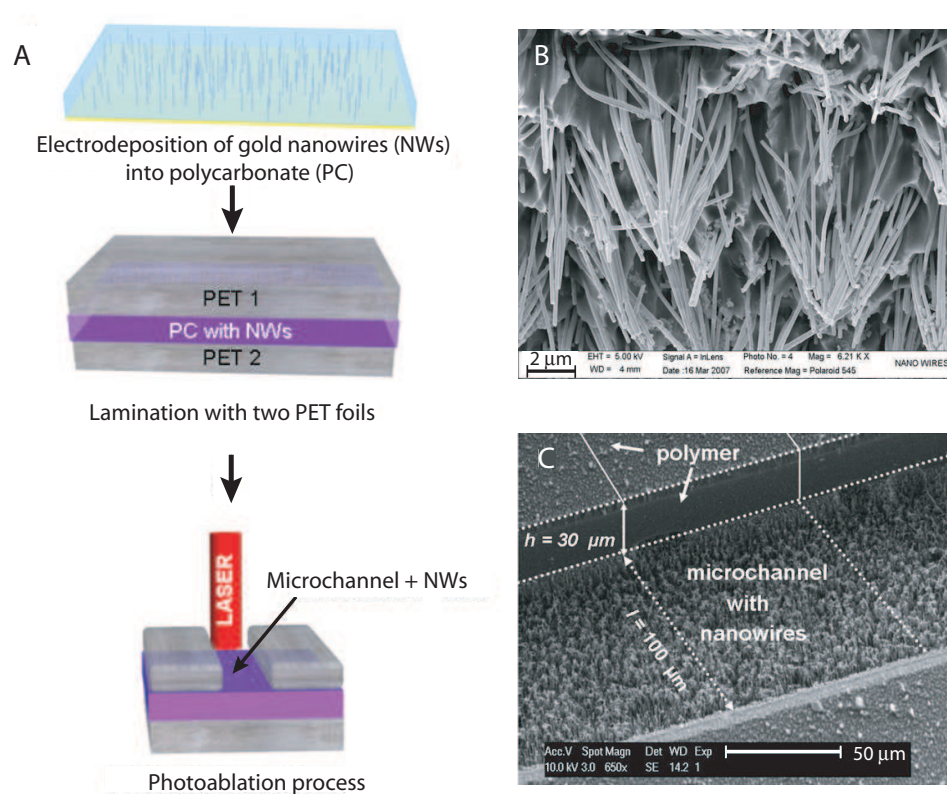
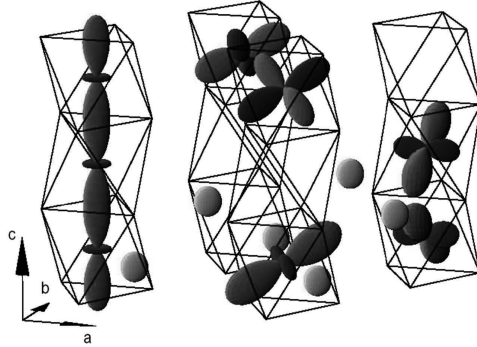


Figure C.1: (A) Schematic illustration of the microchannel network fabrication with embedded Au nanowires 3-D arrays; (B) SEM-FEG micrograph of the Au nanowires after selective plasma etching of polycarbonate; (C) SEM micrograph of the microchannel containing the metallic nanowires.

Appendix D

SQUID measurements on BaVS_3



This work was done in collaboration with Dr. Ana Akrap and Prof. László Forró, EPFL, Switzerland. We achieved susceptibility and magnetization measurements using a SQUID magnetometer on BaVS_3 samples where two types of disorder were produced: a sulfur deficiency produced by heating at elevated temperatures and point defects, produced by fast electron irradiation [59]. The latter one lead to a paper in Physical Review B [60].

Image above: BaVS_3 crystal structure.

The influence of point defects on the metal-insulator transition in BaVS₃

Ana Akrap,^{1,*} Aurore Rudolf,² Florence Rullier-Albenque,³ Helmuth Berger,¹ and László Forró¹

¹*Institut de Physique de la matière complexe, EPFL, CH-1015 Lausanne, Switzerland*

²*Institut de Physique des nanostructures, EPFL, CH-1015 Lausanne, Switzerland*

³*SPEC, Orme des Merisiers, CEA, 91191 Gif sur Yvette cedex, France*

To investigate the nature of the metal-insulator transition which takes place in BaVS₃ at $T_{\text{MIT}} = 70$ K, we study pure samples of BaVS₃ irradiated by fast electrons, which introduce point defects. Our results show that the metal-insulator transition is gradually weakened and shifted to lower temperatures by introducing the defects, in close analogy to systems where metal-insulator transition is due to a Peierls mechanism. Additionally, we study the influence of point defects on the temperature-pressure phase diagram of BaVS₃.

PACS numbers:

I. INTRODUCTION

BaVS₃ is a quasi one-dimensional itinerant spin-1/2 system, built from VS₃ chains spaced by barium atoms. The vanadium $3d^1$ electron is shared equally between two bands, a wide quasi one-dimensional d_{z^2} and a narrow isotropic e_g band.^{1,2} Despite the chainlike crystal structure and the quasi-one-dimensionality, BaVS₃ is electrically nearly isotropic.³ It is believed that this is due to the fact that electron correlations strongly reduce the on-chain conductivity. At ambient pressure, the compound undergoes three transitions: a structural transition from hexagonal to orthorhombic symmetry at $T_S \approx 240$ K, a metal-insulator transition at $T_{\text{MI}} \approx 70$ K, and a magnetic transition at $T_X = 30$ K, where an incommensurate anti-ferromagnetic order is established. By diffuse X-ray scattering it was observed that a commensurate tetramerized structure develops below T_{MI} , suggestive of a Peierls transition in the quasi one-dimensional d_{z^2} band.⁴ However, no charge disproportionation larger than $0.01 e^-$ was found below T_{MI} by anomalous scattering at vanadium K-edge.⁵ Therefore, it is still not firmly established what is the mechanism of the metal-insulator (MI) transition. In many classical charge or spin density wave systems it has been studied how the radiation damage influences the phase transition. A similar response of the metal-insulator transition in BaVS₃ to point defects may suggest that its origin is in the long-range density wave formation. Irradiation by a beam of fast electrons can be used to produce defects in a controlled way. Studies of several systems featuring a Peierls phase transition have shown that point defects locally perturb the coherency of the static charge ordering, and may ultimately prevent the system from long-range ordering.

Presence of defects is also related to an interesting issue in BaVS₃: its extreme sensitivity to disorder, seen in several of its physical properties.⁶ For example, sulphur content has a very important influence on the properties of BaVS₃. Strongly sulfur-deficient samples are known to exhibit no MI transition and to have a ferromagnetic groundstate.⁷ Moreover, the structural transition occurring at T_S can be detected in the resistivity only in the

samples with a stoichiometric sulfur content. Still, no systematic study of how the defects influence the MI transition and the phase diagram has been investigated so far.

Here we report an ambient and high-pressure transport study of BaVS₃ where point defects were induced by fast electron irradiation. We find that by introducing interstitials and vacancies by knock-on collisions, the MI transition is progressively smeared out and shifted to lower temperatures. Under high pressure, the T_{MI} line in the phase diagram is pushed towards lower pressure values.

II. METHODS

The crystals of BaVS₃ were grown in Tellurium flux, and annealed in sulfur atmosphere at high temperature.⁸ Several long needle-like crystals were cut perpendicular to the chain direction. In this study we use six samples, coming from two single crystals. The starting crystals are of high quality, which is evidenced by a sharp metal-insulator transition at ambient pressure and a high residual resistivity ratio ($\text{RRR} \sim 50$) in the metallic phase, under 2.0 GPa. The samples obtained by cutting the starting crystals across the chain direction have typical dimensions $1.25 \times 0.20 \times 0.20 \text{ mm}^3$. The irradiations are carried out with 2.5 MeV electrons in the low temperature facility of the Van de Graaff accelerator at the LSI of Ecole Polytechnique in Palaiseau. Electron fluences ranging from 0.0 up to $6.65 \cdot 10^{19} e^-/\text{cm}^2$ are applied to various pieces of the cut single crystals. The irradiation is performed with the samples immersed in liquid hydrogen, at the temperature of 20 K. The electron flux is limited to $10^{14} e^-/\text{cm}^2\text{s}$ to avoid heating of the samples during irradiation. The thickness of the samples ($\sim 200 \mu\text{m}$) is small compared to the penetration depth of the electrons, warranting homogeneous damage throughout the samples. Ambient pressure resistivity is measured *in situ*, along the VS₃ chains. The susceptibility and magnetization are measured in a Quantum Design SQUID apparatus. The high pressure resistivity measurements are performed in a clamped piston-cylinder cell, where kerosene is used as

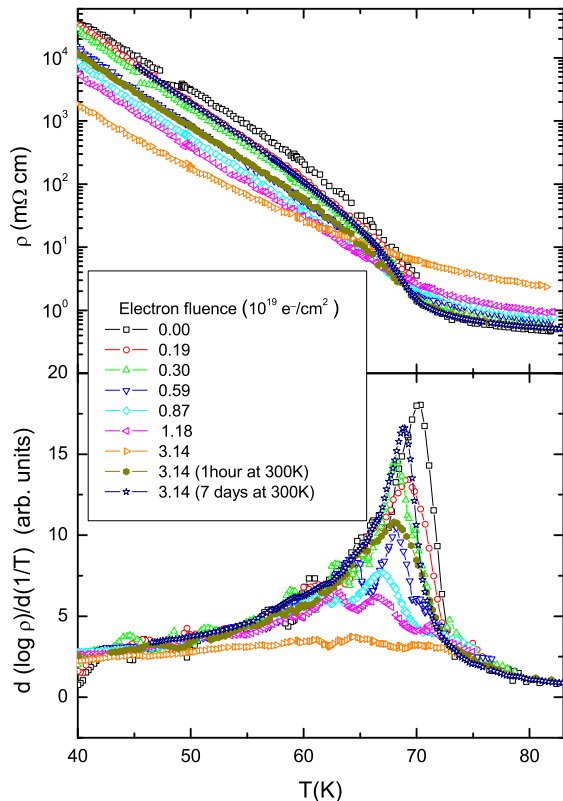


FIG. 1: (Color online) The temperature dependence of resistivity (top panel) and its logarithmic derivative for the same single crystal irradiated by different electron fluences. The sample was kept below 100 K, except in the case of the last two curves where the annealing time and temperature is indicated in the parentheses.

pressure medium.

III. RESULTS AND DISCUSSION

The top panel of Figure 1 shows the temperature dependence of the resistivity, for a single sample repetitively treated by electron radiation. The measurements of resistivity are performed *in situ*, at ambient pressure, directly after irradiating the sample and annealing it for a brief interval of several minutes at 100 K. The defects produced by irradiation are fairly sensitive to thermal migration, which is why the temperature range of the measurement is limited to 20 – 80 K. The resistivity of the sample above the MI transition increases under irradiation. The lower panel of the Figure 1 shows the logarithmic derivative $d(\log \rho)/d(1/T)$ in the same temperature range. The transition at 70 K in the pure sample shifts to lower temperatures, and is significantly widened by the presence of defects. In fact, before the T_{MI} is de-

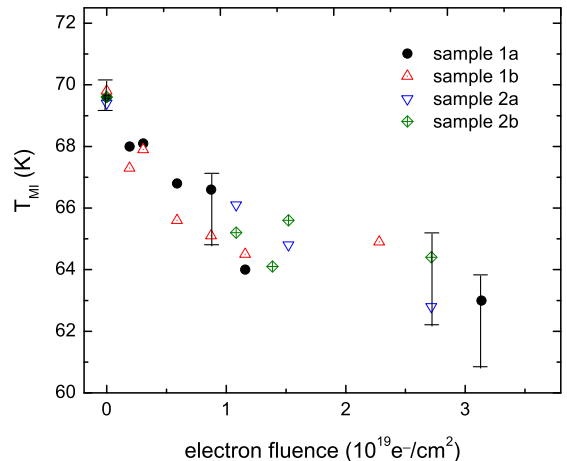


FIG. 2: (Color online) The dependence of the transition temperature on the electron fluence, during the irradiation of four different samples. The samples were maintained on temperatures below 100 K.

creased by 10 K, the metal-insulator transition is already completely smeared out. The broadening and the shift of the transition under the influence of defects has been seen in several systems that undergo a CDW transition.⁹ Such behavior is reminiscent of a Peierls mechanism driving the metal-insulator transition. Because the defects pin the phase of the density wave, coherence between the chains is weakened. The transition is thus shifted to lower temperatures and gradually suppressed. The decrease of T_{MI} is monotonous and approximately linearly dependent on electron fluence, as it can be seen in the Figure 2.

The resistivity at temperatures below the MI transition decreases as the electron dose is increased. After irradiating the sample by a fluence of $3.14 \cdot 10^{19} \text{ e}^-/\text{cm}^2$, the resistivity at 35 K decreases by more than 20 times. There are two reasons for the lowered resistivity. Firstly, the defects introduce localized states through which electrons can hop, enhancing the conductivity of the insulating phase. Secondly, the semiconducting gap is weakened because the pinning effect decreases the coherence volume of the CDWs. The value of the semiconducting gap decreases as the irradiation dose grows, from the initial value of $\sim 530 \text{ K}$ to $\sim 440 \text{ K}$ after the dose of $3.14 \cdot 10^{19} \text{ e}^-/\text{cm}^2$. Here, the values of gap are extracted from the temperatures dependence of the resistivity between 50 and 30 K, using a fit to the activated behavior:

$$\rho = \rho_0 \exp \frac{\Delta}{k_B T}. \quad (1)$$

A similar disorder-induced decrease of the gap has previously been observed in several CDW systems.⁹

When the samples of BaVS_3 are irradiated by the flux of fast electrons at the temperature of 20 K, various scat-

tering processes may take place, resulting in displacements in all the three atomic sublattices. The cross-sections for Ba, V and S atoms depend on the value of the threshold energy, E_d , which is the minimum energy necessary to eject an atom from its site. Typical values of E_d range from 10 to 30 eV depending on the structure and material. For example, E_d values for O and Cu displacements in $\text{YBa}_2\text{Cu}_3\text{O}_{7-\delta}$ are respectively 10 and 15 eV.¹⁰ As BaVS_3 is a rather open structure, we may suppose that the values of E_d are relatively low. The number of defects created per VS_3 unit is $n_d = \sigma_d^i \cdot \phi t$ where σ_d^i is the cross-section for displacing the atom i from its site and ϕt is the electron fluence. Calculations of n_d , by taking for instance $E_d = 5$ eV for S and 15 eV for V, lead to a total number of displaced V and S atoms per VS_3 plane $n_d = 2.0 \cdot 10^{-2}$ for an electron fluence of $10^{19} \text{ e}^-/\text{cm}^2$. Here we do not consider the defects in the Ba sublattice because E_d for Ba is presumably large and moreover, these defects would not be expected to have such an important influence onto the physics of BaVS_3 as S and V defects. Finally, even though this absolute value of n_d may not be very accurate, it allows a comparison between the different crystals studied.

Annealing the sample at room temperature drastically reduces the concentration of impurities. From a sample irradiated by $3.14 \cdot 10^{19} \text{ e}^-/\text{cm}^2$, shown in Figure 1, where the transition is practically wiped out, the annealing at 300 K for several days recovers the phase transition at a temperature with only a slightly less sharp peak in the logarithmic derivative, and merely ~ 1 K lower than in the pure sample. This indicates that a vast part of the defects are easily recombined through thermal diffusion. The peak in the resistivity derivative of the $3.14 \cdot 10^{19} \text{ e}^-/\text{cm}^2$ curve is positioned between the peaks of the curves measured *in situ* after irradiation fluences of 0.19 and $0.3 \cdot 10^{19} \text{ e}^-/\text{cm}^2$. Using the above estimates of displacement cross-sections, this would correspond to $n_d \sim 5 \cdot 10^{-3}$, i.e. 0.5% V and S displacements per unit formula. Since the sulfur atoms are expected to thermally migrate easier than the vanadium atoms, when the sample is annealed by warming up to room temperature, it is likely that the majority of remaining defects are in the V sublattice.

Another way of estimating the number of defects which remain after electron irradiation and a subsequent annealing at 300 K is through a measurement of magnetic susceptibility. We have investigated three pieces of the starting single crystal, irradiated respectively by the total electron fluences of $3.3 \cdot 10^{19} \text{ e}^-/\text{cm}^2$, $1.6 \cdot 10^{19} \text{ e}^-/\text{cm}^2$ and $0.0 \text{ e}^-/\text{cm}^2$. The irradiated samples showed a decrease in the T_{MI} of 1.9 K and 0.8 K, respectively. For a pure BaVS_3 sample, the temperature dependence of magnetic susceptibility shows a $1/T$ behavior down to T_{MI} , a sharp anti-ferromagnetic-like drop below the MI transition, and a negligible Curie tail below ~ 15 K.³ The presence of defects does not influence the high temperature part significantly, but it considerably increases the low-temperature Curie contribution. The magnitude of

the Curie tail due to the presence of defects can be evaluated using the following formula:

$$\chi = \frac{N_{\text{def}} \mu_{\text{eff}}^2}{T} \quad (2)$$

Here N_{def} is the density of defects, and μ_{eff} is their effective magnetic moment. If we assume that the majority of the defects in the samples are due to spin-1/2 cations V^{4+} and spin-1/2 anions S^- , we obtain that the effective spin-only moment is $\mu_{\text{eff}} \approx 1.73 \mu_B$. Using the above formula, we may estimate that the density of defects corresponding to a fluence of $10^{19} \text{ e}^-/\text{cm}^2$ and a subsequent annealing at room temperature for several days approximately equals 0.5% of defects per unit formula. The latter result is approximately a factor of 3 off the estimate we got from the above calculation using the cross-sections for V and S atom displacements, which implies that there may be other non-negligible contributions to the Curie tail.

As we have seen, the MI transition in BaVS_3 can be completely suppressed by introducing the point defects. Another way to do so is to apply hydrostatic pressure to the sample. The temperature dependence of the resistivity under various pressures, for a pristine sample and a sample with irradiation-produced point defects, is shown in upper panel of Figure 3. The external pressure gradually diminishes nesting, destroying the tetramerization along the chains, which leads to a decrease of T_{MI} and a complete suppression of the insulating phase under $p_{\text{cr}} \approx 2.0 \text{ GPa}$.¹¹

The lower panel of Figure 3 shows the phase diagram of BaVS_3 in the presence of defects, in comparison to a pure sample. We observe that the T_{MI} phase boundary is shifted to lower pressures and lower temperatures as the number of defects increases. The p_{cr} for a sample irradiated by $6.27 \cdot 10^{19} \text{ e}^-/\text{cm}^2$ is 0.3 GPa lower than for the pristine sample. We believe that the reason there is a decrease in T_{MI} is the same as for the ambient pressure: adding the defects pins the phase of the CDW in the d_{z^2} band, which weakens the coherence between the chains. The semiconducting gap is related to the transition temperature through the mean field relation $\Delta = mk_B T_{\text{MI}}$. They are both determined by the energy gain which results from lowering the electronic states energy due to the lattice deformation. If the 3D coherence volume of the CDWs is reduced by pinning effects on defects, the electronic energy gain is diminished and so is the Peierls gap. In case of BaVS_3 , $m \approx 12$ and seems to be approximately independent of pressure (up to $\sim 1.8 \text{ GPa}$)¹² and of defect concentration.

The most interesting part of the effect of point defects on the phase diagram is that close to p_{cr} . In the pristine sample the insulating phase rapidly collapses above 1.7 GPa.¹³ This collapse is attributed to the strong interaction of the d_{z^2} and e_g electrons. When pressure decreases the amplitude of the CDW, by reducing the nesting, the internal magnetic field generated by the e_g electrons further diminishes the nesting by the Zeeman

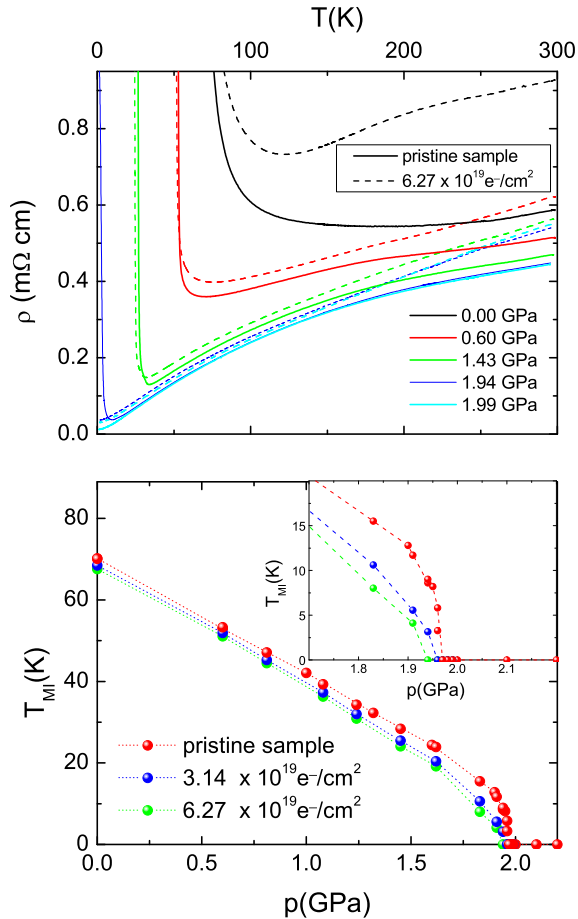


FIG. 3: (Color online) Top panel: temperature dependence of the resistivity at different pressures, shown for a pristine sample (straight line) and a sample irradiated by a fluence of $6.27 \cdot 10^{19} \text{ e}^-/\text{cm}^2$. Bottom panel: phase diagram of a pristine sample of BaVS_3 , compared to two samples where defects were introduced by electron irradiation.

splitting of $\pm k_F$. When point defects are present, they not only pin the CDW, but also introduce disorder into the ferromagnetically arranged e_g electrons. The long range magnetic order of the e_g electrons is then reduced and the collapse of the insulating phase becomes more gradual than for the pristine sample.

When $p \geq 2.0 \text{ GPa}$, in a pure BaVS_3 sample the Peierls transition is suppressed and a metallic state persists down to $T = 0 \text{ K}$. Figure 4 shows the resistivity curves for three parts of a single crystal sample, irradiated by different electron fluences, under a high pressure, $p = 2.8 \text{ GPa}$. When defects are introduced into the sample, the resistivity is enhanced in the whole thermal range. Without dwelling on the details of the low temperature dependence of resistivity, which will be discussed elsewhere,¹⁴ we focus on the high temperature range. In particular, above $\sim 150 \text{ K}$ the temperature de-

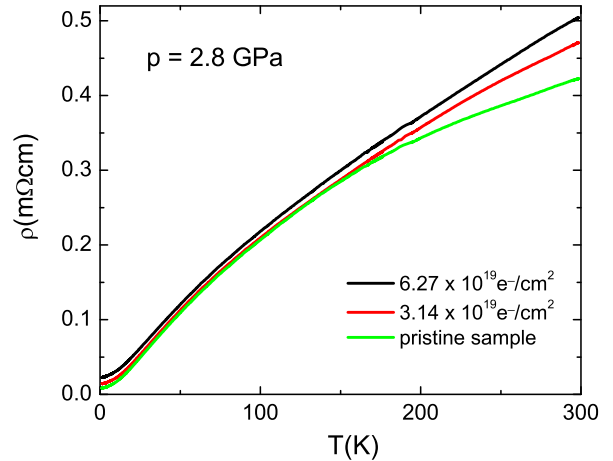


FIG. 4: (Color online) The temperature dependence of resistivity for three pieces of the same single crystal irradiated by different electron doses, under 2.8 GPa .

pendence of the resistivity becomes progressively more linear as the defect density increases. A similar progression can also be seen in the resistivity curves at lower pressures (top panel of Figure 3). Such an effect of defects on the shape of the resistivity indicates that there may be a change in the energy dispersion of a collective mode responsible for the conduction electron scattering in this temperature range. Since at such high temperatures the electronic scale is expected to give less temperature dependence, a remaining possibility is that the introduced defects alter the phononic energy spectrum. For example, if point defects broaden the phonon dispersion, by modifying the elastic constants, then there may be more phonons available for electron-phonon scattering already at lower temperatures than in the pristine sample. This in turn lowers the temperature where a term linear in temperature appears in the resistivity. By Raman spectroscopy, two possible candidates were found: $\sim 193 \text{ cm}^{-1}$ and $\sim 350 \text{ cm}^{-1}$ modes,¹⁵ which appear in the temperature range relatively close to room temperature. Finally, such a phononic interpretation of the high-temperature part of the resistivity is in accord with our rather elevated estimate of the defect density, of the order of one percent.

IV. CONCLUSION

We have shown that the pinning of the density wave to the defects gradually destroys the three-dimensional order. With $\sim 5\%$ of defects, the metal-insulator transition is suppressed entirely. Furthermore, the influence of defects on the phase diagram is such that the T_M is lowered and its sudden drop above 1.7 GPa becomes less pronounced. Finally, the strong influence of the de-

fects on the thermal dependence of the resistivity at high temperature suggests that the point defects may infer changes to the phononic spectrum.

V. ACKNOWLEDGMENTS

We gratefully acknowledge discussions with Eduard Tutiš and Gøran Nilsen. It is a pleasure to thank

Stephane Guillous from the van der Graaf accelerator of the Laboratoire des Solides Irradiés, Ecole Polytechnique in Palaiseau for the technical assistance. The work in Lausanne was supported by the Swiss National Science Foundation and its NCCR MaNEP.

* electronic address: ana.akrap@epfl.ch

- ¹ S. Mitrovic, P. Fazekas, C. Søndergaard, D. Ariosa, N. Barišić, H. Berger, D. Cloëta, L. Forró, H. Höchst, I. Kupčić, D. Pavuna, and G. Margaritondo, *Phys. Rev. B* **75**, 153103 (2007).
- ² F. Lechermann, S. Biermann, and A. Georges, *Phys. Rev. B* **76**, 085101 (2007).
- ³ G. Mihály, I. Kézsmárki, F. Zámboarszky, M. Miljak, K. Penc, P. Fazekas, H. Berger, and L. Forró, *Phys. Rev. B* **61**, R7831 (2000).
- ⁴ S. Fagot, P. Foury-Leylekian, S. Ravy, J.-P. Pouget, and H. Berger, *Phys. Rev. Lett.* **90**, 196401 (2003).
- ⁵ S. Fagot, P. Foury-Leylekian, S. Ravy, J.-P. Pouget, É. Lorenzo, Y. Joly, M. Greenblatt, M. V. Lobanov, and G. Popov, *Phys. Rev. B* **73**, 033102 (2006).
- ⁶ S. Fagot, P. Foury-Leylekian, J.-P. Pouget, G. Popov, M. Lobanov, M. Greenblatt, and P. Fertey, *Physica B* **378-380**, 1068 (2006).
- ⁷ T. Yamasaki, H. Nakamura, and M. Shiga, *J. Phys. Soc.*

Jpn **69**, 3068 (2000).

- ⁸ H. Kuriyaki, H. Berger, S. Nishioka, H. Kawakami, K. Hirakawa and F.A. Lévy, *Synthetic Metals* **71**, 2049 (1995).
- ⁹ L. Forró, A. Jánossy, L. Zuppiroli, and K. Bechgaard, *Journal de Physique* **43**, 977 (1982).
- ¹⁰ A. Legris, F. Rullier-Albenque, E. Radeva, and P. Lejay, *Journal de Physique (France)* **13**, 1605 (1993).
- ¹¹ L. Forró, R. Gaál, H. Berger, P. Fazekas, K. Penc, I. Kézsmárki, and G. Mihály, *Phys. Rev. Lett.* **85**, 1938 (2000).
- ¹² I. Kézsmárki, G. Mihály, R. Gaál, N. Barišić, H. Berger, L. Forró, C. C. Homes, and L. Mihály, *Phys. Rev. B* **71**, 193103 (2005).
- ¹³ N. Barišić et al, cond-mat/0712.3395, unpublished.
- ¹⁴ A. Akrap et al, unpublished.
- ¹⁵ Z. V. Popović, G. Mihály, I. Kézsmárki, H. Berger, L. Forró, and V. V. Moshchalkov, *Phys. Rev. B* **65**, 132301 (2002).

Bibliography

- [1] A. Fert, “Nobel Lecture: Origin, development, and future of spintronics,” *Rev. Mod. Phys.*, vol. 80, pp. 1517–1529, 2008.
- [2] P. Grünberg, “Nobel Lecture: From spin waves to giant magnetoresistance and beyond,” *Rev. Mod. Phys.*, vol. 80, pp. 1531–1540, 2008.
- [3] M. Johnson, “Analysis of anomalous multilayer magnetoresistance within the thermomagnetoelectric system,” *Phys. Rev. Lett.*, vol. 67, pp. 3594–3597, Dec. 1991.
- [4] M. N. Baibich, J. M. Broto, A. Fert, F. N. Van Dau, F. Petroff, P. Etienne, G. Creuzet, A. Friederich, and J. Chazelas, “Giant Magnetoresistance of (001)Fe/(001)Cr Magnetic Superlattices,” *Phys. Rev. Lett.*, vol. 61, pp. 2472–2475, Nov. 1988.
- [5] G. Binasch, P. Grünberg, F. Saurenbach, and W. Zinn, “Enhanced magnetoresistance in layered magnetic structures with antiferromagnetic interlayer exchange,” *Phys. Rev. B*, vol. 39, pp. 4828–4830, Mar. 1989.
- [6] W. P. Pratt, S.-F. Lee, J. M. Slaughter, R. Loloee, P. A. Schroeder, and J. Bass, “Perpendicular giant magnetoresistances of Ag/Co multilayers,” *Phys. Rev. Lett.*, vol. 66, pp. 3060–3063, June 1991.
- [7] T. Valet and A. Fert, “Theory of the perpendicular magnetoresistance in magnetic multilayers,” *Phys. Rev. B*, vol. 48, pp. 7099–7113, Sept. 1993.
- [8] L. Piraux, S. Dubois, A. Fert, and L. Belliard, “The temperature dependence of the perpendicular giant magnetoresistance in Co/Cu multilayered nanowires,” *Eur. Phys. J. B*, vol. 4, pp. 413–420, 1998.
- [9] M. Johnson and R. H. Silsbee, “Interfacial charge-spin coupling: Injection and detection of spin magnetization in metals,” *Phys. Rev. Lett.*, vol. 55, pp. 1790–1793, Oct. 1985.

- [10] Y. Ji, A. Hoffmann, J. S. Jiang, J. E. Pearson, and S. D. Bader, “Non-local spin injection in lateral spin valves,” *J. Phys. D: Appl. Phys.*, vol. 40, pp. 1280–1284, 2007.
- [11] N. Tombros, S. J. van der Molen, and B. J. van Wees, “Separating spin and charge transport in single-wall carbon nanotubes,” *Phys. Rev. B.*, vol. 73, pp. 233403–4, 2006.
- [12] F. J. Jedema, H. B. Heersche, A. T. Filip, J. J. A. Baselmans, and B. J. van Wees, “Electrical detection of spin precession in a metallic mesoscopic spin valve,” *Nature*, vol. 416, pp. 713–716, 2002.
- [13] T. Kimura, Y. Otani, and J. Hamrle, “Switching magnetization of a nanoscale ferromagnetic particle using nonlocal spin injection,” *Phys. Rev. Lett.*, vol. 96, p. 037201, 2006.
- [14] A. Abragam, *The principles of nuclear magnetism*. Oxford University Press, 1961.
- [15] E. A. Turov and M. P. Petrov, *Nuclear Magnetic Resonance in Ferro- and Antiferromagnets*. Halsted Press, a division of John Wiley & Sons, Inc., New York, 1972.
- [16] H. A. M. de Gronckel, “The nanostructure of Multilayered Films, A NMR study,” *Ph. D. Thesis, Jülich*, pp. 3–20, 1993.
- [17] E. Fermi, “Über die magnetischen Momente der Atomkerne,” *Z. Phys.*, vol. 60, pp. 320–333, 1930.
- [18] A. C. Gossard and A. M. Portis, “Observation of Nuclear Resonance in a Ferromagnet,” *Phys. Rev. Lett.*, vol. 3, pp. 164–166, Aug. 1959.
- [19] A. C. Gossard and A. M. Portis, “Nuclear Resonance in Ferromagnetic Cobalt,” *J. Appl. Phys.*, vol. 31, pp. 205S–213S, 1960.
- [20] N. W. Ashcroft and N. D. Mermin, *Solid State Physics*. Saunders College Publishing, 1976.
- [21] C. P. Slichter, *Principles of Magnetic Resonance*. 3rd edition, Springer-Verlag, 1990.
- [22] D. Fekete, A. Grayevsky, D. Shaltiel, U. Goebel, E. Dormann, and N. Kaplan, “Test for Band Ferromagnetism in hcp Cobalt: Knight Shift in the Ferromagnetic Phase of Cobalt,” *Phys. Rev. Lett.*, vol. 36, pp. 1566–1569, June 1976.

- [23] S. Valizadeh, J. M. George, P. Leisner, and L. Hultman, "Electrochemical synthesis of Ag/Co multilayered nanowires in porous polycarbonate membranes," *Thin Solid Films*, vol. 402, pp. 262–271, Jan. 2002.
- [24] A. E. Berkowitz, J. R. Mitchell, M. J. Carey, A. P. Young, S. Zhang, F. E. Spada, F. T. Parker, A. Hutten, and G. Thomas, "Giant magnetoresistance in heterogeneous Cu-Co alloys," *Phys. Rev. Lett.*, vol. 68, pp. 3745–3748, June 1992.
- [25] J. Q. Xiao, J. S. Jiang, and C. L. Chien, "Giant magnetoresistance in non-multilayer magnetic systems," *Phys. Rev. Lett.*, vol. 68, pp. 3749–3752, June 1992.
- [26] V. Scarani, B. Doudin, and J.-P. Ansermet, "The microstructure of electrodeposited cobalt-based nanowires and its effect on their magnetic and transport properties," *Journal of Magnetism and Magnetic Materials*, vol. 205, pp. 241–248, Nov. 1999.
- [27] H. Yousef, K. Hjort, and M. Lindeberg, "Reliable small via interconnects made of multiple sub-micron wires in flexible PCB," *J. Micromech. Microeng.*, vol. 17, pp. 700–708, 2007.
- [28] L. Piraux, J. M. George, J. F. Despres, C. Leroy, E. Ferain, R. Legras, K. Ounadjela, and A. Fert, "Giant magnetoresistance in magnetic multilayered nanowires," *Applied Physics Letters*, vol. 65, no. 19, pp. 2484–2486, 1994.
- [29] A. Blondel, J. P. Meier, B. Doudin, and J.-P. Ansermet, "Giant magnetoresistance of nanowires of multilayers," *Applied Physics Letters*, vol. 65, no. 23, pp. 3019–3021, 1994.
- [30] S. Valizadeh, L. Hultman, J. George, and P. Leisner, "Template Synthesis of Au/Co Multilayered Nanowires by Electrochemical Deposition," *Advanced Functional Materials*, vol. 12, no. 11-12, pp. 766–772, 2002.
- [31] L. J. Swartzendruber, "Properties, units and constants in magnetism," *Journal of Magnetism and Magnetic Materials*, vol. 100, pp. 573–575, Nov. 1991.
- [32] L. E. Toth and S. F. Ravitz, "Ferromagnetic nuclear resonance in cobalt nuclei in stacking faults and twins," *J. Phys. Chem. Solids*, vol. 24, pp. 1203–1206, 1963.
- [33] E. A. M. van Alphen, S. G. E. te Velthuis, H. A. M. de Gronckel, K. Kopinga, and W. J. M. de Jonge, "NMR study of the strain in Co-based multilayers," *Phys. Rev. B*, vol. 49, pp. 17336–17341, June 1994.

- [34] Y. G. Pogorelov, G. N. Kakazei, J. B. Sousa, A. F. Kravets, N. A. Lesnik, M. M. Pereira de Azevedo, M. Malinowska, and P. Panissod, “Structural and magnetic study of heterogeneous $\text{Co}_x\text{Ag}_{1-x}$ films by resonance and magnetometric techniques,” *Phys. Rev. B*, vol. 60, pp. 12200–12206, Nov. 1999.
- [35] E. A. M. van Alphen and W. J. M. de Jonge, “Granular Co/Ag multilayers: Relation between nanostructure, and magnetic and transport properties,” *Phys. Rev. B*, vol. 51, pp. 8182–8192, Apr. 1995.
- [36] Y. Ji, A. Hoffmann, J. S. Jiang, and S. D. Bader, “Spin injection, diffusion, and detection in lateral spin-valves,” *Appl. Phys. Lett.*, vol. 85, pp. 6218–6220, Dec. 2004.
- [37] J.-H. Ku, J. Chang, H. Kim, and J. Eom, “Effective spin injection in Au film from Permalloy,” *Appl. Phys. Lett.*, vol. 88, pp. 172510–3, Apr. 2006.
- [38] J. L. Bubendorff, C. Mény, E. Beaurepaire, P. Panissod, and J. P. Bucher, “Electrodeposited cobalt films: hcp versus fcc nanostructuring and magnetic properties,” *Eur. Phys. J. B*, vol. 17, pp. 635–643, 2000.
- [39] H. A. M. de Gronckel, K. Kopinga, W. J. M. de Jonge, P. Panissod, J. P. Schillé, and F. J. A. den Broeder, “Nanostructure of Co/Cu multilayers,” *Phys. Rev. B*, vol. 44, pp. 9100–9103, Oct. 1991.
- [40] P. Panissod, *Frontiers in Magnetism of Reduced Dimension Systems*. “Structural and magnetic investigations of ferromagnets by NMR. Application to magnetic metallic multilayers,” NATO ASI Series, eds. Wigen, Lesnik & Baryakhtar, Kluwer Academic, pp. 15-17, 1998.
- [41] P. C. Riedi, “Temperature Dependence of the Hyperfine Field and Hyperfine Coupling Constant of Iron,” *Phys. Rev. B*, vol. 8, pp. 5243–5246, Dec. 1973.
- [42] H. Yasuoka and R. T. Lewis, “Temperature Dependence of Co^{59} Nuclear Magnetic Resonance in Single-Domain Cobalt Particles,” *Phys. Rev.*, vol. 183, pp. 559–562, July 1969.
- [43] M. Kawakami, T. Hihara, Y. Kōi, and T. Wakiyama, “The Co^{59} Nuclear Magnetic Resonance in Hexagonal Cobalt,” *Journal of the Physical Society of Japan*, vol. 33, pp. 1591–1598, 1972.
- [44] V. Scarani, “NMR studies on magnetic nanostructures,” *Ph. D. Thesis 2146*, Ecole Polytechnique Fédérale de Lausanne, pp. 39–42, 2000.

- [45] M. Weger, “Longitudinal Nuclear Magnetic Relaxation in Ferromagnetic Iron, Cobalt, and Nickel,” *Phys. Rev.*, vol. 128, pp. 1505–1511, Nov. 1962.
- [46] V. Jaccarino, N. Kaplan, R. Walstedt, and J. Wernick, “Field dependence of nuclear relaxation in ferromagnetic metals,” *Physics Letters*, vol. 23, pp. 514–515, Nov. 1966.
- [47] M. E. Filipkowski, E. E. Hach III, and M. Offenbacher, “Electrical detection of nuclear spin echoes,” *Journal of Magnetism and Magnetic Materials*, vol. 306, pp. 321–323, Nov. 2006.
- [48] C. H. Recchia, K. Gorny, and C. H. Pennington, “Gaussian-approximation formalism for evaluating decay of NMR spin echoes,” *Phys. Rev. B*, vol. 54, pp. 4207–4217, Aug. 1996.
- [49] H. Ohno, A. Shen, F. Matsukura, A. Oiwa, A. Endo, S. Katsumoto, and Y. Iye, “(Ga,Mn)As: A new diluted magnetic semiconductor based on GaAs,” *Appl. Phys. Lett.*, vol. 69, pp. 363–365, 1996.
- [50] H. Ohno, “Making nonmagnetic semiconductors ferromagnetic,” *Science*, vol. 281, pp. 951–956, 1998.
- [51] H. Ohno, “Properties of ferromagnetic III-V semiconductors,” *J. Magn. Magn. Mater.*, vol. 200, pp. 110–129, 1999.
- [52] V. Novák, K. Olejník, J. Wunderlich, M. Cukr, K. Výborný, A. W. Rushforth, K. W. Edmonds, R. P. Campion, B. L. Gallagher, J. Sinova, and T. Jungwirth, “Curie point singularity in the temperature derivative of resistivity in (Ga,Mn)As,” *Physical Review Letters*, vol. 101, pp. 077201–4, Aug. 2008.
- [53] M. Wang, R. P. Campion, A. W. Rushforth, K. W. Edmonds, C. T. Foxon, and B. L. Gallagher, “Achieving high Curie temperature in (Ga,Mn)As,” *Appl. Phys. Lett.*, vol. 93, pp. 132103–3, 2008.
- [54] H. Jinushi, Y. Kasamatsu, K. Hiraoka, and T. Hihara, “NMR study of MnAs at atmospheric and high pressures,” *Journal of Magnetism and Magnetic Materials*, vol. 272–276, pp. E587–E588, May 2004.
- [55] A. K. Das, C. Pampuch, A. Ney, T. Hesjedal, L. Däweritz, R. Koch, and K. H. Ploog, “Ferromagnetism of MnAs Studied by Heteroepitaxial Films on GaAs(001),” *Phys. Rev. Lett.*, vol. 91, pp. 087203–4, Aug. 2003.

- [56] H. Yasuoka, T. Ngwe, V. Jaccarino, and H. J. Guggenheim, “ Mn^{55} Nuclear Magnetic Resonance in MnF_2 ; The Suhl-Nakamura Interaction,” *Phys. Rev.*, vol. 177, pp. 667–672, Jan. 1969.
- [57] I. O. Troyanchuk, L. A. Bashkirov, A. A. Shemyakov, and V. K. Prokopenko, “NMR-spectroscopy study of $\text{Ca}(\text{Cu}_{3-x}\text{Mn}_x)\text{Mn}_4\text{O}_{12}$ perovskites,” *Phys. Stat. Sol. (a)*, vol. 109, pp. K59–K61, 1988.
- [58] T. Hwang, S. Lee, H. K. Choi, H. S. Kim, Y. D. Park, and S. H. Chun, “Evidence for secondary ferromagnetic phases in the nuclear magnetic resonance spectra of GaMnAs epitaxial films and their nominal effect,” *J. Korean Phys. Soc.*, vol. 52, pp. 396–401, 2008.
- [59] A. Akrap, “Competing orders in strongly correlated systems studied by transport measurements,” *Ph. D. Thesis 4124, Ecole Polytechnique Fédérale de Lausanne*, pp. 53–65, 2008.
- [60] A. Akrap, A. Rudolf, F. Rullier-Albenque, H. Berger, and L. Forró, “Influence of point defects on the metal-insulator transition in BaVS_3 ,” *Phys. Rev. B*, vol. 77, pp. 115142–4, Mar. 2008.

Curriculum Vitae

Aurore Rudolf

Laboratoire de Physique des Matériaux Nanostructurés

École Polytechnique Fédérale de Lausanne

CH-1015 Lausanne, Switzerland

aurore.rudolf@gmail.com

Personal information

Date of birth	September 12, 1979
Nationality	French
Marital Status	single

Education

2005–2009	PhD student at EPFL, Faculty of basic sciences, Institute of physics of nanostructures under the supervision of and in the group of Prof. Jean-Philippe Ansermet.
2003–2005	Master 2 Research in Material Sciences, Joseph Fourier University, France. Diploma project: “Magnetic thin films studied by Transmission Electron Microscopy” (Advisor: Dr. Pascale Bayle Guillemaud).
1999–2003	B. Sc. in Physics, Haute-Alsace University, France.
1997–1999	First year of studies in Pharmaceutics, Louis Pasteur University, France.
1997	Scientific A-level (“Baccalauréat”), Théodore Deck Secondary School, France.

Skills

Languages	French (native language); English (fluent); German (good level).
Software	Origin, Mathematica, LaTeX, Microsoft Office.

Experimental methods

Nuclear magnetic resonance;
Magnetic and Magneto-transport measurements;
Electrodeposition and other chemistry techniques;
Transmission and scanning electron microscopies;
UV lithography;
Cryogenic and vacuum techniques;
Electronics.

Teaching experience

2005-2008 Teaching assistant in advanced laboratory work for 3rd year students in Physics (Travaux pratiques de physique III) in nuclear magnetic resonance, EPFL (R. Sanjines). Awarded for teaching performance in winter semester 2007, Faculty of Basic Science, EPFL.

Conference presentations

- A. Rudolf, M. Abid, A. D. Santos, A. Comment and J.-Ph. Ansermet, “Electrically excited and detected nuclear magnetic resonance in ferromagnetic thin films”, *Gordon Research Conference on Magnetic Nanostructures*, Aussois, France, August 31-September 5, 2008: **poster presentation**.
- A. Rudolf, M. Abid, S. Valizadeh, A. D. Santos, J. van der Klink and J.-Ph. Ansermet, “ ^{59}Co nuclear magnetic resonance of nanostructures”, *Swiss Physical Society*, Geneva, Switzerland, March 27, 2008: **oral presentation**.
- A. Rudolf, M. Abid, S. Valizadeh, A. D. Santos, J. van der Klink and J.-Ph. Ansermet, “ ^{59}Co nuclear magnetic resonance of nanostructures”, *Euro-mar*, Tarragona, Spain, July 2-5, 2007: **poster presentation**.

Publications

- J. Gamby, A. Rudolf, M. Abid, H. H. Girault, C. Deslouis, B. Tribollet, “Polycarbonate microchannel network with carpet of Gold NanoWires as SERS-active device”, *accepted in Lab Chip*, DOI:10.1039/B820802F (2009).
- A. Akrap, A. Rudolf, F. Rullier-Albenque, H. Berger and L. Forró, “Influence of point defects on the metal-insulator transition in BaVS_3 ”, *Phys. Rev. B.* **77**, 115142 (2008).

- L. Gravier, A. Fábíán, A. Rudolf, A. Cachin, K. Hjort and J.-Ph. Ansermet, “Thermopower measurement of single isolated metallic nanostructures”, *Meas. Sci. Technol.* **15**, 420 (2004).
- L. Gravier, A. Fábíán, A. Rudolf, A. Cachin, J.-E. Wegrowe, and J.-Ph. Ansermet, “Spin-dependent thermopower in Co/Cu multilayer nanowires”, *J. Magn. Magn. Mater.* **271**, 153 (2004).